Spin drag below the condensation temperature of an ultra-cold Bose gas

Martijn van 't Woud BSc

Supervision: Pieter C. Bons MSc and prof. dr. Peter van der Straten

October 28, 2013

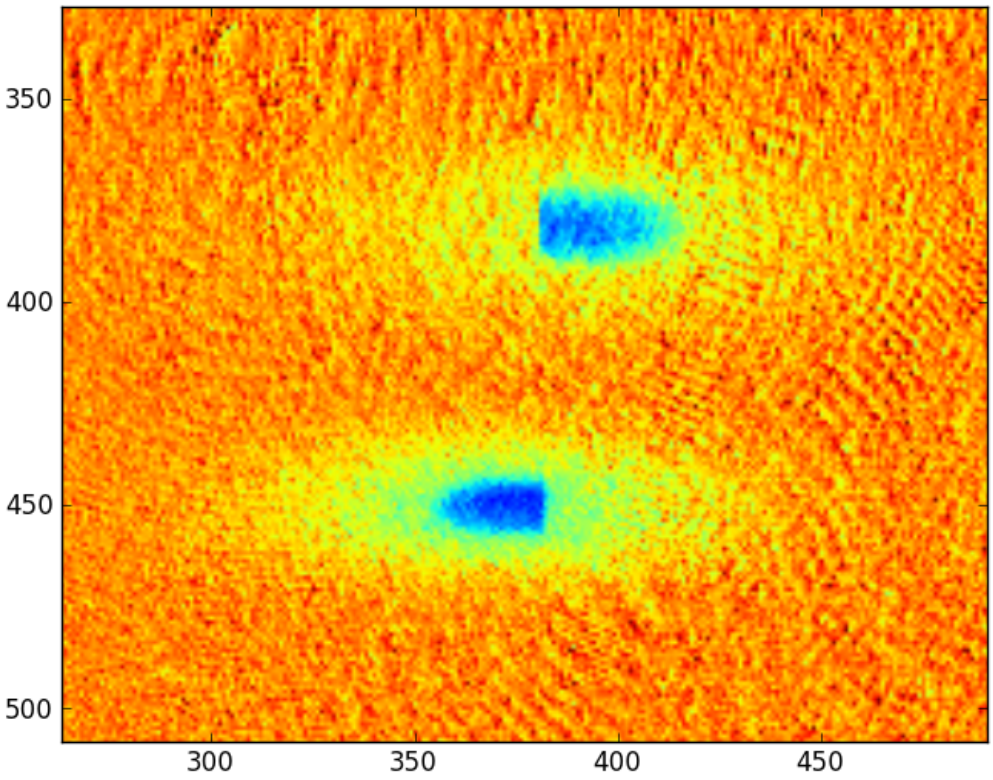

Universiteit Utrecht

Abstract

In this thesis, an experiment involving spin drag between two clouds of sodium atoms (one with spin -1, one with spin 0) in a Bose-Einstein condensate is described and analyzed in two different ways. These analysis methods involve both the movement of domain walls of the two clouds, and the movement of the centers of mass of the two clouds. It turns out that the movement of the domain walls is significantly different than that of the centers of mass of the clouds. Also, a couple of possible parameterizations are given to analyze the center of mass method properly. Furthermore, analytical formulas for the calculation of a magnetic cloverleaf trap, as used in the setup for Bose-Einstein condensation, are derived and the characteristics of this trap are discussed. The parameters describing the shape of the trap, which are the radial and axial trap frequencies, are calculated as a function of the current through the coils, and the change in magnetic field of the trap after applying several gradients is investigated. Finally, a series of experiments involving both the fast and slow flux of particles, used for loading the trap, from the oven to the vacuum chamber are described and analyzed. The results of the fast flux are compared with calculations involving the vapor pressure. The behavior of the magnetic field of the Zeeman coils is also discussed.

Contents

Chapter 1

General Introduction

In this thesis, three different subjects, of which two are related to Bose-Einstein condensation, are discussed. For the reader who is already familiar with this field of research, this general introduction can be skipped. For the reader who is not familiar, first the concept of Bose-Einstein condensation is discussed. When describing a gas, two parameters are important: the inter-particle distance and the size of the particle. Depending on the way of describing this 'particle', the 'size' can either be the radius (or diameter) if the particle is described classically, or the so-called thermal wavelength when the particle is described as a quantum mechanical wave. The thermal wavelength (or De Broglie wavelength) is given by:

$$\Lambda_{\mathrm{dB}} = \frac{h}{\sqrt{2\pi m k_{\mathrm{B}} T}}. \tag{1.1}$$

Here, h is Planck's constant, k_{B} is Boltzmann's constant, m is the mass of the particle and T is the temperature of the gas. It can be seen from Eq. 1.1 that Λ_{dB} is inversely proportional to the square-root of the temperature. This means that at high temperatures (for instance, room temperature) the De Broglie wavelength is small, so the gas can be described classically. However, at sufficiently low temperatures the De Broglie wavelength becomes of the order of the inter-particle spacing, which means that the gas should be described quantum-mechanically (see Ref. [1]). This is because the wave functions of the particles start to overlap. When the gas consists of particles with an integer spin (bosons), a fraction of the particles will, when the temperature is lowered to the critical temperature T_c, condense to a Bose-Einstein condensate. This temperature is in the order of μK, so the system can be described by one many-particle wave function.
The three different topics discussed in this thesis are *spin drag*, the magnetic trap and the particle flux of the oven. The first thing one needs if one wants to create a Bose-Einstein condensate in the setup used, is particles (for a schematic representation of the setup and thereby the terminology used below, see Figure 2.1). In this case, sodium particles are used. The measurements involving particle flux are performed to obtain a better insight in the operation of the oven as a function of the temperature of this oven. Also, the effect on the particle flux (and particle velocity in the atomic beam) of the power of the Zeeman laser beam is investigated. It turns out that scattering effects between the oven and the BEC chamber are more important than previously assumed. If the particles are in the BEC chamber, there needs to be a way in which they can be trapped and manipulated without immediately raising the temperature (i.e. no contact with the walls of the BEC chamber is allowed). This is done using a magnetic trap, which is the second topic of this thesis. This topic also includes a way to find out what small perturbations do to the magnetic field of the trap. This is useful because it provides a model for how the magnetic trap *should* theoretically be, and with this model it is possible to find explanations for why the magnetic trap operates in a different way. The simulation on which this topic is based can also be used to calculate the behavior of several magnetic field components, which is a useful tool when doing experiments. With the code, a good value for a certain magnetic coil can be calculated and the effects of increasing or decreasing a field can immediately be shown. The main subject of this thesis is an experiment involving spin drag below the critical temperature T_c. Spin drag is an entirely new field of research, but the experiment performed before were always performed above

T_c. When the temperature is decreased below T_c, several new interesting phenomena occur, such as *domain walls*.

1.1 Structure of the thesis

First, in Chapter 2 some general aspects concerning the Bose-Einstein condensate setup are discussed. These aspects are not directly related to the experiment described in Chapter 3, so they are included in a separate chapter. In Chapter 3 the experiment involving spin drag below T_c is discussed. It starts with a theoretical description of the relevant part of the experiment, described in Section 3.2. In Section 3.4 the results are presented by providing two different ways of analyzing the data. In Chapter 4 an analytical way to calculate the magnetic field of the magnetic trap is presented, including the derivation of the expressions used in this calculation. It provides a 'guidebook' which is based on a simulation. In this simulation, by varying the currents through the various magnetic coils (and by adding gradients in several directions and magnitudes), the characteristics of the magnetic trap can be investigated and trap frequencies can be calculated. The code is also used to calculate the forces used in Chapter 3. In Chapter 5 several experiments involving both fast and slow particle flux from the oven to the vacuum chamber are described and analyzed. In the Appendices a table of relevant constants can be found, plus some more background information about elliptic integrals and some lengthy expressions which are related to Chapter 4. The chapters, except Chapter 2 which is for readers unfamiliar with this field of research, in this thesis can be read in random order and are (mostly) independent of each other.

Chapter 2

The setup

In this chapter, the relevant parts of the Bose-Einstein condensate setup are discussed. First, the formation of a Bose-Einstein condensate is discussed (Section 2.1), then two different kinds of traps which can be used in experiments are described (see Sections 2.2 and 2.3). For the reader who is already familiar with the Bose-Einstein condensate setup and its general concepts, this chapter can be skipped.

2.1 The formation of a Bose-Einstein condensate

In the experiment, a Bose-Einstein condensate is formed from a sodium source which is located in an oven. When this source of sodium is heated, a beam of sodium particles is formed which is directed towards the BEC-chamber by using several diaphragms (see Figure 2.1). On its way to the vacuum chamber, the beam goes through a Zeeman slower. The Zeeman slower consists of a (near-resonant) laser beam which counter-propagates the beam of particles and of coils which induce a certain magnetic field. Due to the interactions between the laser beam and the particles, the particles are slowed down. However, this speed also induces a Doppler shift, which is being compensated by the magnetic field of the coils. In that way, the atoms are on resonance with the laser beam during the whole trajectory of the Zeeman slower. When they enter the BEC chamber, they are trapped by a magneto-optical trap (MOT), which consists of 6 propagating laser beams: 2 beams for each Cartesian axis, all directed towards the center. Using this principle, the atoms that move away from the center are directed back towards the center and thus cooled down to even lower temperatures. Subsequently, the atoms are transported to a magnetic trap (see Section 2.2) in which experiments can be done. Spin drag experiments are performed in an optical dipole trap (see Section 2.3).

2.2 The magnetic trap

For a wide variety of experiments, the magnetic trap (MT) can be used. It is created by using several magnetic coils through which different currents flow. This yields confinement of the atoms in both the axial and radial direction in an approximately harmonic trap. In Chapter 4 of this thesis, a method which analytically calculates the magnetic fields to create a magnetic trap is thoroughly discussed. By overlapping the MOT with the MT, the atoms in the MOT are transported to the MT. An important property of the MT is that it has a local minimum in the magnetic field. In the discussion about spin drag experiments, it is important to note that the atoms which are trapped in the MOT consist of a mixture of spin components $m_F = -1$, 0 and $+1$ with F the $F = 1$ electronic ground state. All these species react in a different way to a magnetic trap: the spin $+1$ particles are so-called high-field seekers, which means that for them it is energetically most favorable to be in a maximum of the magnetic field. Effectively, this means that spin $+1$ particles are accelerated in all directions, so they are lost. Particles which have spin 0 do not interact with a magnetic field at all, so they just fall through the magnetic trap due to gravity (hence they are also lost).

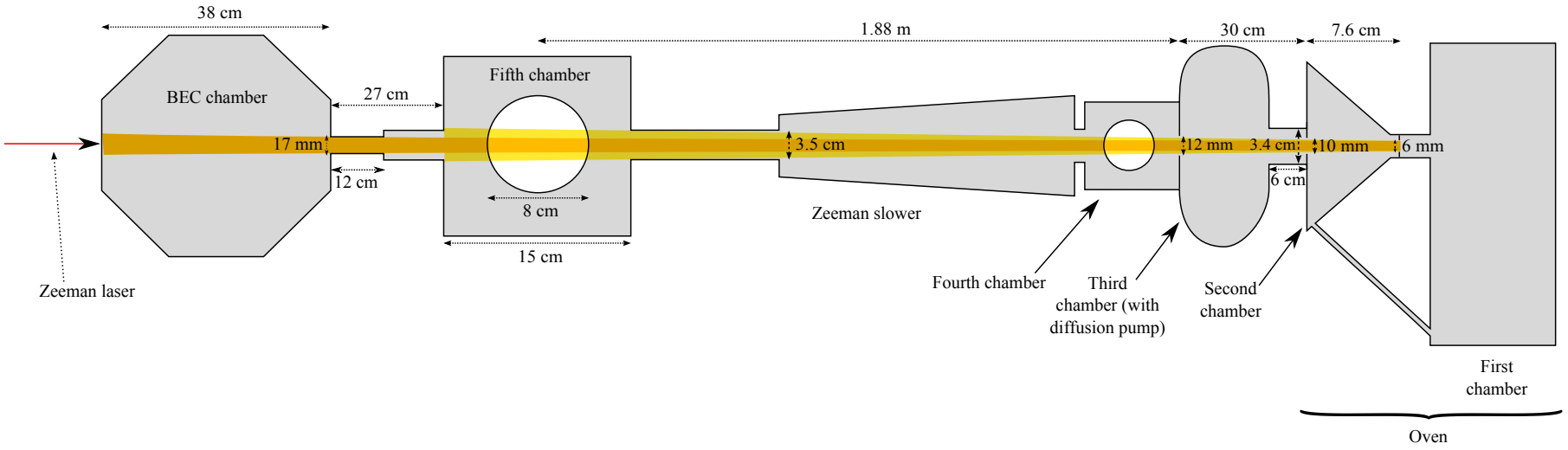

Figure 2.1: Overview of the setup used. The atoms move from the oven on the right-hand side towards the BEC chamber.

Finally, spin -1 are so-called low-field seekers, for which it is energetically most favorable to be in a minimum of the magnetic field. The magnetic trap accommodates such a minimum, so the particles with spin -1 are trapped and can be used to do experiments in the magnetic trap. To make a BEC in the MT, radio frequency (RF) cooling is used. For spin drag experiments, the magnetic trap is only an intermediate step.

2.3 The optical trap

In order to do spin drag experiments, it is necessary to have at least 2 different spin components. As discussed in Section 2.2, this cannot be achieved in a magnetic trap. Instead, it is necessary to have a trap in which atoms can be captured regardless of their spin. This can be achieved by an optical trap called the Far Off Resonant Trap (FORT). This trap, which is made by a laser beam with a wavelength of 1070 nm, causes the atoms to behave like electric dipoles. This laser beam is red-detuned with respect to the resonance frequency of sodium. The potential of the trap is, like the potential of the magnetic trap, approximately harmonic. Due to the AC stark effect, the energy levels of an atom trapped in the FORT shift apart from each other as a function of light intensity (see Ref. [2]). The atom, which is in the ground state, thus shifts towards an even lower energy level and therefore moves towards the focus of the laser beam profile, regardless of its spin. Spin drag experiments are thus always performed in the FORT.

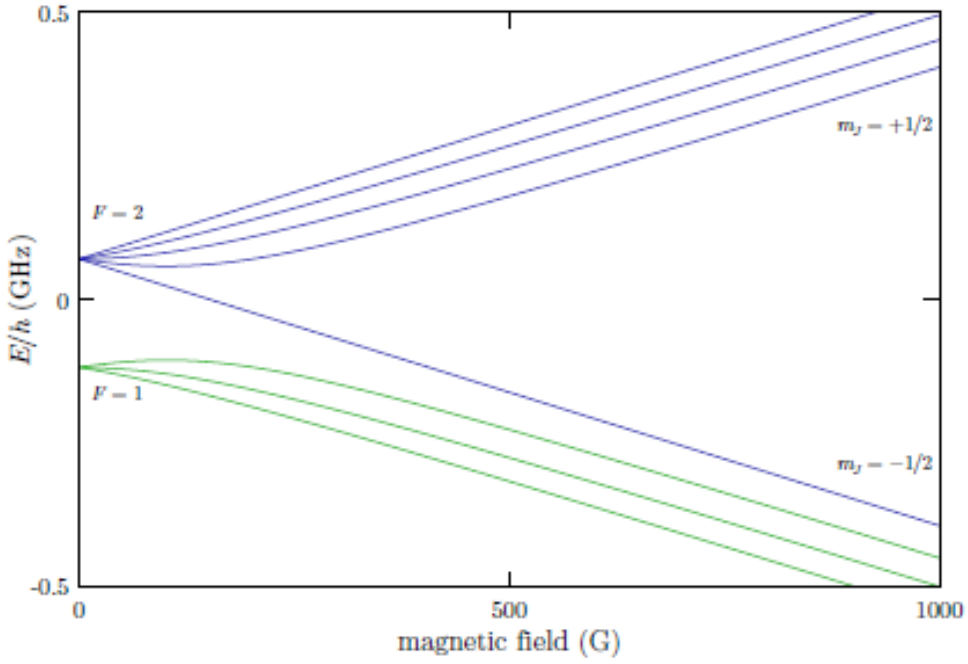

Figure 2.2: The energy as a function of the magnetic field (which is in this figure given in Gauss. 1 Gauss $= 10^{-4}$ T). In the experiment, the green $F = 1$ curves are used, in the regime with very small magnetic fields. The upper green curve indicates the $m_F = -1$ state, which in this regime increases with the magnetic field. The middle green curve indicates the $m_F = 0$ state (which is constant at very low magnetic fields) and the lower green curve indicates the $m_F = +1$ state, which decreases as a function of the magnetic field. The picture is taken from Ref. [3].

2.4 Separation of the spin components

To do spin drag experiments, two clouds of atoms must be present, one with spin -1 particles and one with spin 0 particles. The cloud of atoms is first transferred from the MT to the FORT;

after that, the MT is turned off. Then the MOT coils are turned on to create a homogeneous magnetic field, which makes that the spin components have a different energy as a function of this magnetic field. [3] For an illustration, see Figure 2.2. To create a homogeneous magnetic field, the current through one MOT coil is set clockwise while the current through the other coil is counterclockwise. For more details about the magnetic coils, see Chapter 4. The two spin species are separated by using a Landau-Zener transition. Now, there are two kinds of spin components in the FORT, which need to be spatially separated. This is also done using the magnetic field of the MOT coils, but in this step the current through one MOT coil is reversed, which causes a small magnetic gradient.

2.5 Evaporative cooling

In this Section, evaporative cooling in the FORT, which is essentially slowly lowering the depth of the trap, is described. Evaporative cooling is done by reducing the power of the FORT beam. When this is done, particles in the trap interact such that the energies of the particles is redistributed: one particle gets a higher energy than before the interaction, and thus escapes the trap, while the other gets a much lower energy. This means that on the one hand particles with a high energy are lost and on the other hand that in the same process, another particle gets a low energy. Therefore, the process of evaporative cooling is very efficient. In this case, two clouds are formed because there are both particles with spin -1 and spin 0. On top of that, the magnetic field of the finetuning coils is also turned on all the time, to make sure that two flipped spin 0 atoms do not (because of collisions) recombine into a spin $+1$ and a spin -1 atom. The principle of an evaporative cooling curve is illustrated in Figure 2.3.

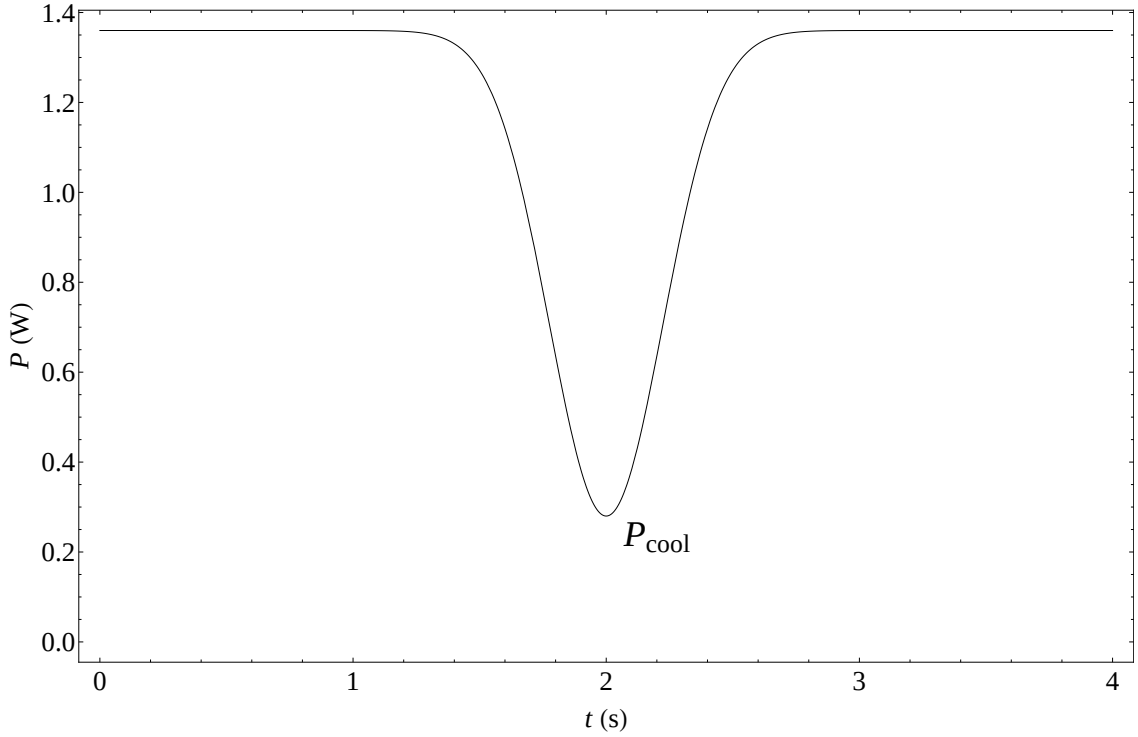

Figure 2.3: An evaporative cooling curve. During the evaporative cooling process, the power of the FORT is reduced to a certain minimum (this is P_{cool}), hence a minimal, tunable, temperature.

In Figure 2.3, two quantities of power are of importance. First, the minimum value of the evaporative cooling curve, which is denoted by P_{cool}. This quantity is used frequently in the text to distinguish between measurements which are performed at different temperatures of the condensate. The two powers used in the experiment described in Chapter 3 are 333 mW and 220

mW. These values are measured outside the BEC-chamber. To find the appropriate values inside the BEC-chamber, these powers must be multiplied by a factor 0.85 to correct for losses due to the windows of the BEC-chamber (see Ref [4, Section 5.2]). This yields values of 283 mW and 187 mW respectively. These values are used in the discussion in Chapter 3. Next, the final value of the power is important, which is *not* varied during the measurements. This is measured to be 1.6 W, after correction this is 1.36 W.

2.6 Applying the force

To generate a force which interacts with the spin -1 component, the magnetic field of the MOT coils is applied to interact with the cloud of these particles, causing a magnetic gradient, hence a force. The steeper this gradient, the larger the force. This is shown using the following relation:

$$\vec{a} = \frac{\vec{F}}{m} = g_F m_F \mu_B \frac{d\vec{B}(\vec{r})}{dz} \tag{2.1}$$

In this relation, g_F is the hyperfine Landé g-factor (equal to $-\frac{1}{2}$, this can be calculated from Eq. 4.49), m_F is the magnetic moment, m is the mass of a sodium atom and μ_B is the Bohr magneton (see Table A.1). During each measurement series, a temperature is chosen by setting the minimum value of the FORT evaporative cooling process. The time of applying the force was varied. After that, the MOT coils and the FORT are turned off and both clouds have a 30 ms time of flight, in which they both fall down towards the earth by gravity. Separation of the two spin components occurs due to the Stern-Gerlach splitting principle.

2.7 Imaging

Imaging the atoms is done by sending a resonant light beam through the atoms. The profile of the atoms is detected on a camera in the setup. These pictures indicate the transmission of the light, which is less than 1 if there are atoms. By using the Beer-Lambert law:

$$T = 1 - A = \exp\left(-\sigma \int \rho(x, y, z) dx\right), \tag{2.2}$$

the picture can be analyzed. Here, T is the transmission, A is the absorption, σ is the resonant absorption cross-section and ρ is the density. The analysis which can be done includes calculating the center of mass of a cloud, or the relative position of two clouds with respect to each other.

Chapter 3

Spin drag below T_c in a Bose-Einstein condensate

3.1 Introduction

Separate domains in a Bose-Einstein condensate are an interesting phenomenon to study. In a Bose-Einstein condensate, all atoms are normally in the ground state of the trap, i.e. the state which is energetically the most favorable. The electronic ground state of these sodium atoms is the $|F = 1, m_F = -1, 0, +1\rangle$ state. The first step to go from a cloud of trapped atoms to domain walls is to have at least 2 different spin components, such as -1 and 0, which is explained in Section 2.4. With two spin components, several interesting phenomena such as *spin drag* can be observed, which is discussed in more detail in Section 3.2. However, when the temperature of the cloud is below the critical temperature for Bose-Einstein condensation, domains are formed (see Section 3.2.2). It is thus interesting to do an experiment in which these domain walls form and in which control over them is gained. In this chapter, such an experiment is described. After a discussion about spin drag, the experiment itself is described, including the results, analysis and conclusion.

3.2 Theoretical description

Spin drag is an interesting phenomenon, in which a spin-dependent force is studied. The effect of spin drag is that one spin component, on which the force acts, interacts with the other spin component by momentum transfer. Some experiments (for example, see Ref. [5]) have already been performed in this field of research. In this Section, the theory related to spin drag experiments is described in more detail. Spin drag above $T = T_c$ is described in Section 3.2.1 and in Section 3.2.2, spin drag below T_c is discussed.

3.2.1 Spin drag above $T = T_c$

Experiments involving spin drag above the condensation temperature $T = T_c$ have already been performed (see Ref. [5]). In this Section, the experiments described in Ref. [5] are very briefly summarized. This gives the reader an idea of what knowledge is obtained by these experiments and thus the perspective in which the experiment described in this chapter can be placed. The experiments of spin drag above T_c are all performed at temperatures between 2 and 8 μK. Two methods are applied: firstly, the so-called constant force method, secondly, the oscillation method. In the constant force method, a constant (magnetic) force is applied which acts only on particles in the spin -1 state. The results are that the relative displacement of the particles with spin -1 and the particles with spin 0 is linear as a function of time. From these results, the spin drag rate γ can be derived. The other method, the oscillation method, is less relevant for the experiment described in this thesis. The reader is therefore referred to Ref. [5] for more details about this method, and about the full description of experiments above T_c.

3.2.2 Spin drag below $T = T_c$

In order to do spin drag experiments below T_c, one needs to have two BECs: in the case of the experiment described in this chapter, one BEC with spin -1 particles, and one with spin 0 particles. In the experiment, a spin-dependent force acts on the BEC with spin -1 particles and by momentum transfer, this BEC interacts with the BEC of spin 0 particles. Because condensates have different properties and behavior compared to thermal clouds, the results of this experiment are a way to find out what these differences are (and how they can be explained). The main differences between spin drag above and below T_c is that below T_c domain walls are formed. As explained in Ref. [6], for the two spin components -1 and 0, different collisions are possible: collisions with total angular 0, collisions with total angular momentum 1 and collisions with total angular momentum 2. The eigenstates for collisions with total angular momentum 1 change sign when two identical particles are exchanged. Because exchange symmetry states that, for bosons, the many-body wave function does *not* change sign when two identical particles are exchanged, the total angular momentum of two colliding particles must be either equal to 0 or 2. The interaction energy which plays a role during these collisions is equal to:

$$V_{\text{int}} = \frac{4\pi\hbar^2}{3M}\delta(\vec{r}_1 - \vec{r}_2)\left((a_0 + 2a_2) + (a_2 - a_0)(\vec{F}_1 \cdot \vec{F}_2)\right). \tag{3.1}$$

For sodium, the two scattering lengths are given by $a_0 = 46a_B$ and $a_2 = 52a_B$ with a_B the Bohr radius (see Table A.1). Furthermore:

$$\vec{F}_1 \cdot \vec{F}_2 = \begin{cases} -2 & \text{total angular momentum of colliding atoms equal to 0} \\ 1 & \text{total angular momentum of colliding atoms equal to -2} \end{cases} \tag{3.2}$$

The derivation is described in more detail in Ref. [6]. This result yields that the interaction energy between two atoms with spin 0 is lower than the interaction energies between either two spin -1 atoms or one spin 0 and one spin -1 particle, so it is energetically favorable for spin 0 particles to group together. This leads to the formation of domains. Above T_c, there is no condensate so in that case, domains do not form.

3.3 Experimental issues

Experimental physics is a process of doing something, finding out that some practical issue is not taken into account, trying again and repeating this process until the measurements are performed as was planned. Doing spin drag experiments below T_c is no exception, so in this Section a few of these issues are highlighted.

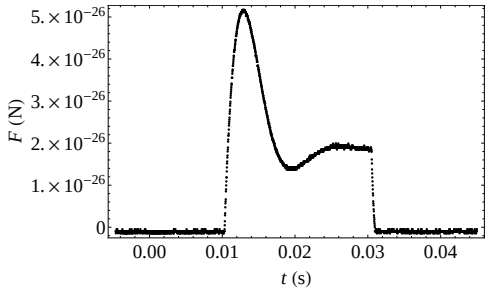

(a) A representation of the force profile which was used during the very first series of measurements. The undesired peak is clearly visible.

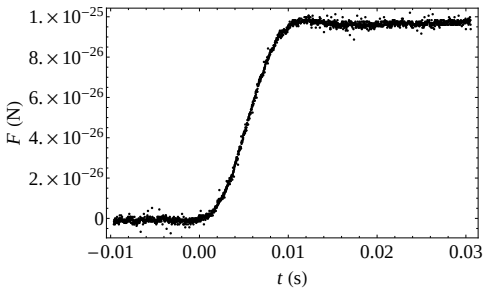

(b) A force profile used during the measurements series discussed in this thesis. The peak from Figure 3.1a has become much smaller.

Figure 3.1: Two different force profiles. The vertical axis shows the applied spin-dependent force.

3.3.1 The spin-dependent force

In Section 2.6, it is explained that the spin-dependent force, caused by a magnetic field gradient from the MOT coils, is supposed to be constant. However, a magnetic field gradient is applied by

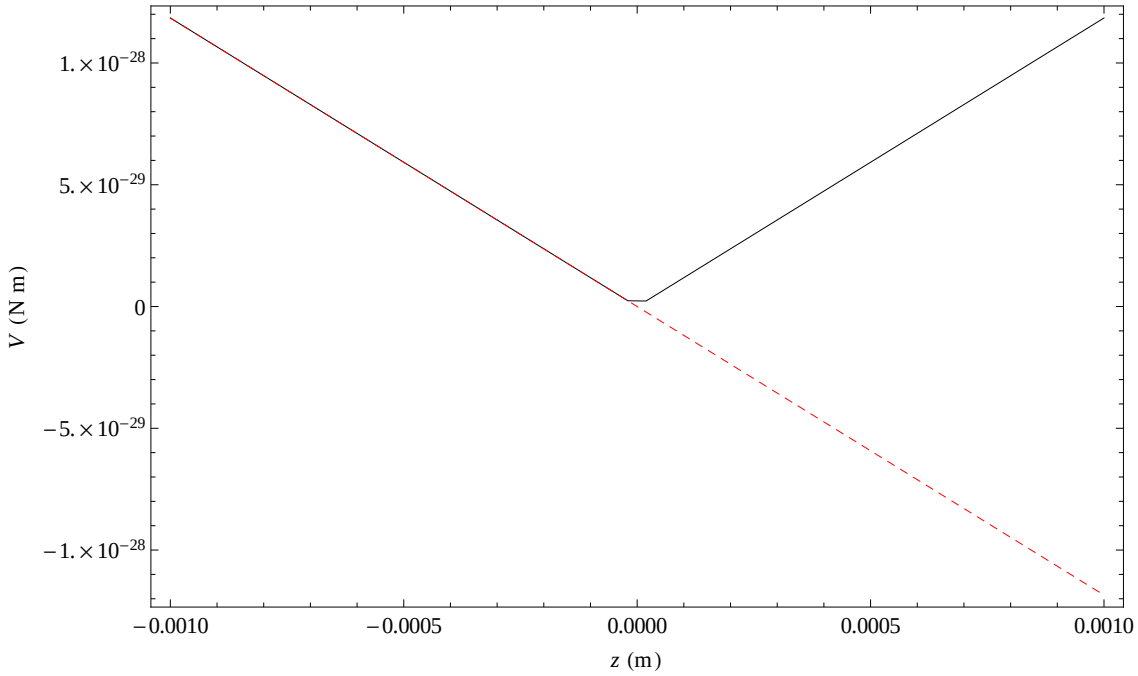

Figure 3.2: The V-shaped potential. The red dashed line indicates the gradient-like behavior of the magnetic field, whereas the black indicates what potential the atoms actually feel.

setting a current through the wires of the magnetic coils. The power supplies which are used for this have a response time of approximately 10 ms. This does not seem to be an important issue at first, but regarding the time scales used during the experiments, which are usually no longer than 30 ms, this is significant.
In the very first series of measurements (which are **not** further incorporated in the upcoming sections) a mistake in controlling the experiment was made, because the response time of 10 ms was not yet accounted for. As a result of this, the power supply did not get enough time to create a constant force, which caused an overshoot in the $F(t)$ profile after 10 ms. Before that overshoot, nothing at all happened. In Figure 3.1a, this profile is shown. Of course, this is an undesired artifact which was corrected by giving the power supply more time to establish a constant force. In all the other measurements series the response time is still present, but the overshoot in the profile is much smaller, making the experimental conditions better than before (as can be seen in Figure 3.1b). This profile also shows that between 0 and 10 ms of applying the force, the atoms are actually being pulled, albeit not yet at the desired force.

3.3.2 A V-shaped potential

Another experimental issue, also related to the applied spin-dependent force, is the potential associated with this force. If the force is given by Eq. 2.1, then the corresponding potential (with the assumption of adiabatic following) is given by:

$$V = g_F m_F \mu_B |\vec{B}| \tag{3.3}$$

Because the magnetic field of the MOT coils $B(\rho, z)$ is in an Anti-Helmholtz configuration and thus that $B(\rho, z = 0) = 0$, this means that at $z = 0$, the magnetic field changes sign. Because the potential is a scalar and the magnetic field is a vector, this means that the absolute value of the magnetic field is taken, which leads to a V-shaped potential. This is illustrated in Figure 3.2.

This leads to a force which changes sign for $z < 0$ and $z > 0$. Because in this experiment a constant force is assumed, this is an issue that needs to be solved. During the third (and final) measurements series, this issue is solved by turning on the finetuning coils also when the spin-dependent force is applied.

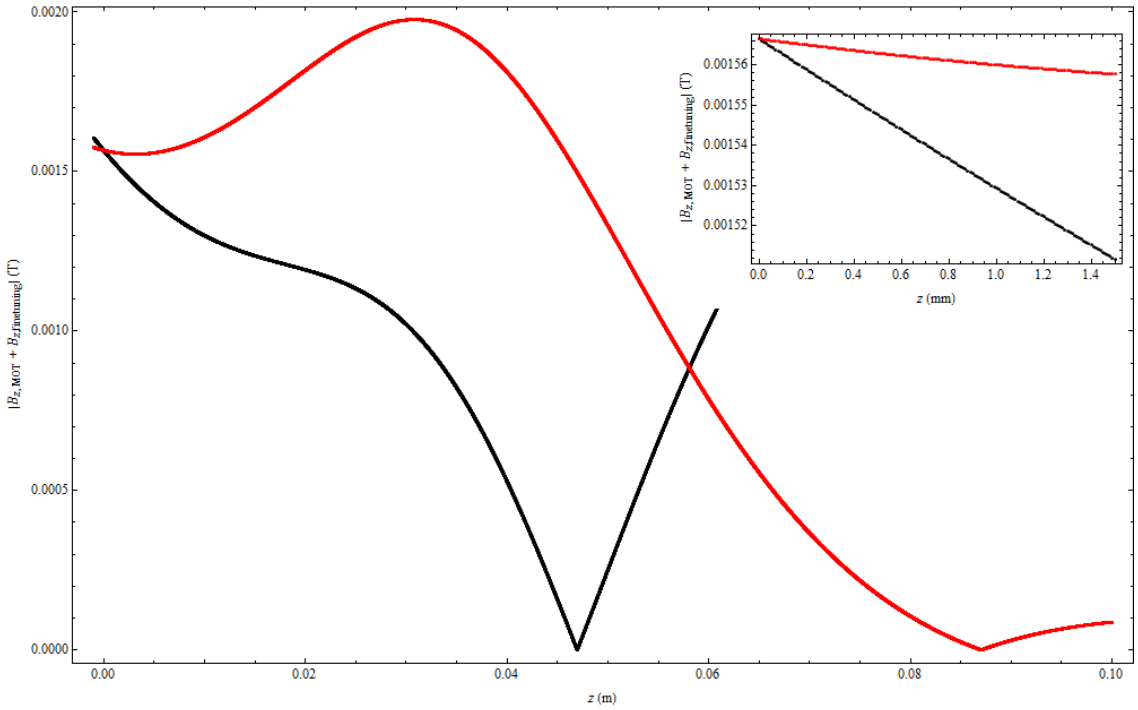

Figure 3.3: The absolute value of magnetic field resulting from both the finetuning and MOT coils. The black curve indicates the strongest force used in the experiment, the red curve indicates the weakest force. This graph shows that there *is* still a V-shaped potential, but the V is far away (order of cm) from the regions where the measurements are performed. In the inset, the region in which the experiments are performed, is shown. From this graph, it can be seen that the magnetic field in this region has a constant gradient.

The superposition of the magnetic fields of both MOT and finetuning coils provides a magnetic gradient, hence a constant magnetic force, which does not change sign in the area in which the measurements were performed (i.e. order of several mm). This can be seen in Figure 3.3, in which the inset zooms in on the region where the measurements are performed. This does not automatically imply that the second series of measurements (which was performed with a V-shaped potential) is bad and yields undesired results, it does however imply that these series are more difficult to analyze.

3.4 Results and analysis of the main experiment

In this Section, the results of the spin drag experiments below T_c are discussed. There are essentially two ways to gain information from the data: one is to look at the behavior of the domains walls themselves, the other is to look at the center of mass of the two clouds. Both methods supplement each other and together, they give a good insight in the dynamics of the interactions between two BECs with different spins. The two methods are explained in more detail in Sections 3.4.1 and 3.4.2.

3.4.1 Domain wall method

The domain wall method only uses one feature of each condensate: the domain wall. If both clouds were merged together, they would form a cigar-shaped condensate. Due to the fact that they are separated, two semi-cigar-shaped clouds appear. The cloud with spin -1 particles only, which appears on the left-hand side in Figure 3.4a, has a vertical domain wall on its right-hand side and the cloud with spin 0 particles only, which appears on the right-hand side in Figure 3.4a, has a vertical domain wall on its left-hand side. Initially, the distance between these domain walls is zero (in the picture, they are located above each other), but after applying the spin-dependent

force the distance $\Delta x \equiv x_1 - x_0$, as indicated in Figure 3.5, evolves over time. One of the major disadvantages of this method is that the two clouds deform after momentum transfer between the clouds has occurred, i.e. the clouds are no longer semi-cigar-shaped. This makes the determination of a domain wall in those cases difficult, and may lead to results which are less trustworthy. This is illustrated in Figures 3.4a and 3.4b, respectively.

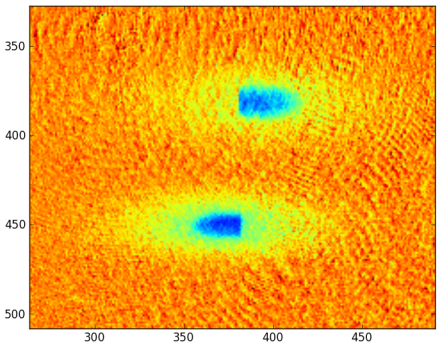

(a) An example of two clouds (upper: spin 0, lower: spin -1) with a well-defined domain wall. This is a typical picture for short periods of applying the spin-dependent force (or even no force at all).

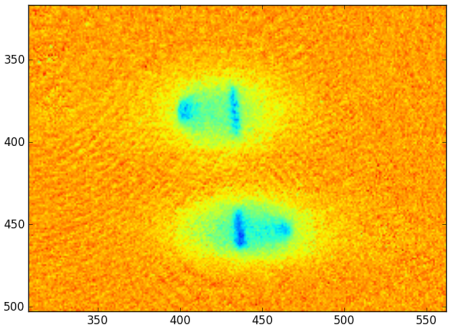

(b) An example of two clouds (upper: spin 0, lower: spin -1), where the domain wall is no longer well-defined. This occurs when the spin-dependent force is applied for a longer time.

Figure 3.4: Two pictures which are taken during the experiment.

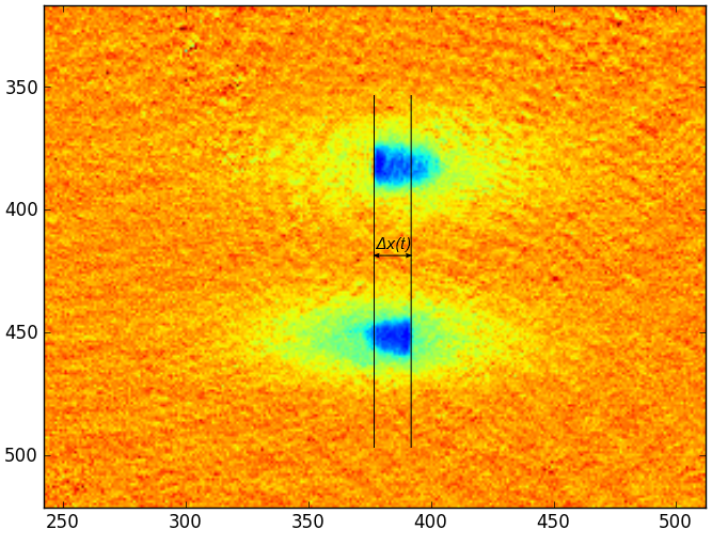

Figure 3.5: In this figure, the definition of $\Delta x(t)$, as used in the domain wall method, is defined.

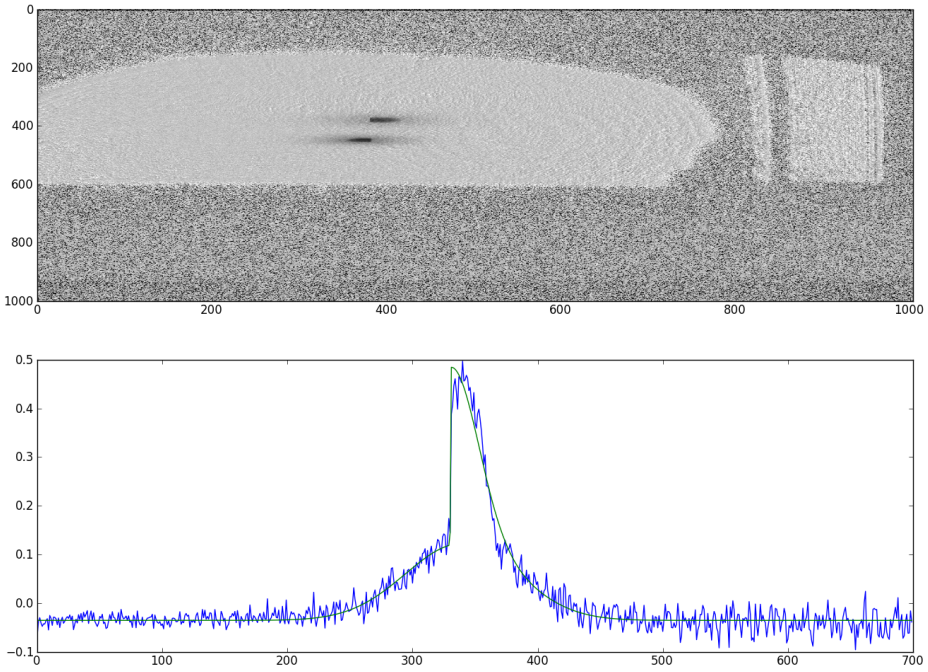

Figure 3.6: The upper part of the figure shows a picture of a measurement, featuring two spatially separated condensates. The lower part of the figure shows the absorption curve (blue) of the upper cloud, with spin 0. In green, a fit according to Eq. 3.4 is shown. The quantities on all axes are pixels (1 pixel = 23.2 μm), except the vertical axis of the lower part of the figure, which indicates the fraction of absorption.

Results and analysis of the domain wall method

To analyze the results of the domain wall method, the locations of the domain walls of both clouds must be determined. In order to do this, absorption imaging is used (see Section 2.7). For each cloud on the picture, the weighted average over the $y-$axis is taken. In that way, the cloud can be described by a one-dimensional absorption curve which consists of a (one-dimensional) Gaussian profile superposed with another Gaussian profile which is multiplied with a step function. This is because the thermal cloud can be described by a wide Gaussian profile and the condensate can be described by another, much narrower, Gaussian profile. Because the condensates are semi-cigar-shaped as shown in Figure 3.4a, this narrow Gaussian profile is multiplied by a step function. The fit function is thus:

$$G_{1D}(x) = C_1 + C_2 e^{-\frac{(x-x_1)^2}{2\sigma_1^2}} + C_3 e^{-\frac{(x-x_0)^2}{2\sigma_0^2}} \cdot S(x, x_0) \tag{3.4}$$

where C_1 is a constant indicating the offset, which is in the ideal case equal to 0. Furthermore, C_2 and C_3 are the amplitudes of both Gaussian contributions. The function $S(x, x_0)$ is given by:

$$S(x, x_0) = \frac{\arctan\left(C_4 n(x - x_0)\right)}{\pi} + 0.5 \tag{3.5}$$

where n is equal to either 1 or -1, depending on the location of the domain wall (which is either on the left- or right-hand side of the cloud). C_4 is a parameter which determines the steepness of the step function, which is 1000 because the step function must be steep. Also, $x_0 < x_1$. An example of a fit is shown in Figure 3.6. For the analysis, on both clouds the position of the domain wall is taken and they are subtracted, where $\Delta x(t) \equiv x_1(t) - x_0(t)$, these are plotted as a function of

time. From the slope of this curve, the relative velocity $\Delta v(t)$ can be determined. The slope is only determined from the points in which the drag is present. When the force is applied longer than the startup time (Figure 3.4b), momentum transfer between the two overlapping clouds occurs, yielding a nonzero and increasing relative displacement of the domain walls. This is the area of interest, in which a velocity can be determined. An example of such a fit is given in Figure 3.7.

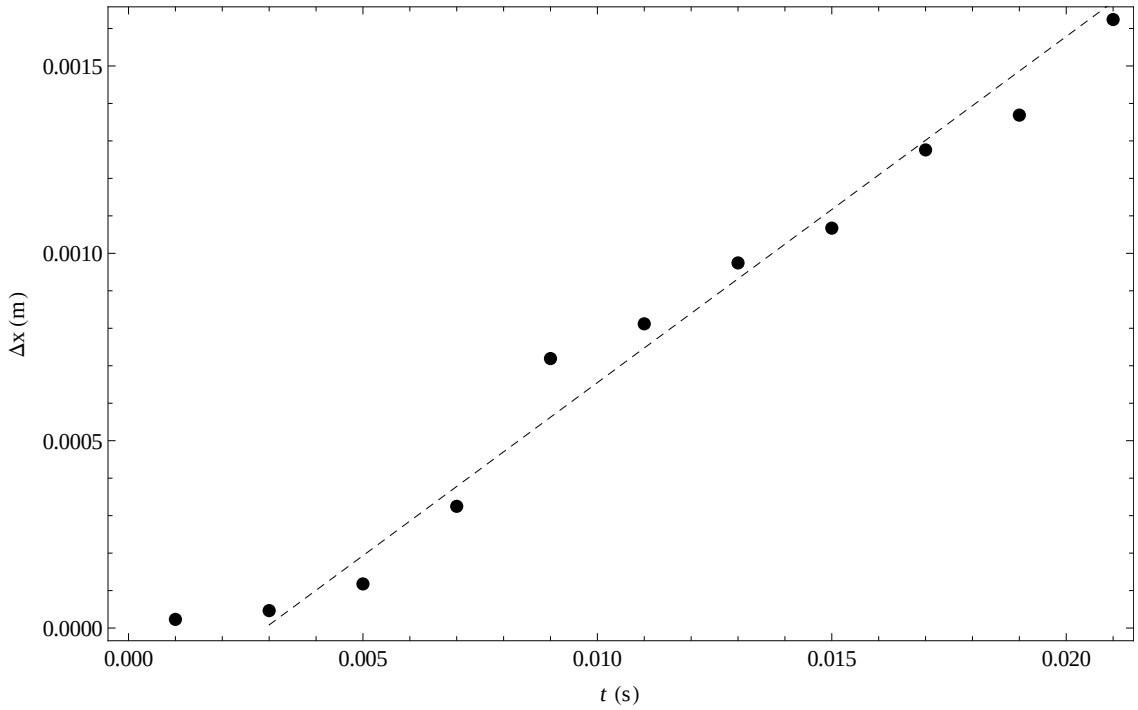

Figure 3.7: The data set of the relative displacement between the two clouds as a function of time. The power of the FORT in this data set is 283 mW, the applied spin-dependent force is $1.77 \cdot 10^{-25}$ N (i.e. the corresponding velocity is given in the 5th line of Table 3.1, this corresponds to an acceleration of 4.65 m s^{-2}). The errors bars in this plot are so small that they are almost indistinguishable, because the uncertainty in the determination of $\Delta x(t)$ is small.

A list of the relative velocities obtained from all the fits are given in Table 3.1. The pictures are usually comparable with Figure 3.7, therefore only one example of these graphs is given. When the acceleration resultant to the applied force is divided by this velocity, the 'domain wall drag rate' (unit s^{-1}, denoted by γ_D) can be obtained. This is given by:

$$\gamma_D = \frac{g_F m_F \mu_B \frac{d\vec{B}_{\mathrm{MOT}}(\rho,z)}{dz}}{v}. \tag{3.6}$$

For sodium atoms, a force of $1.18 \cdot 10^{-25}$ N corresponds with an acceleration of 3.10 m s^{-2}. The corresponding values of γ_D are also given in Table 3.1 and in Figure 3.8. In Section 3.6, this is further discussed.

P_{cool} (mW)	F_{MOT} (N)	Δv (m s^{-1})	γ_D (s^{-1})
283	$3.55 \cdot 10^{-26}$	0.0146 ± 0.0008	63.90
283	$5.92 \cdot 10^{-26}$	0.0273 ± 0.0073	56.77
283	$9.48 \cdot 10^{-26}$	0.0306 ± 0.0037	81.15
283	$1.18 \cdot 10^{-25}$	0.0617 ± 0.0018	50.32
283	$1.77 \cdot 10^{-25}$	0.0924 ± 0.0056	50.39
187	$3.55 \cdot 10^{-26}$	0.0201 ± 0.0033	46.42
187	$5.92 \cdot 10^{-26}$	0.0293 ± 0.0046	52.90
187	$9.48 \cdot 10^{-26}$	0.0537 ± 0.0026	46.19
187	$1.18 \cdot 10^{-25}$	0.0553 ± 0.0025	56.13

Table 3.1: The relative velocities which result from a linear fit to the data sets of the relative distance between the domain walls of the spin −1 and spin 0 clouds. Also, the 'domain wall drag rates' γ_D are given. The data sets are taken without a V-shaped potential.

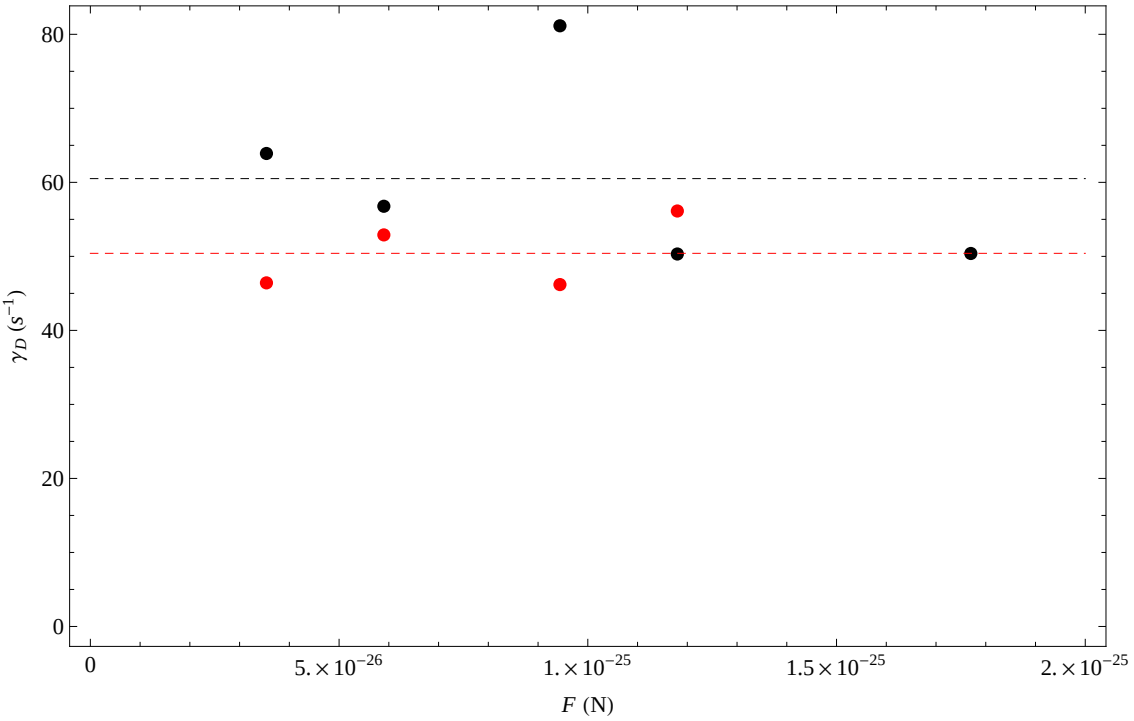

Figure 3.8: The domain wall drag rate γ_D as a function of the applied force by the MOT coils. The black points denote measurements series with $P_{\text{cool}} = 283$ mW, the red points denote measurements series with $P_{\text{cool}} = 187$ mW. The dashed lines are the averages of both sets of points, equal to γ_D =60.506 s^{-1} (black) and γ_D =50.41 s^{-1} (red).

3.4.2 Center of mass method

The center of mass method is a more in-depth method of analyzing the results, because it does not only take into account the location of the domain wall, but also the remainder of the cloud of atoms. The major disadvantage of the domain wall method, as explained in Section 3.4.1, is not much of an issue here, because regardless of the shape of the cloud, the center of mass can always be calculated. The center of mass is equally well defined for a compressed cloud with a tail at its end as for a semi-cigar-shaped cloud. In this method, the initial distance between the two centers of mass is nonzero and negative, because of the definition of Δx (the spin −1 cloud is located left of the spin 0 cloud), so $\Delta x(t = 0) = x_1(t = 0) - x_0(t = 0) = -\Delta x_0$ with Δx_0 a positive number. See also Figure 3.9. With this method, it is also possible to describe either only the condensate, or only the thermal cloud, or both together (with a given condensate fraction).

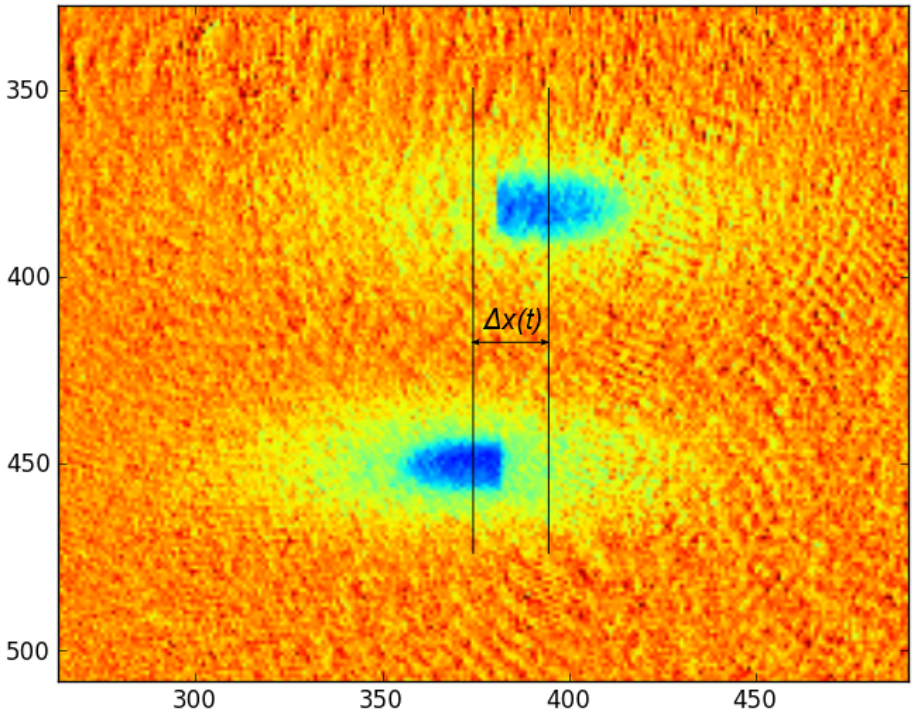

Figure 3.9: In this figure, the definition of $\Delta x(t)$, as used in the center of mass, is defined.

Results and analysis of the center of mass method

In order to analyze the results obtained by the center of mass method, the centers of mass of both clouds must be calculated first. These centers of mass can either be defined by the centers of mass of the 2 condensates, or by the centers of mass of the surrounding thermal cloud, or the total of both thermal cloud and condensate. To describe a system of two clouds, in which one cloud transfers its momentum to the other by a spin-dependent force in a trap, the following differential equation can be used:

$$\Delta x''(t) + 2\gamma\Delta x'(t) + \omega^2(\Delta x(t) + x_0) = \frac{F_{\mathrm{MOT}}(t)}{m} \tag{3.7}$$

with initial conditions $\Delta x(t = 0) = -\Delta x_0$ and $\Delta x'(t = 0) = 0$. Here, γ is the spin drag rate, ω is 2π times the axial trap frequency, which is calculated in Section 3.5.2, m is the mass of a sodium atom, Δx_0 is the initial separation between the two clouds (which is in the order of 100 μm) and x_0 is the location of the center of the Gaussian profile (see Figure 3.10). The term on the right-hand side of this equation is the acceleration as a result of the spin-dependent force. The second term on the left-hand side of the equation is the force caused by spin drag, which is directed in the opposite direction of the force. Finally, the third term on the left-hand side is the force as a result of the trapping potential, which is assumed to be approximately harmonic. Because the value of the trap frequency is small (2.91 Hz, see Section 3.5.2), this term only plays a role at time scales in the order of 300 ms. It is thus essentially a model which describes a damped harmonic oscillator. The force is time-dependent, as discussed in Section 3.3.1. In the model, this is incorporated by combining Eq. 2.1 with a force profile as shown in Figure 3.1b. The other free parameter is the spin drag rate. As a first approximation, the spin drag rate can be taken as a constant, independent of the overlap between the two condensates. Because there is also a thermal cloud present, which extends on a much bigger length scale, this approach can be characterized as the assumption that the thermal cloud is fully responsible for the spin drag rate,

and the condensate does not contribute at all. The spin drag rate can also be made a function of $\Delta x(t)$. This can be regarded as an overlapping function if one assumes that the spin drag in this experiment is fully due to the interactions of the condensate. At $t = 0$, the two condensates do not overlap at all, hence the drag should be zero. Depending on the magnitude of the force, there is a certain regime in time where the overlap between the two condensates increases, until they fully overlap. After that, the overlap decreases again and if the force is applied long enough, there is no overlap anymore. In first order approximation, this can be regarded as a triangle, with a basis of the typical size of a condensate, which is 1.39 mm (or 60 pixels). An analytical function which can be fitted to this shape is for example a Gaussian profile (which is illustrated in Figure 3.10), so γ becomes:

$$\gamma = \gamma_0 e^{-\frac{(\Delta x - x_0)^2}{2\sigma^2}}. \tag{3.8}$$

Here, x_0 is the displacement of the Gaussian shape, which is in this equal to zero, because when $\Delta x = 0$, the overlap is maximum, so the drag is largest. This same correction is also used in Eq. 3.7. Furthermore, σ is the width of the Gaussian profile. It can, however, be argued that another function fits just as well as a Gaussian profile, but the most important parameter of the overlapping function appears to be the width of the function.

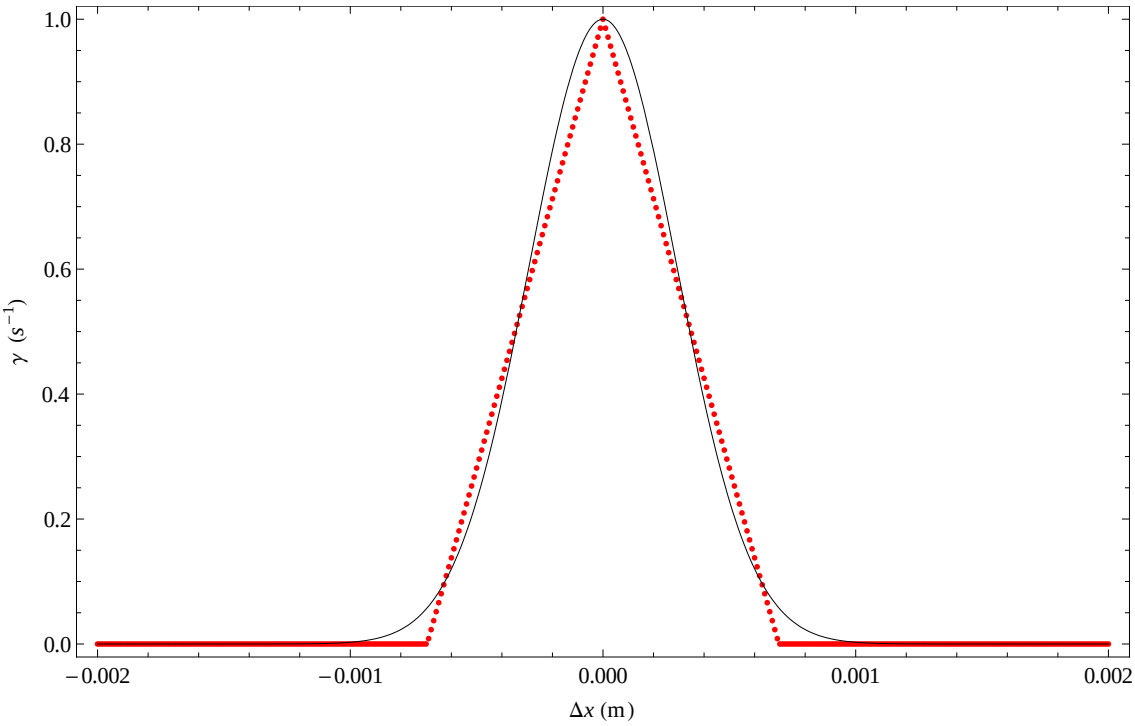

Figure 3.10: A Gaussian profile fitted to a triangular shape. The spin drag rate γ is normalized to 1 in this graph.

However, it appears that trying to reasonably fit any solution of Eq. 3.7 to the data obtained in this experiment fails, because if the force is turned off after the pre-set time, there is a time of flight period of 30 ms after which the picture is taken. In this period, the two clouds do not immediately stand still, but instead keep moving in the axial direction. From a number of measurement series it becomes clear that the relative distance $\Delta x(t)$ decreases after a certain time of applying the spin-dependent force. This phenomenon can also not be explained with the model of Eq. 3.7 alone. Because $\Delta x(t)$ is calculated at the moment the picture is taken, the extra movement due to the time of flight has to be taken into account. So for the analysis, γ (or γ_0, in the case of non-constant spin drag rates), is obtained by a superposition of the solution of Eq. 3.7 and the movement due to the time of flight t_{ToF}. In this equation, $\Delta x'(t)$ is also obtained from the solution

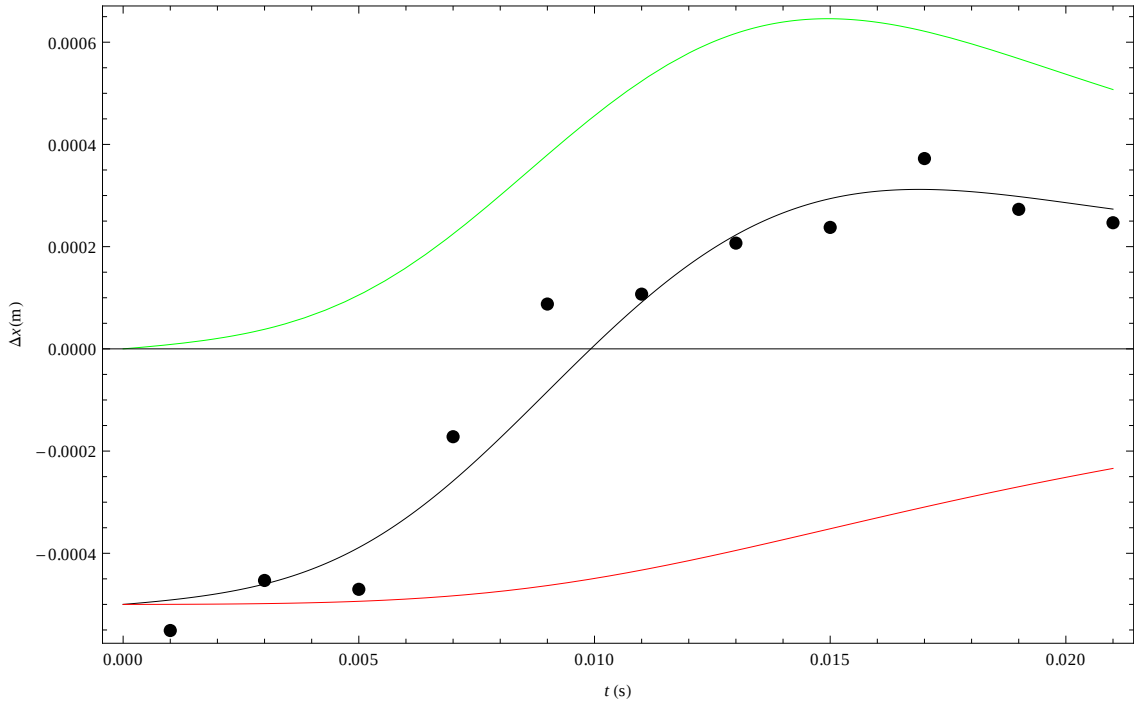

Figure 3.11: The data set with the relative displacement of the centers of mass of the two condensates as a function of time. When this data set was taken, the power of the FORT was 283 mW and the applied spin-dependent force was $1.77 \cdot 10^{-25}$ N. The fit was made using the assumption that the spin drag rate is a Gaussian distribution. The red line is the solution of Eq. 3.7, the green line is the correction term in Eq. 3.9 and the black line is $\Delta x_{\text{total}}(t)$ of Eq. 3.9.

of Eq. 3.7.

$$\Delta x_{\text{total}}(t) = \Delta x(t)|_{\text{Eq. 3.7}} + t_{\text{ToF}} \cdot \Delta x'(t)|_{\text{Eq. 3.7}}. \tag{3.9}$$

Both extreme cases outline aboved are used to find upper and lower values drag rates in the measurements. This is illustrated in Figure 3.11. In this figure, the red line is the solution to Eq. 3.7. It can be seen that this solution alone does not go through the data points at all, as already pointed out above. The correction term in Eq. 3.9 is depicted in green and the sum of the green and red curve (which does go through the data points) is represented in black. In this graph, after about 18 ms of applying the force, the relative displacement decreases again. Therefore, it is interesting to find out what is predicted by the fit for the longer term. This is shown in Figure 3.12. From that figure, it becomes clear that the relative displacement eventually increases again. Figures 3.11 and 3.12 are one example of a data set with a fitted line. For completeness, the other measurement series are included in Appendix B.

Of course, both cases of the spin drag rate are different because if a constant drag rate is assumed, the system has much more overlap so the interactions between the two clouds can be spread along a wider space and time frame than when the drag is assumed to be only caused by the two condensates. In Table 3.2, the values of the spin drag rate found from Eq. 3.9 for both cases of each measurements series are given. Because the exact dependance of the overlap function is unknown, the 'real' drag rate is probably somewhere between these two extreme cases. This will be further discussed in Section 3.6. The drag rates from Table 3.2 are also presented in Figures 3.13 and 3.14.

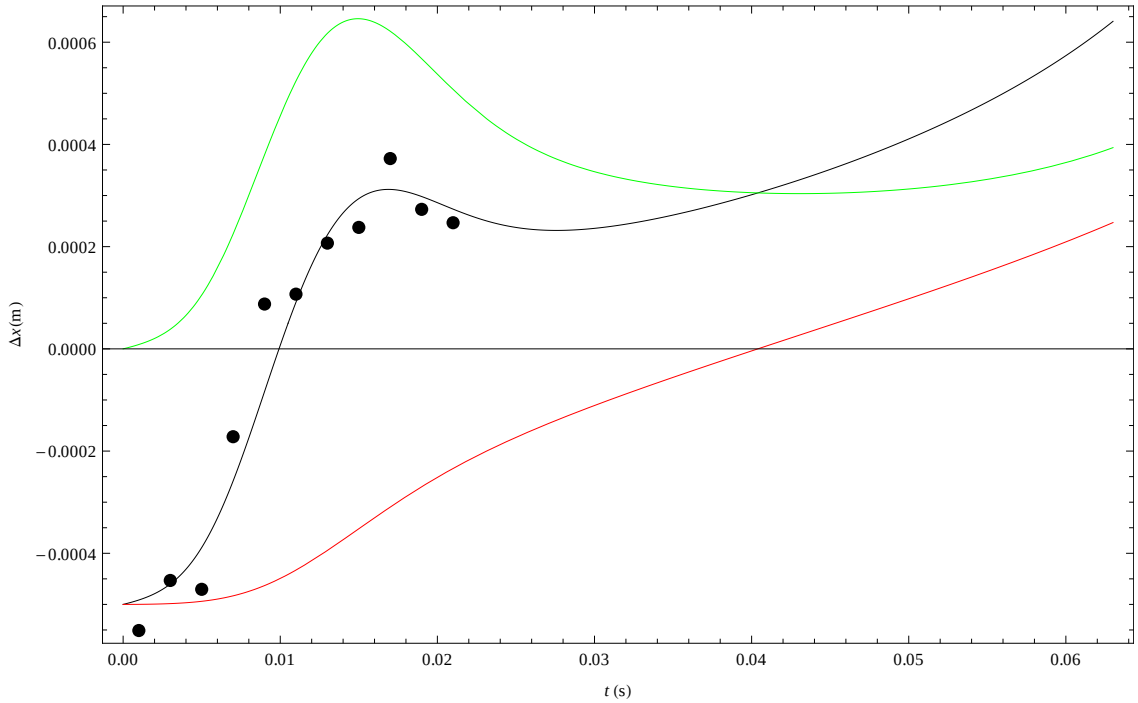

Figure 3.12: This graph represents the same data (and the same fits) as Figure 3.11, but is instead extrapolated for applying the spin-dependent force three times as long.

P_{cool} (mW)	F_{MOT} (N)	γ_0 (Gaussian) (s^{-1})	γ (constant) (s^{-1})
283	$3.55 \cdot 10^{-26}$	159.757 ± 88.853	106.966 ± 45.950
283	$5.92 \cdot 10^{-26}$	181.171 ± 83.682	53.582 ± 19.379
283	$9.48 \cdot 10^{-26}$	260.616 ± 172.464	71.647 ± 14.142
283	$1.18 \cdot 10^{-25}$	184.479 ± 48.875	45.470 ± 12.278
283	$1.77 \cdot 10^{-25}$	244.786 ± 55.056	65.455 ± 14.068
187	$3.55 \cdot 10^{-26}$	198.785 ± 171.258	142.894 ± 66.98
187	$5.92 \cdot 10^{-26}$	211.184 ± 146.365	76.456 ± 18.477
187	$9.48 \cdot 10^{-26}$	198.302 ± 42.951	86.958 ± 27.864
187	$1.18 \cdot 10^{-25}$	183.93 ± 37.89	54.895 ± 12.555

Table 3.2: The spin drag rates from the fits to Eq. 3.9. As a function of both P_{cool} and applied spin-dependent force, the spin drag rates for both extreme cases are given: a constant spin drag rate (i.e. the thermal cloud is entirely responsible for the spin drag rate) and a Gaussian spin drag rate (see Eq. 3.8, i.e. only the condensate is responsible for the drag). The values are from measurements series without a V-shaped potential.

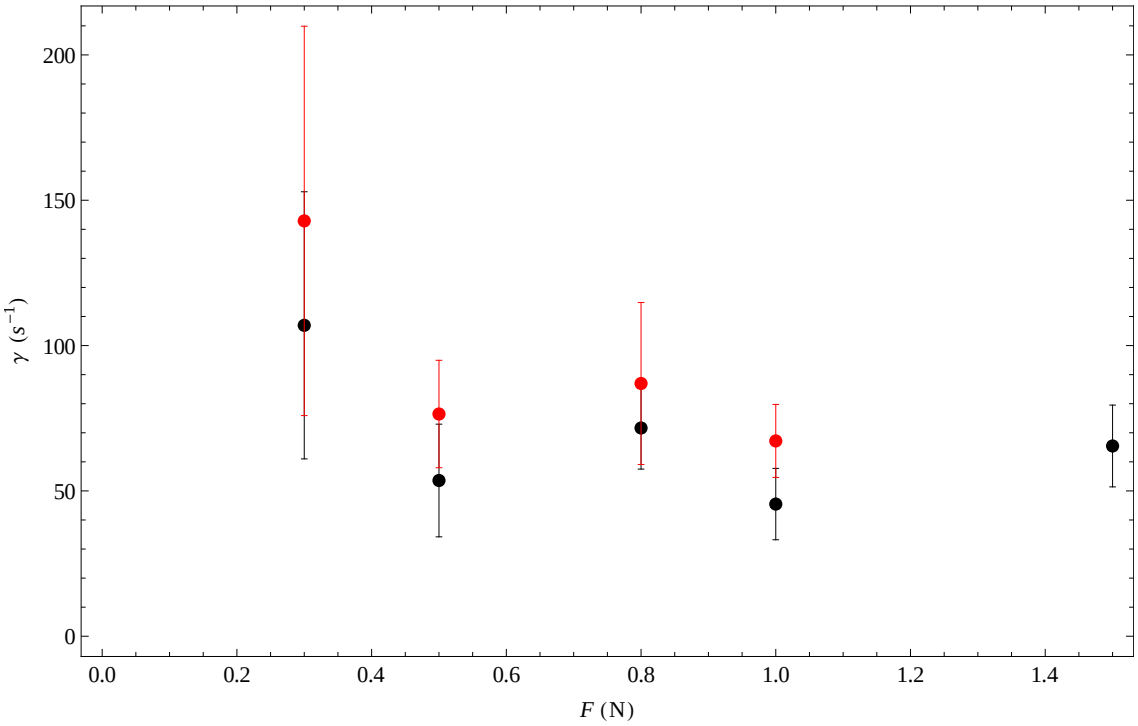

Figure 3.13: The spin drag rate γ as a function of applied spin-dependent force. The black points denote measurements series with $P_{\text{cool}} = 283$ mW, the red points denote measurements series with $P_{\text{cool}} = 187$ mW. The drag rates are assumed to be constant for these points.

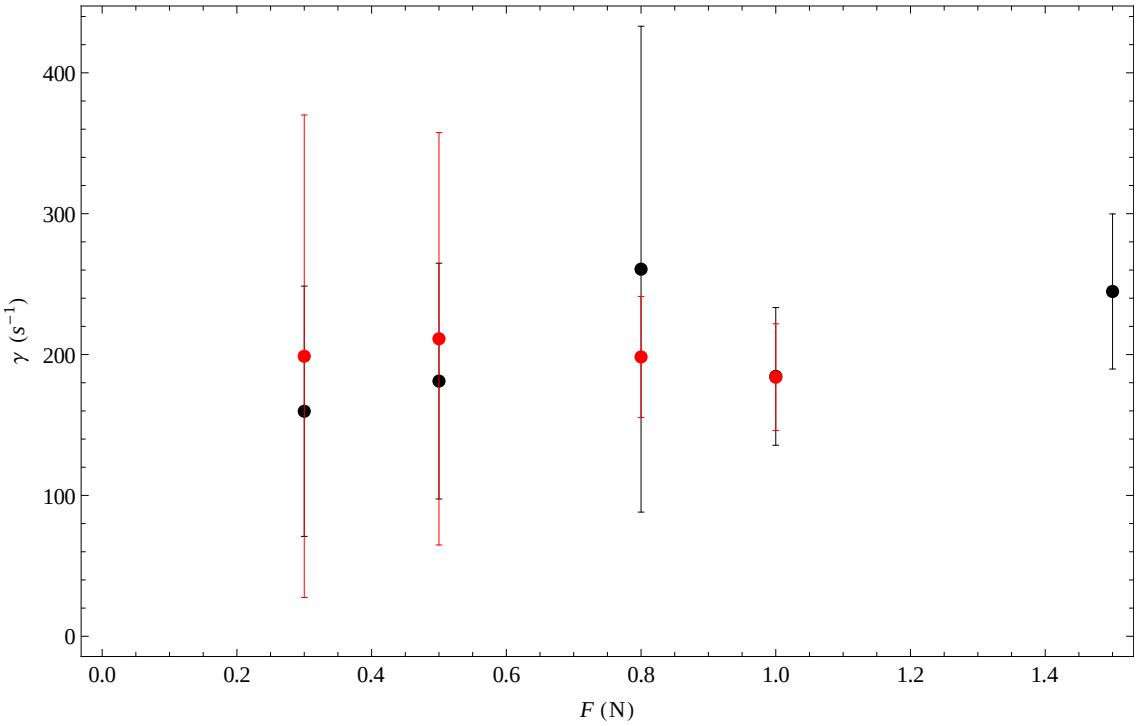

Figure 3.14: The spin drag rate γ_0 as a function of applied spin-dependent force. The black points denote measurements series with $P_{\text{cool}} = 283$ mW, the red points denote measurements series with $P_{\text{cool}} = 187$ mW. Here, the drag rates are Gaussian.

3.5 Secondary measurements

In this Section, some supplementary measurements which were done during the main experiment are described and discussed. This includes measurements of the temperature of the cloud (see Section 3.5.1), measurements of the trap frequencies (see Section 3.5.2) and a calculation of the chemical potential.

3.5.1 Temperature measurements

At each measurements series, the minimum value of the evaporative cooling curve of the FORT is set at a certain value to set the temperature of the series, as shown in Figure 2.3. From this value, it does not immediately become clear what the temperature (in μK) actually is; the value given is just a power (which is, in the measurement series discussed in Section 3.4, either 283 mW or 187 mW). To find out what the temperature really is, a series of pictures was taken with one BEC without applying a spin-dependent force. An example is shown in Figure 3.15.

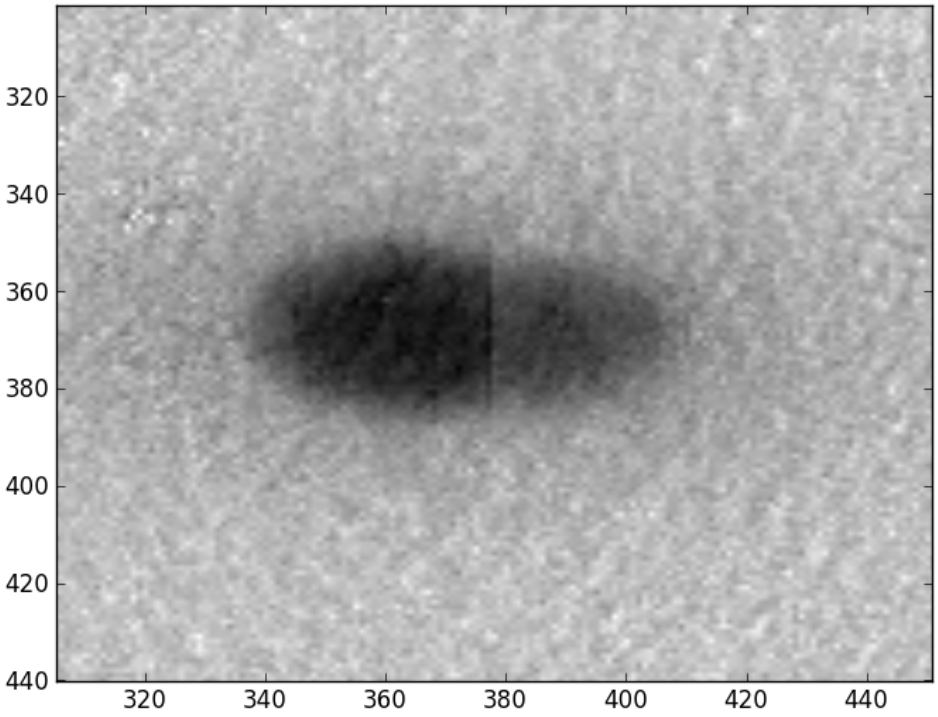

Figure 3.15: This figure shows one cloud of atoms with the two spin components separated. The two components can be distinguished because of the difference in transmission, which is due to the difference in absorption cross-section, of the two semi-cigar-shaped structures.

These images are further processed by a fitting module, which cuts out the condensate and fits a 2-dimensional Gaussian profile to the absorption profile of the thermal cloud, which is given by:

$$G_{2D}(x,y) = c_1 + \exp\left(-Ae^{-\frac{(y-y_0)^2}{2\sigma_y^2} - \frac{(x-x_0)^2}{2\sigma_x^2}}\right) \tag{3.10}$$

The temperature can be calculated using the following relation:

$$\frac{1}{2}mv^2 = \frac{1}{2}k_{\mathrm{B}}T \tag{3.11}$$

where m is the mass of a sodium atom, v is the speed, which can be related to the width of the Gaussian profile by $v = \frac{\sigma_y}{t_{\mathrm{ToF}}}$, where t_{ToF} is the time of flight, which is equal to 30 ms. In the case that the time of flight is zero, this relation cannot be used. Using this method, one can both relate the power of the FORT to the actual temperature, and one can also measure the temperature as a check before and after each measurements series. These control measurements are also used in Section 3.5.4. Also, a measurements series has been taken to find out what the temperatures are when the power of the FORT is varied. The results are presented in Figure 3.16. In this figure, a linear fit is shown. The slope of this graph is $9.43 \cdot 10^{-7}$ K/W.

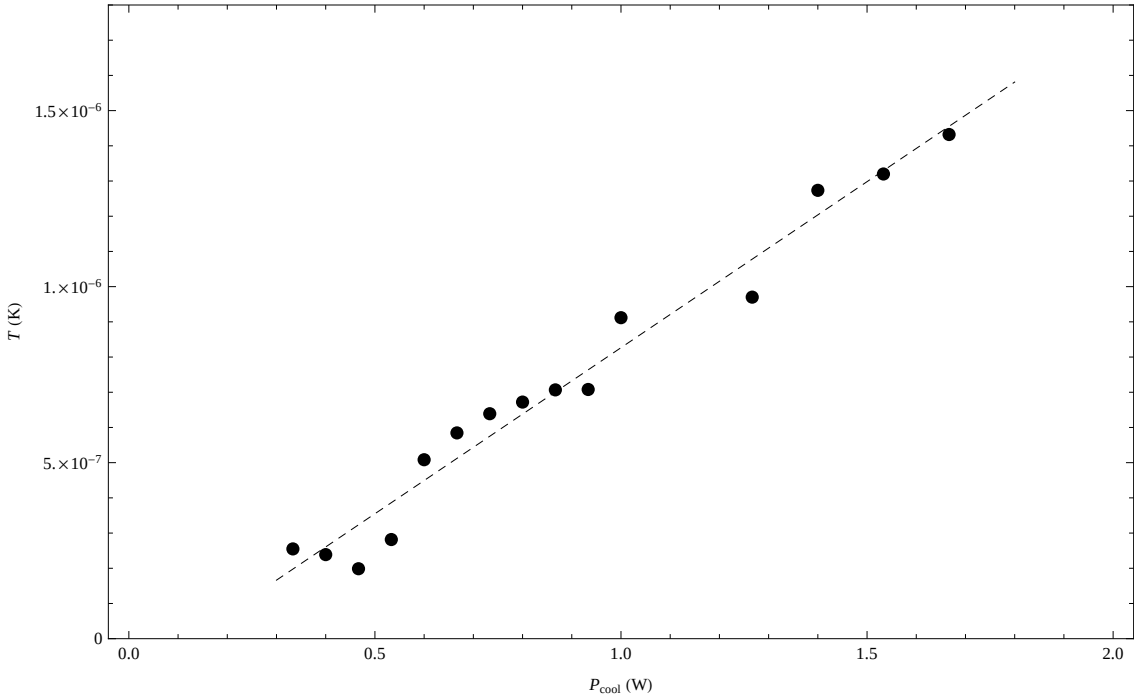

Figure 3.16: The temperature in the FORT as a function of the minimum power P_{cool} from Figure 2.3 of the FORT. The line is a fit through the data points.

3.5.2 Measurements of the trap frequencies

A good way to find out the characteristics of the FORT, is to measure its trap frequencies. There are 2 trap frequencies, the radial trap frequency and the axial trap frequency. The measurement of both trap frequencies is described in this Section.

The radial trap frequency

The radial trap frequency is measured by displacing a cloud of cold atoms into the radial direction, as a function of time. The time scales are in the order of 100 μs. A measurements series of the center of the cloud as a function of time is made, which is afterwards analyzed in the same manner as the temperature measurements. Again, a fit function like Eq. 3.10 is used to analyze the absorption. This time, the relevant parameter is x_0, the displacement in the $x-$direction of the cloud as a function of time. To these results, a sinusoidal function can be fitted:

$$x(t) = A \sin(2\pi f t + \phi) + x_0 \tag{3.12}$$

where A is the amplitude, ϕ is the phase, x_0 is the offset and f is the radial trap frequency. The result of this measurement yields 524.6 ± 3.9 Hz. In Figure 3.17, the curve from which this result follows, is displayed.

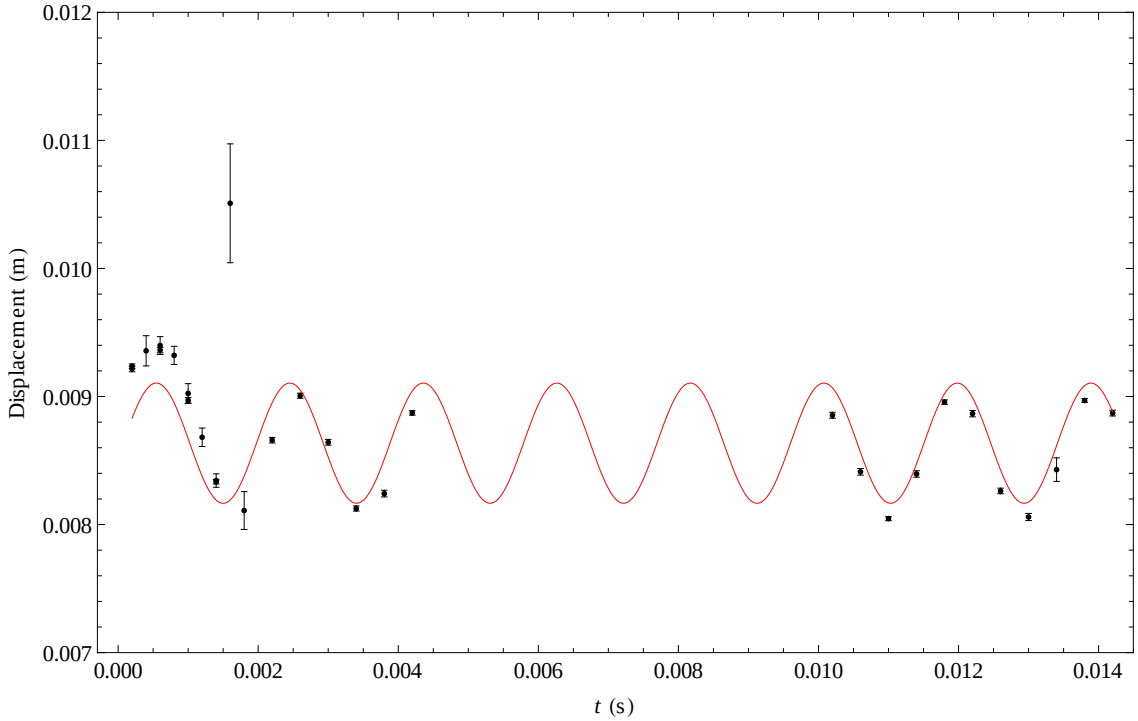

Figure 3.17: The displacement of the cloud in the radial direction as a function of time. The red line is a sinusoid, from which the radial trap frequency can be deduced.

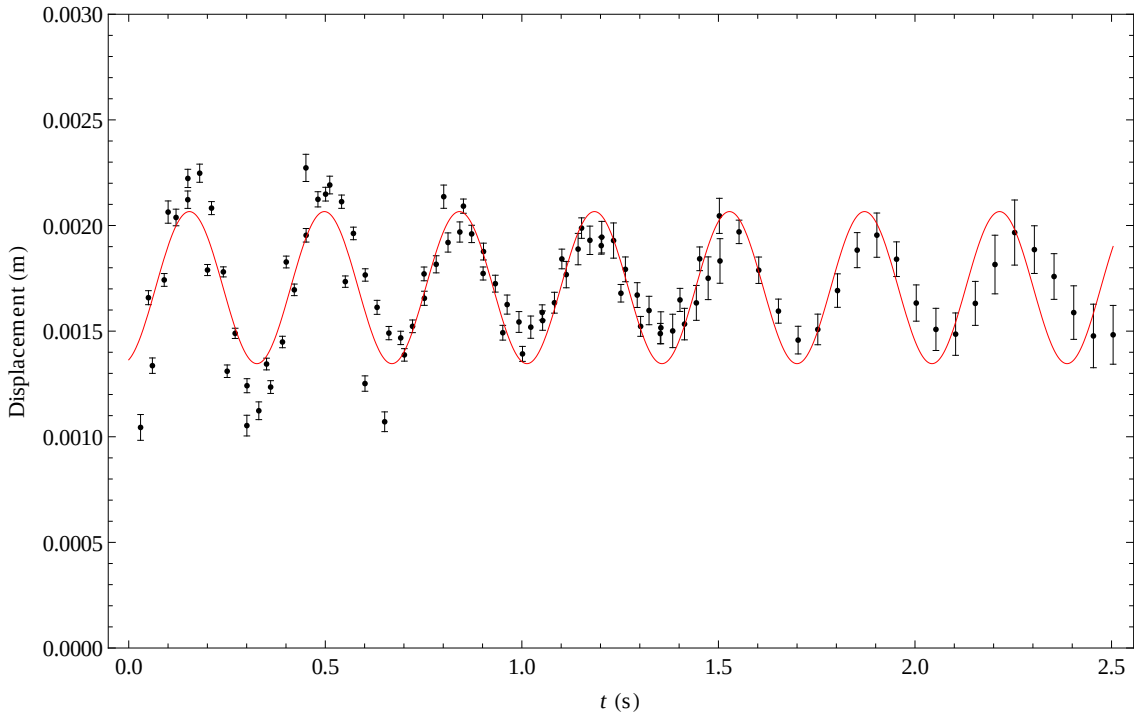

Figure 3.18: The displacement of the cloud in the axial direction as a function of time. The red line is a sinusoid, from which the axial trap frequency can be deduced.

The axial trap frequency

The axial trap frequency is measured in the same way as the radial trap frequency, but not in absorption side-imaging but in top-imaging, using a technique called phase contrast imaging, or PCI. This time, 2 measurement series of 50 pictures each were taken; in one series the time between two pictures was 50.08 ms, in the other series this time was 30.08 ms. These pictures were also analyzed using a fit function like Eq. 3.10, but the relevant parameter is now y_0. Again, a sinusoidal function for y_0 as a function of time was used to find the axial trap frequency, which turns out to be 2.91 ± 0.02 Hz. The curve which yields this result is shown in Figure 3.18.

3.5.3 Calculation of the FORT power from the trap frequencies

In Ref. [4], the radial and axial trap frequencies of the FORT are calculated from the focus of the laser, the Rayleigh length, the power of the laser and the trap frequencies. These relations can also be used the other way, to calculate the power from both trap frequencies separately.

The relation for the calculation of the power from the radial trap frequency is:

$$P = \frac{m\omega_\rho^2 w_0^4}{4C_{\mathrm{Na}}} \tag{3.13}$$

where w_0 is the waist of the beam, equal to $(44.44 \pm 0.192) \cdot 10^{-6}$ m, ω_ρ as calculated in Section 3.5.2 and $C_{\mathrm{Na}} = 4.55666 \cdot 10^{-37}$ m^2 s, which is a constant for sodium. The power calculated from this relation is $P = 0.88 \pm 0.02$ W.

The relation for the calculation of the power from the axial trap frequency is:

$$P = \frac{m w_0^2 z_R^2 \omega_z^2}{2C_{\mathrm{Na}}} \tag{3.14}$$

where all variables are already known, except z_R which is equal to $(5.52 \pm 0.14) \cdot 10^{-3}$ m. The power calculated from this relation is 0.84 ± 0.05 W. The values of z_R, w_0 and C_{Na} can all be found in Ref. [4].

3.5.4 The spin drag rate versus the chemical potential

In this Section, the spin drag rate is plotted against the chemical potential of the condensate. For clarity, first a distinction between two chemical potentials is emphasized: both a chemical potential of a thermal cloud and a chemical potential of a condensate exist. The chemical potential of a thermal cloud is always smaller than 0 and thus the fugacity (defined by $z = \exp \frac{\mu}{k_{\mathrm{B}}T}$) is between 0 and 1. At the transition to a Bose-Einstein condensate, the chemical potential of the thermal cloud becomes 0. In a Bose-Einstein condensate, interactions also play a role so the chemical potential *can* increase to values larger than 0.
In Ref. [5, Pages 104-106], the chemical potential of the thermal cloud is used in a graph of the spin drag rate, divided by the square of the temperature in μK, versus the fugacity. The data follows a theoretical predicted line of a quantum mechanical model. This is in contrast with the classical model, which is a straight line (the quantum mechanical model predicts higher drag rates for higher z than the classical model).
In this experiment, the spin drag rate is determined for temperatures below T_c. Therefore, in this Section the chemical potential of the *condensate* is calculated and compared to the spin drag rate divided by the square of the temperature. In order to find these points on a graph, the following quantities must be known:

- The spin drag rate
- The temperature
- The chemical potential

From these quantities, the spin drag rate follows from Table 3.2 and the temperature is calculated from the temperature measurements using the method outlined in Section 3.5.1. For the vertical coordinate of each point, the temperature must be given in μK.

Calculating the chemical potential

The chemical potential follows from a calculation involving the number of particles. In the Thomas-Fermi approximation for zero temperature, the relation between the number of particles and the chemical potential is (see Ref. [1]):

$$N = \frac{8\pi}{15}\left(\frac{2\mu}{m\bar{\omega}^2}\right)^{3/2}\frac{\mu}{U_0}. \tag{3.15}$$

Here, N is the number of particles, μ is the chemical potential, $\bar{\omega}$ defined as $(\omega_\rho^2\omega_z)^{1/3}$, with ω_ρ and ω_z as measured in Section 3.5.2 and $U_0 = 1.02\cdot 10^{-50}$ J m^3. The relevant solution of Eq. 3.15 with respect to μ is:

$$\mu = \left(\frac{225}{512\pi^2}(NU_0\omega_z)^2 m^3\omega_\rho^4\right)^{2/5} \tag{3.16}$$

The calculation of the number of particles is separated into two parts: the calculation of the number of particles in the thermal cloud and the calculation of the number of particles in the condensate. This is done for both the cloud of particles with spin -1 and the cloud of particles with spin 0. In both cases, the part where the cloud is, is cut out of the picture which is made by absorption spectroscopy. The pixels, which have values between 1 (no absorption at all) and 0 (infinite absorption), are then divided into two groups: pixels which have a value between 1 and 0.8, and pixels which have a value lower than 0.8. The reason for this is the distinction between the thermal cloud and the condensate. The pixels with values between 1 and 0.8 are part of the thermal cloud and pixels with a value less than 0.8 are part of the condensate. The first group is analyzed using the exponential of a 2-dimensional Gaussian profile, which takes only these pixels into account, not the ones which are lower than 0.8. The contribution of this thermal cloud is given by:

$$N_{\text{Thermal cloud}} = \frac{2\pi A\sigma_x\sigma_y}{\xi_i}, i = -1, 0 \tag{3.17}$$

Here, A is the amplitude of the Gaussian profile, σ_x and σ_y are the widths of the profile in the $x-$ and $y-$direction, respectively. Furthermore, ξ_i is the scattering cross-section for spin -1 and spin 0 particles, which is given by:

$$\sigma_i = f\frac{3\lambda^2}{2\pi} \tag{3.18}$$

with λ the wavelength of sodium, and f the polarization-dependent Glebsch-Gordan coëfficient. These constants are measured by comparing an absorption picture with a PCI picture. The coëfficients are fit parameters in the analysis to match the two pictures. Therefore, other effects, like Zeeman shift, are also incorporated in these constants. For the spin 0 particles, this factor is equal to 0.145 and for the spin -1 particles, it is 0.212.
The second group of pixels is determined by making a list of the values of all pixels, of which the pixels with an absorption less than 0.8 are assigned a weight of 1, and the other pixels are assigned a weight of 0. After that, the remaining absorption values (with weight 1) are added and by using the relation:

$$N_{\text{Condensate}} = \frac{1}{\sigma_i}\left(\sum_{\text{pixels}}\log\frac{1}{1-A}x_p^2\right) \tag{3.19}$$

where σ_i is as defined above, A is the absorption value of the pixel and x_p is the length of a pixel, which is $8\cdot 10^{-6}\cdot 2.9$ m, so x_p^2 is the area of one pixel.

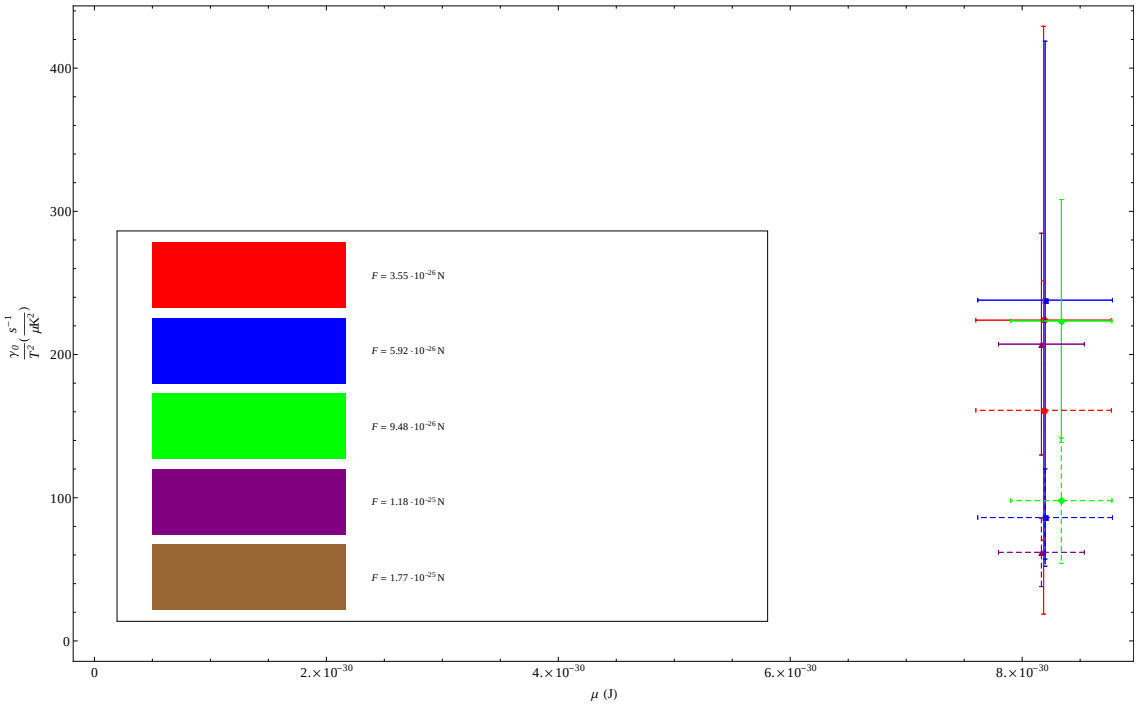

Figure 3.19: The spin drag rate (normalized by the temperature) as a function of μ. The minimum power of the evaporative cooling curve is 283 mW. The dashed points result from fits with a constant spin drag rate, the solid points result from Gaussian distributed spin drag rates. The colors indicate different spin-dependent forces.

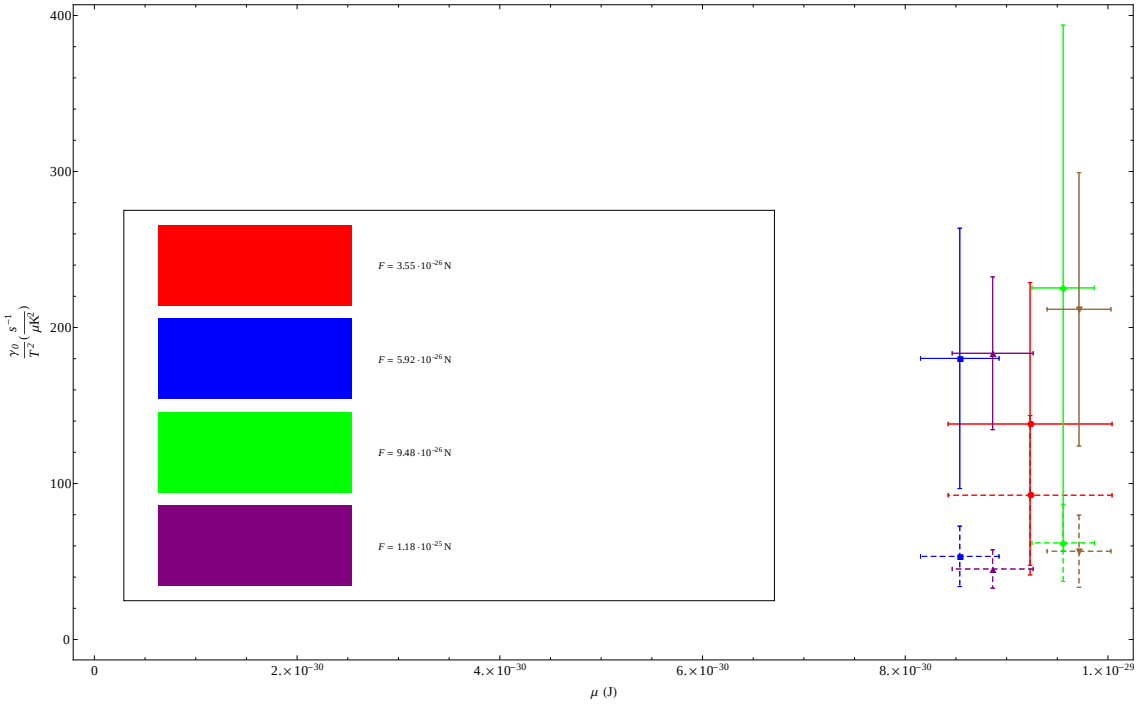

Figure 3.20: The spin drag rate (normalized by the temperature) as a function of μ. The minimum power of the evaporative cooling curve is 187 mW. The dashed points result from fits with a constant spin drag rate, the solid points result from Gaussian distributed spin drag rates. The colors indicate different spin-dependent forces.

However, the values of the Gaussian profile in these pixels must still be subtracted from the values obtained in this equation, because although these pixels were not used to determine the shape of the Gaussian profile, the Gaussian profile still is taken over *all* pixels. If the values of the Gaussian profile were not subtracted from the absorption values of the individual pixels, one would over-count these pixels. The method to prevent this is to insert the coordinates of the pixels in the Gaussian profile to determine the value of the Gaussian profile at these pixels, and then subtract these values from Eq. 3.19.

Results

This procedure results in a number of points on a $\frac{\gamma}{T^2}(\mu)$ graph. The results of the measurements are shown in Figures 3.19 and 3.20. In the inset, the colors used in the figures are explained. The points with dashed uncertainty bars are calculated using fits in which γ is constant (i.e. the thermal cloud is responsible to the spin drag rate), whereas the points with solid uncertainty bars are calculated using fits in which γ is given by Eq. 3.8 (i.e. the condensate is responsible for the spin drag rate).

3.6 Discussion

In this thesis, the spin drag experiment below T_c is analyzed in two distinct ways: the center of mass method and the domain wall method. In both ways of analyzing, a quantity with units s^{-1} can be obtained. In the center of mass method, this quantity is called the spin drag rate, and it is obtained by fitting the solution of the differential equation (Eq. 3.9) to the data points. In the domain wall method, the behavior of the domain walls is presented in a $\Delta x(t)$ diagram, on which a straight line (representing the relative velocity of the domain walls with respect to each other) is fitted. The value of this relative velocity is divided by the acceleration caused by the spin-dependent force. In this Section, one of the main questions is whether or not this resulting γ_D can be regarded as a spin drag rate. If so, what is it that can explain the difference between the results of this method and values obtained by the center of mass method? Another question (which is discussed first) is how the spin drag rate depends on the overlap between the two condensates.

3.6.1 Discussion about the center of mass method

The starting point of this discussion is, however, the center of mass method. This method has already been applied in the analysis of other spin drag experiments, including the spin drag experiments above T_c described in [5]. In [5], also a graph is shown in which the experimental data is compared with two models: a classical model described in [7], and a quantum mechanical model described in [8]. The data obtained by [5] does agree best with the quantum mechanical model. This graph has its upper limit at a thermal cloud fugacity equal to $z = 1$, where $\mu = 0$. As shown in Section 3.5.4, the condensate chemical potentials obtained in the experiment described in this thesis are all around the order 10^{-29} J. However, the values of $\frac{\gamma}{T^2}$ have a large spread (Figures 3.19 and 3.20). This is in the first place caused by the two separate assumptions which were made when the spin drag rate is calculated.

The **first assumption** is that the spin drag rate is caused by the condensed atoms only. The reason for this assumption is that if a condensate is present, it probably plays a role in the dynamics involved in spin drag. This assumption means that there may be a thermal cloud, which does not contribute anything to the spin drag rate. It also implies that the spin drag rate is not constant in time due to the fact that during a series of measurements the overlap is not constant. When the two condensed clouds do not overlap at all, the spin drag rate is zero, whereas when the overlap is maximum, the spin drag rate is maximum as well. This reasoning implies that a good way to model the spin drag rate as a function of overlap, is a triangular shape. However, a triangular shape is an idealized way to model this situation, because it implies that the two clouds are exactly rectangularly shaped. This is, of course, not the case. When the domain wall is well-defined, one side of the cloud is straight, but the remainder is semi-cigar-shaped. It can

be argued that this can be approximated as a rectangle, but this is only valid when the domain wall is well-defined. When the spin-dependent force is applied for a longer time, the domain wall becomes less well-defined and the shape of each cloud is no longer a semi-cigar. Instead, it is more like a compressed 'blob' in the middle with a tail at one side. In those cases, there is still some overlap. But the approximation of a triangular spin drag rate is in these cases difficult to justify. A solution to this could be to calculate the overlap as a function of time exactly. This is time-consuming because it has to be done for each data point separately. The most important parameter of the overlap function of the spin drag rate is the width of the (in this case) triangle. This is also supported by choosing the overlap function Lorentzian instead of Gaussian. While this is not discussed in this thesis in more detail, the spin drag rates obtained from this overlap function are of the same order of magnitude.

The **other assumption** is that the spin drag rate is determined by the thermal cloud only. The reason for this assumption is that there are theoretical models which state that the spin drag rate of a condensate is zero (see Ref. [9]). This assumption implies that the presence of condensed atoms in a spin drag experiment do not matter at all. This might draw the conclusion that the experiment could also have been done above T_c. It also implies that the spin drag rate is constant during the whole measurements series, because the thermal cloud stretches far outside the regions of the condensate. This means that the rate of momentum transfer is spread over a larger period of space and time, explaining the overall lower spin drag rates which are calculated for this situation.

3.6.2 Comparison with the domain wall method

The next question which is discussed here, is whether or not (if so, how) the results of the center of mass method can be related to the results of the domain wall method. From the results of the domain wall method, another quantity with unit s^{-1} can be derived. These 'domain wall drag rates' lay all between 45 and 85 s^{-1}, which partially agrees with the results of the center of mass method, constant spin drag rate. The reduced estimated variances (χ^2_{red}) are large: in the order of 10^6 to 10^8 which can be explained by the shot-to-shot fluctuations of the measurements. Both of these methods do not take the overlap as a function of time into account when the spin-dependent force was turned on, which might be an explanation for the agreement. Furthermore, because the frame in space and time is much larger for a domain wall (or a constant spin drag rate) than for a time-dependent overlapping spin drag rate (but the same amount of energy transfer takes place) these drag rates can be lower. It must, however, be noted that after the force is applied longer, the domain wall becomes less well-defined. This makes it more difficult and inaccurate to locate the coordinates of such a domain wall. This contradicts with the desire to also measure the phenomena at longer time scales by applying the force for a longer time, because then, the decrease in $\Delta x(t)$ for longer time scales could be experimentally proven. Because the condensates fall apart, this is probably a difficult thing to achieve.

3.7 Conclusion

The conclusions which can be drawn from this experiment are not final and partially preliminary, because of the spread in the results. To draw more solid conclusions, more measurements are necessary. The first conclusion is that domain walls move in a different way than the cloud as a whole, and that it falls apart after applying the force longer. The second, and final, conclusion is that the spin drag rate for experiments below T_c can be either calculated with the assumption that either the thermal cloud or the condensate is responsible. The first assumption does not agree with theoretical predictions such as in Ref. [9], and the latter implies spin drag rates which are much higher than the ones calculated above T_c. Because not enough knowledge is available regarding the contributions of both thermal cloud and condensate, the preliminary conclusion is that the spin drag rate lies somewhere between these two extreme cases.

3.8 Outlook

From the temperature measurements which were used to check what the temperature is, it has become clear that choosing a different power of the FORT does not make much difference. The first step which can be taken is to do more measurements at *really* different temperatures. Second, it is still unclear what the contribution of both the condensate and the thermal cloud in spin drag experiments below T_c is. It is probably well worth the effort to look into this more closely, and to find out what the spin drag rate is. Third, it can also be interesting to find out ways to do experiments with other combinations of spin components. It is already possible to create mixtures of spin components in any combination in a controlled way; in this experiment only the combination spin -1 and spin 0 is used. Finally, from the analysis in this chapter it becomes clear that the behavior and dynamics of domain walls still needs to be developed in a quantitative way. The analysis provided in this chapter is a basic one (the relative distance between the two domain walls), but the way and reason domain walls grow, compress and decay is not yet accounted for in a quantitative way.

Chapter 4

Calculation of a magnetic trapping potential

4.1 Introduction

In this chapter, the magnetic field needed to create a trapping potential for atoms of a Bose-Einstein condensate is calculated. To create a Bose-Einstein condensate, the atoms must be in a vacuum chamber with a very low (order μK) temperature. Because any contact with the walls of this chamber immediately gives rise to an increase in temperature, the atoms should not be in contact with the walls of the chamber, because in that case the cloud of cold atoms is lost. By using a proper magnetic field configuration, the atoms can also be used for a wide variety of experiments. There are several ways to calculate the magnetic field of this configuration. It is possible to make use of formulas which use a calculation involving power series (see for instance Ref. [10]), but in this chapter the magnetic field is calculated using analytical formulas. After that, all ingredients are taken together in a simulation of the magnetic trap which is used in the experiment. The results of the simulation are also compared with measurements of the magnetic trap.

4.2 Layout of the coils

In order to achieve an approximately harmonic magnetic trap, one needs several different magnetic fields superposed on each other. The magnetic fields are induced by currents through various coils, which are called bias coils, pinch coils, fine tuning coils and cloverleaf (or gradient) coils. In the drag experiment, there are also MOT coils, but these are not used to trap the atoms, so they are not further incorporated here. All the coils which are mentioned above, except the fine tuning coils, consist of wires with a square cross-section which have dimensions of 3.6x3.6 mm. They also have a small channel in the middle through which the wires can be cooled. This is necessary because of the large currents passing through these wires. The fine tuning coils consist of wire with dimensions 1 mm x 3 mm and do not have to be cooled. For the calculations, all these wires are approximated as infinitely thin wires, positioned at the center of each wire. The geometry of the coils is the same for both $z > 0$ and for $z < 0$, but the directions of the currents through these wires are not. For a more detailed view of the geometry, see Figure 4.1. More details about the separate elements of the geometry will be provided in Section 4.4.

4.3 Theoretical description

As shown in Figure 4.1, there are several different segments in the layout of the coils which contribute to the total magnetic field of the trap. These are:

- Circular current loops (in the bias coils, pinch coils and fine tuning coils)

- Circular current arcs (in the cloverleaf coils)
- Finite straight lines (also in the cloverleaf coils)

Because it is, in general, not trivial to find the magnitude of the magnetic field of either one of these configurations anywhere in space (not just on the symmetry axis), the magnetic fields due to these configurations will be derived in this Section.

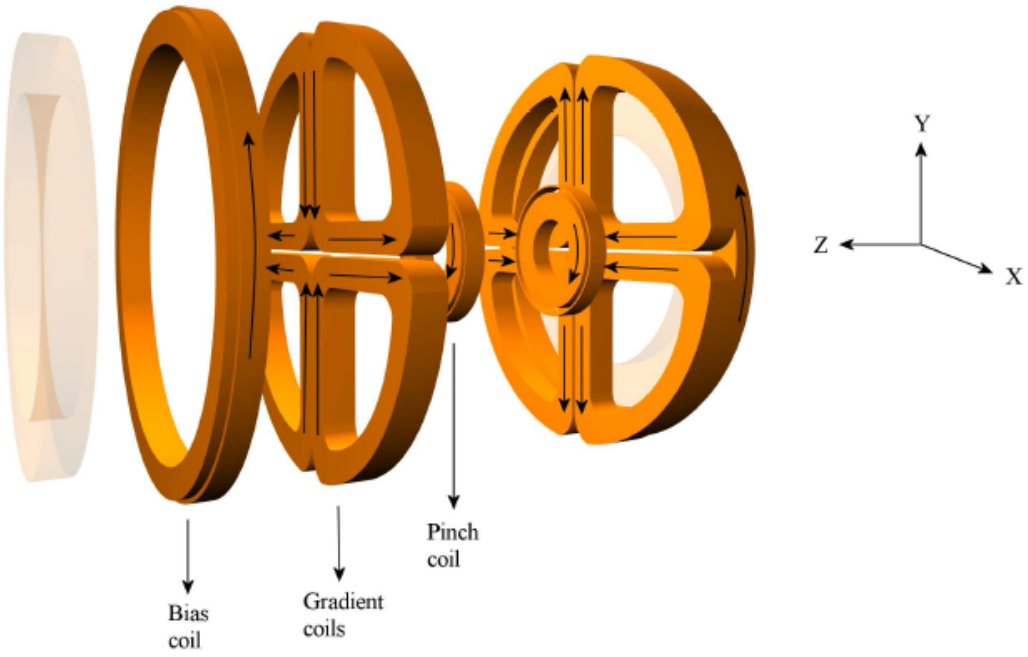

Figure 4.1: The geometry of the magnetic coil configuration (for $z > 0$). For $z < 0$, the geometry is comparable, except the direction of the current through the gradient coils (for details about this, see Section 4.4.3) [11].

4.3.1 Circular current loops

The magnetic field of a circular current loop can be found in various books (for instance Ref. [12]) but for the sake of the derivation of the circular current arcs (see Section 4.3.2) the derivation is also given here. The starting point is the magnetic vector potential, given by the following closed path integral:

$$\vec{A} = \frac{\mu_0 I}{4\pi} \oint \frac{d\vec{l}}{\mathscr{r}}. \tag{4.1}$$

Here, μ_0 is the permeability of the vacuum (see Appendix A), I is the current through the wire, $d\vec{l}$ is a vector indicating an infinitesimal part of the wire and $\mathscr{r}$ is the length of a vector pointing from the wire to the point of interest P. The magnetic vector potential only has components along the direction in which the current flows. In the case of a circular current loop, there is only a ϕ-component. So the vector $d\vec{l}$ only has one component which is equal to $dl_\phi = R\cos(\phi)d\phi$ and due to symmetry, Eq. (4.1) can also be written as:

$$A_\phi = \frac{\mu_0 I}{2\pi} \int_0^\pi \frac{R\cos(\phi)d\phi}{\mathscr{r}}. \tag{4.2}$$

The geometry of the situation is sketched in Figure 4.2.

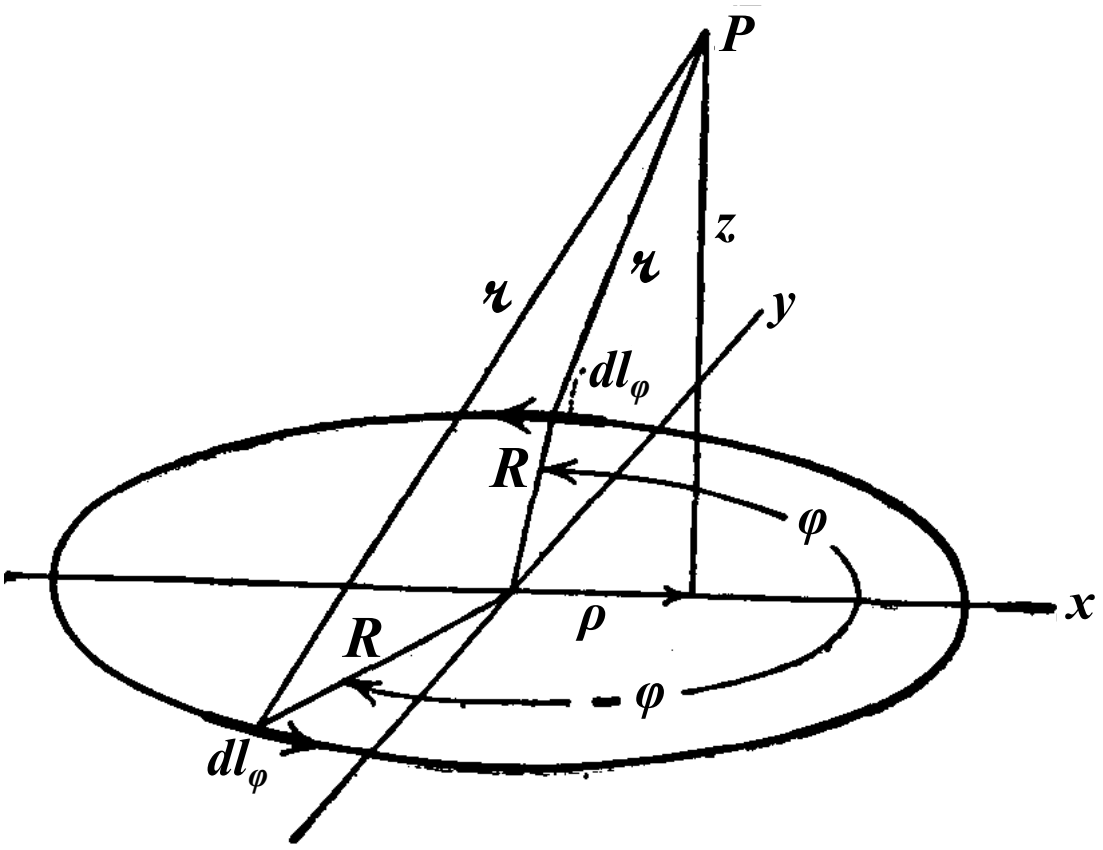

Figure 4.2: The geometry of the circular current loop. The image is a modified version of Figure 7.10 in Ref. [12].

The magnitude of r in cylindrical coordinates is given by:

$$r = \sqrt{(R - \rho\cos(\phi))^2 + (\rho\sin(\phi))^2 + (z - z_\mathrm{d})^2} = \sqrt{R^2 + \rho^2 + (z - z_\mathrm{d})^2 - 2R\rho\cos(\phi)} \quad (4.3)$$

where z_d is the z-coordinate at which the loop is located. The magnetic vector potential is thus given by:

$$A_\phi = \frac{\mu_0 I}{2\pi}\int_0^\pi \frac{R\cos(\phi)d\phi}{\sqrt{R^2 + \rho^2 + (z - z_\mathrm{d})^2 - 2R\rho\cos(\phi)}}. \quad (4.4)$$

Now, the substitution $\phi = \pi + 2\theta$ (and hence $d\phi = 2d\theta$) is made. Then $\cos(\phi)$ becomes $\cos(\phi) = \cos(\pi + 2\theta) = 2\sin^2(\theta) - 1$. The denominator r now becomes:

$$r = \sqrt{(R + \rho)^2 + (z - z_\mathrm{d})^2 - 4R\rho\sin^2(\theta)}. \quad (4.5)$$

This yields the following magnetic vector potential:

$$A_\phi = \frac{\mu_0 I R}{\pi}\int_0^{\pi/2} \frac{(2\sin^2(\theta) - 1)d\theta}{\sqrt{(R + \rho)^2 + (z - z_\mathrm{d})^2 - 4R\rho\sin^2(\theta)}}. \quad (4.6)$$

The goal of this substitution is to express the above expression in terms of elliptic integrals, which can be evaluated relatively easy. The next important substitution is:

$$k^2 = \frac{4R\rho}{(R + \rho)^2 + (z - z_\mathrm{d})^2} \quad (4.7)$$

which leads to:

$$A_\phi = \frac{\mu_0 I R}{\pi}\int_0^{\pi/2}\frac{(2\sin^2(\theta)-1)d\theta}{\sqrt{\frac{4R\rho}{k^2}(1-k^2\sin^2(\theta))}} = \frac{\mu_0 I k}{2\pi}\sqrt{\frac{R}{\rho}}\int_0^{\pi/2}\frac{(2\sin^2(\theta)-1)d\theta}{\sqrt{1-k^2\sin^2(\theta)}}. \tag{4.8}$$

This expression can be separated into two parts, namely:

$$A_\phi = \frac{\mu_0 I k}{2\pi}\sqrt{\frac{R}{\rho}}\left(\int_0^{\pi/2}\frac{2\sin^2(\theta)d\theta}{\sqrt{1-k^2\sin^2(\theta)}} - \int_0^{\pi/2}\frac{d\theta}{\sqrt{1-k^2\sin^2(\theta)}}\right). \tag{4.9}$$

The last integral in the expression above is a way to express the **complete elliptic integral of the first kind** $K(k^2)$. The first integral can be rewritten as:

$$\begin{aligned}\int_0^{\pi/2}\frac{2\sin^2(\theta)d\theta}{\sqrt{1-k^2\sin^2(\theta)}} &= \frac{2}{k^2}\int_0^{\pi/2}\frac{k^2\sin^2(\theta)d\theta}{\sqrt{1-k^2\sin^2(\theta)}} \\ &= \frac{2}{k^2}\left(\int_0^{\pi/2}\frac{d\theta}{\sqrt{1-k^2\sin^2(\theta)}} - \int_0^{\pi/2}\frac{(1-k^2\sin^2(\theta))d\theta}{\sqrt{1-k^2\sin^2(\theta)}}\right) \qquad (4.10)\\ &= \frac{2}{k^2}\left(\int_0^{\pi/2}\frac{d\theta}{\sqrt{1-k^2\sin^2(\theta)}} - \int_0^{\pi/2}\sqrt{1-k^2\sin^2(\theta)}d\theta\right). \qquad (4.11)\end{aligned}$$

In this expression, the first integral is again the complete elliptic integral of the first kind $K(k^2)$ and the second integral is a representation of the **complete integral of the second kind** $E(k^2)$. For more information about elliptic integrals, see Appendix C. This yields the result for an analytic expression for the magnetic vector potential of a circular current loop:

$$A_\phi = \frac{\mu_0 I k}{2\pi}\sqrt{\frac{R}{\rho}}\left[\left(\frac{2}{k^2}-1\right)K(k^2) - \frac{2}{k^2}E(k^2)\right]. \tag{4.12}$$

The magnetic field from this expression can be obtained by calculating the curl in cylindrical coordinates. The curl in cylindrical coordinates is given by [13]:

$$\vec{\nabla}\times\vec{A} = \left(\frac{1}{\rho}\frac{\partial A_z}{\partial\phi} - \frac{\partial A_\phi}{\partial z}\right)\hat{\rho} + \left(\frac{\partial A_\rho}{\partial z} - \frac{\partial A_z}{\partial\rho}\right)\hat{\phi} + \frac{1}{\rho}\left(\frac{\partial(\rho A_\phi)}{\partial\rho} - \frac{\partial A_\rho}{\partial\phi}\right)\hat{z}. \tag{4.13}$$

Because in this case, there is only a component of $\vec{A}$ in the ϕ-direction, the components of the magnetic field are given by:

$$B_\rho = -\frac{\partial A_\phi}{\partial z}, \tag{4.14}$$

$$B_\phi = 0, \tag{4.15}$$

$$B_z = \frac{1}{\rho}\frac{\partial(\rho A_\phi)}{\partial\rho}. \tag{4.16}$$

The magnetic field components are thus:

$$B_\rho = \frac{\mu_0 I(z-z_\mathrm{d})}{2\pi\rho\sqrt{(R+\rho)^2+(z-z_\mathrm{d})^2}}\left(-K(k^2) + \frac{R^2+\rho^2+(z-z_\mathrm{d})^2}{(R-\rho)^2+(z-z_\mathrm{d})^2}E(k^2)\right), \tag{4.17}$$

$$B_\phi = 0, \tag{4.18}$$

$$B_z = \frac{\mu_0 I}{2\pi\sqrt{(R+\rho)^2+(z-z_\mathrm{d})^2}}\left(K(k^2) + \frac{R^2-\rho^2-(z-z_\mathrm{d})^2}{(R-\rho)^2+(z-z_\mathrm{d})^2}E(k^2)\right). \tag{4.19}$$

These expressions are exactly the same as in Refs. [12] and [14].

4.3.2 Circular current arcs

A circular current arc is defined as a circular current loop only between a lower limit θ_1 and an upper limit θ_2. In the limit when $\theta_1 \to 0$ and $\theta_2 \to 2\pi$, the expressions for the full circular arc should be obtained again. The magnetic field of a circular current arc can also be calculated using the magnetic vector potential, Eq. (4.1). However, it is a more general approach compared to the derivation of a circular current loop. This time, it is more convenient to start with Cartesian coordinates and transform into cylindrical coordinates afterwards. The coordinate system can be seen in Figure 4.3.

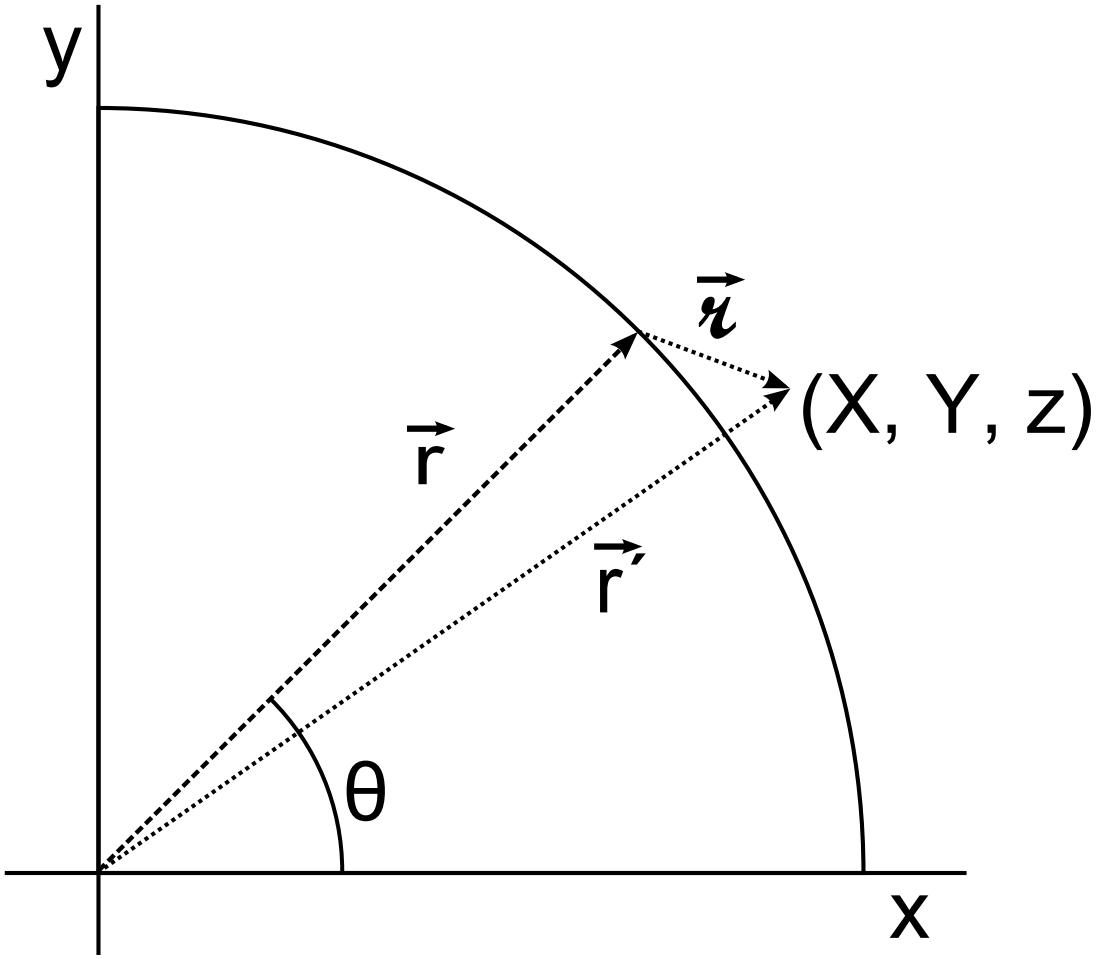

Figure 4.3: The coordinate system used in the derivation in Section 4.3.2. The arc is located at $z = z_{\mathrm{d}}$.

In Cartesian coordinates, the vector $d\vec{l}$ (indicating in which direction the current flows) is given by:

$$d\vec{l} = \begin{pmatrix} -dy \\ dx \\ 0 \end{pmatrix}. \tag{4.20}$$

If the arc has radius R, then this can be converted into cylindrical coordinates as follows:

$$d\vec{l} = \begin{pmatrix} -R\sin\theta \\ R\cos\theta \\ 0 \end{pmatrix} d\theta. \tag{4.21}$$

Any point on the arc can then be expressed as $\vec{r} = (R\cos\theta, R\sin\theta, z_\mathrm{d})$. If the point, where one wants to calculate the magnetic field is given by $\vec{r'} = (X, Y, z)$ then the magnitude of $\vec{\varkappa} = \vec{r'} - \vec{r}$ is given by:

$$\vec{\varkappa} = \begin{pmatrix} X - R\cos\theta \\ Y - R\sin\theta \\ z - z_\mathrm{d} \end{pmatrix}. \tag{4.22}$$

The length of $\vec{\varkappa}$ is equal to:

$$|\vec{\varkappa}| = \sqrt{X^2 + Y^2 + R^2 - 2R(X\cos\theta + Y\sin\theta) + (z - z_\mathrm{d})^2}. \tag{4.23}$$

Inserting Eqs. (4.21) and (4.23) into Eq. (4.1) yields:

$$\vec{A} = \frac{\mu_0 IR}{4\pi}\int_{\theta_1}^{\theta_2} \frac{-\sin(\theta)\hat{x} + \cos(\theta)\hat{y}}{\sqrt{X^2 + Y^2 + R^2 - 2R(X\cos\theta + Y\sin\theta) + (z - z_\mathrm{d})^2}} d\theta. \tag{4.24}$$

To convert this to cylindrical coordinates, the substitutions $\hat{x} = \cos(\phi)\hat{\rho} - \sin(\phi)\hat{\phi}$, $\hat{y} = \sin(\phi)\hat{\rho} + \cos(\phi)\hat{\phi}$, $X = \rho\cos(\phi)$ and $Y = \rho\sin(\phi)$ are made. Because $\vec{dl}$ has no $z-$component, $\vec{A}$ also has no $z-$component. Inserting these substitutions in Eq. (4.24) and using geometrical relations, we get:

$$\vec{A} = \frac{\mu_0 IR}{4\pi}\int_{\theta_1}^{\theta_2} \frac{\cos(\theta - \phi)\hat{\phi} - \sin(\theta - \phi)\hat{\rho}}{\sqrt{\rho^2 + R^2 - 2R\rho\cos(\theta - \phi) + (z - z_\mathrm{d})^2}} d\theta. \tag{4.25}$$

In order to obtain the $\rho-$ and $\phi-$components, we substitute $\alpha = \theta - \phi$ so we get:

$$A_\phi = \frac{\mu_0 IR}{4\pi}\int_{\theta_1-\phi}^{\theta_2-\phi} \frac{\cos(\alpha)}{\sqrt{\rho^2 + R^2 - 2R\rho\cos(\alpha) + (z - z_\mathrm{d})^2}} d\alpha, \tag{4.26}$$

$$A_\rho = -\frac{\mu_0 IR}{4\pi}\int_{\theta_1-\phi}^{\theta_2-\phi} \frac{\sin(\alpha)}{\sqrt{\rho^2 + R^2 - 2R\rho\cos(\alpha) + (z - z_\mathrm{d})^2}} d\alpha. \tag{4.27}$$

In the following sections, the $\phi-$ and $\rho-$components will be further derived, in order to arrive at expressions which can be evaluated.

The ϕ-component

The first substitution which will be incorporated is $\alpha = 2\theta' + \pi$ (the same as in Section 4.3.1), in order to change the variable of integration to θ'. This also implies that $d\alpha = 2d\theta'$ and $\theta' = \frac{\alpha - \pi}{2}$. By doing this substitution, the integration limits also change: $\theta_i - \phi = 2\theta'_i + \pi$. Solving for θ'_i then yields $\theta'_i = \frac{\theta_i - \phi - \pi}{2}$ for $i = 1, 2$ and we set $\cos(\alpha) = 2\sin^2(\theta') - 1$. Inserting all these substitutions into Eq. (4.26), the $\phi-$component becomes:

$$A_\phi = \frac{\mu_0 IR}{2\pi}\int_{\theta'_1}^{\theta'_2} \frac{2\sin^2(\theta') - 1}{\sqrt{(R + \rho)^2 - 4R\rho\sin(\theta') + (z - z_\mathrm{d})^2}} d\theta'. \tag{4.28}$$

Using eq. (4.7), this expression can be rewritten as:

$$A_\phi = \frac{\mu_0 Ik}{4\pi}\sqrt{\frac{R}{\rho}}\int_{\theta'_1}^{\theta'_2} \frac{2\sin^2(\theta') - 1}{\sqrt{1 - k^2\sin^2(\theta')}} d\theta', \tag{4.29}$$

$$= \frac{\mu_0 Ik}{4\pi}\frac{R}{\rho}\left((\frac{2}{k^2} - 1)\int_{\theta'_1}^{\theta'_2} \frac{d\theta'}{\sqrt{1 - k^2\sin^2(\theta')}} - \frac{2}{k^2}\int_{\theta'_1}^{\theta'_2} \sqrt{1 - k^2\sin^2(\theta')} d\theta' \right). \tag{4.30}$$

The first of these integrals is the ***incomplete*** **elliptic integral of the first kind** $F(\gamma_i|k^2)$ and the second integral is the ***incomplete*** **elliptic integral of the second kind** $E(\gamma_i|k^2)$ where

γ_i are the upper and lower limits of the integral (see also Appendix C). Because elliptic integrals normally have a lower limit equal to zero, these two integrals can each be denoted by the difference between two incomplete elliptic integrals. For the $\phi-$component, this finally yields:

$$A_\phi = \frac{\mu_0 I k}{4\pi}\sqrt{\frac{R}{\rho}}\left[(\frac{2}{k^2}-1)\left(F(\theta_2'|k^2)-F(\theta_1'|k^2)\right)-\frac{2}{k^2}\left(E(\theta_2'|k^2)-E(\theta_1'|k^2)\right)\right]. \tag{4.31}$$

If θ_2' is set to 2π and θ_1' is set to 0, then for any ϕ, $F(\theta_2'|k^2)-F(\theta_1'|k^2)=2K(k^2)$ and $E(\theta_2'|k^2)-E(\theta_1'|k^2)=2E(k^2)$. Inserting this into Eq. (4.31) yields Eq. (4.12), as expected.

The ρ-component

In order to obtain the $\rho-$component, we make the same substitutions as for the $\phi-$component, so the integration variable, integration limits and denominator change in the same way. The sine in the numerator also changes: $\sin(\alpha)=\sin(2\theta'+\pi)=-\sin(2\theta')$. Inserting this into Eq. (4.27) yields:

$$A_\rho = \frac{\mu_0 I R}{4\pi}\int_{\theta_1'}^{\theta_2'}\frac{\sin(2\theta')}{\sqrt{(R+\rho)^2-4R\rho\sin^2(\theta')+(z-z_\mathrm{d})^2}}d\theta'. \tag{4.32}$$

Using Eq. (4.7) gives, after rewriting:

$$A_\rho = \frac{\mu_0 I k}{4\pi}\sqrt{\frac{R}{\rho}}\int_{\theta_1'}^{\theta_2'}\frac{\sin(2\theta')}{\sqrt{1-k^2\sin^2(\theta')}}d\theta'. \tag{4.33}$$

The integral in Eq. (4.33) can be evaluated using partial integration:

$$\int_{\theta_1'}^{\theta_2'}\frac{\sin(2\theta')}{\sqrt{1-k^2\sin^2(\theta')}}d\theta' = \left[\sin(2\theta')F(\theta'|k^2)\right]_{\theta_1'}^{\theta_2'} - 2\int_{\theta_1'}^{\theta_2'}\frac{\cos(2\theta')}{\sqrt{1-k^2\sin^2(\theta')}}d\theta' \tag{4.34}$$

which can be evaluated in terms of analytical functions and incomplete elliptic integrals of the first kind. The $\rho-$component then becomes (after inserting the expressions for θ_1' and θ_2'):

$$A_\rho = \frac{\mu_0 I k}{4\pi}\sqrt{\frac{R}{\rho}}\frac{\sqrt{2}\left(k^2\cos(\theta_2-\phi)f(\theta_1,k)-k^2\cos(\theta_1-\phi)f(\theta_2,k)-(k^2-2)g(\theta_1,\theta_2,k)\right)}{f(\theta_1,k)f(\theta_2,k)} \tag{4.35}$$

where (for $i=1,2$)

$$f(\theta_i,k)=\sqrt{k^2(-\cos(\theta_i-\phi))-k^2+2} \tag{4.36}$$

and

$$g(\theta_1,\theta_2,k)=f(\theta_1,k)\left(\sqrt{\frac{k^2\cos(\theta_2-\phi)}{k^2-2}+1}-1\right)+f(\theta_2,k)\left(1+\sqrt{\frac{k^2\cos(\theta_1-\phi)}{k^2-2}+1}\right). \tag{4.37}$$

It is more convenient to *not* insert the expressions for θ_1' and θ_2'. In that case, A_ρ reduces to:

$$A_\rho = \frac{\mu_0 I}{4\pi}\sqrt{(R+\rho)^2+(z-z_\mathrm{d})^2}\left[h(\theta_1')-h(\theta_2')\right] \tag{4.38}$$

where (for $i=1,2$):

$$h(\theta_i')=\sqrt{\frac{R^2+\rho^2+2R\rho\cos(2\theta_i')+(z-z_\mathrm{d})^2}{(R+\rho)^2+(z-z_\mathrm{d})^2}}. \tag{4.39}$$

To obtain the magnetic field, the curl of Eqs. (4.31) and (4.35) (or 4.38) is taken using Eq. (4.13). The expressions for the magnetic field are quite lengthy, so they are included in Appendix D.

4.3.3 Finite straight wire

The expression for the magnetic field of a finite, straight wire can be found in many textbooks, like [13] and is equal to:

$$\vec{B} = \frac{\mu_0 I}{4\pi s}(\sin(\theta_2) - \sin(\theta_1))\hat{\phi} \tag{4.40}$$

where the angles are taken with respect to the origin. The current flows from θ_1 to θ_2 and s is the (shortest) distance from the wire to the point where the magnetic field is evaluated. In the following, a Cartesian coordinate system will be assumed; the current flows in the $\hat{x}-$direction through a wire located at $y = y_d, z = z_\mathrm{d}$ (if these are zero, then the wire is at the $x-$axis). With these assumptions, $s = \sqrt{(y-y_d)^2 + (z-z_\mathrm{d})^2}$. The sines can be written as:

$$\sin(\theta_i) = \frac{x_i - x}{\sqrt{(x_i - x)^2 + (y-y_d)^2 + (z-z_\mathrm{d})^2}} \tag{4.41}$$

for $i = 1, 2$. The direction of the magnetic field $\hat{\phi}$ can be expressed as the (normalized) cross product of the current $\vec{I}$ and the vector $\vec{s}$, which is in this case equal to $\vec{s} = \begin{pmatrix} 0 \\ y-y_d \\ z-z_\mathrm{d} \end{pmatrix}$. This yields:

$$\hat{\phi} = \frac{\vec{I}\times\vec{s}}{|\vec{I}\times\vec{s}|} = \frac{1}{|\vec{I}\times\vec{s}|}\begin{pmatrix}1\\0\\0\end{pmatrix} \times \begin{pmatrix} 0 \\ y-y_d \\ z-z_\mathrm{d} \end{pmatrix} = \frac{1}{\sqrt{(y-y_d)^2 + (z-z_\mathrm{d})^2}} \begin{pmatrix} 0 \\ z_\mathrm{d}-z \\ y-y_d \end{pmatrix}. \tag{4.42}$$

The magnetic field of this finite straight wire is thus given by:

$$\vec{B}(x,y,z) = \frac{\mu_0 I}{4\pi\left((y-y_d)^2 + (z-z_\mathrm{d})^2\right)} \cdot \left(\frac{x_2 - x}{\sqrt{(x_2-x)^2 + (y-y_d)^2 + (z-z_\mathrm{d})^2}} - \frac{x_1 - x}{\sqrt{(x_1-x)^2 + (y-y_d)^2 + (z-z_\mathrm{d})^2}} \right) \begin{pmatrix} 0 \\ z_\mathrm{d}-z \\ y-y_d \end{pmatrix}. \tag{4.43}$$

For a wire parallel to the $y-$ or $z-$axis, a similar derivation can be done.

4.4 Characteristics of the components

In this Section, the characteristics of the various coils, needed to make a magnetic trap, will be discussed. As pointed out in the previous sections, the most suitable set of coordinates is a cylindrical coordinate system. In the lab, a *positive z-axis* points in the direction of the windows of the lab. The $\rho-$plane is perpendicular to this axis. In Figure 4.4, the configuration is described in detail, to support the descriptions of the various components outlined below.

4.4.1 The pinch and bias coils

The first two components which are discussed, are the pinch coils and bias coils. The reason that they are discussed in one subsection, is that they are connected in series. For both positive and negative z, the current in the pinch flows clockwise and the current in the bias flows counterclockwise. The pinch coil consists of a total of 12 wires (on both sides of the vacuum chamber), in a configuration of 4 windings and 3 layers. The windings are located between $R_\mathrm{min} = 16 \times 10^{-3}$ m and $R_\mathrm{max} = 31.75 \times 10^{-3}$ m and the layers are located between $z_\mathrm{min} = \pm 30 \times 10^{-3}$ m and $z_\mathrm{max} = \pm 41.5 \times 10^{-3}$ m. The bias coil consists of a total of 15 wires, in a configuration of 4 windings and 4 layers. The windings are located between $R_\mathrm{min} = 79.5 \times 10^{-3}$ m and $R_\mathrm{max} = 95 \times 10^{-3}$ m, the layers are located between $z_\mathrm{min} = \pm 62 \times 10^{-3}$ m and $z_\mathrm{max} = \pm 77.5 \times 10^{-3}$ m. In the bias coil, the outermost wire (with respect to both R and z) is missing. In the experiment, the current which flows through these two coils ranges between 1.6 and 200 A.

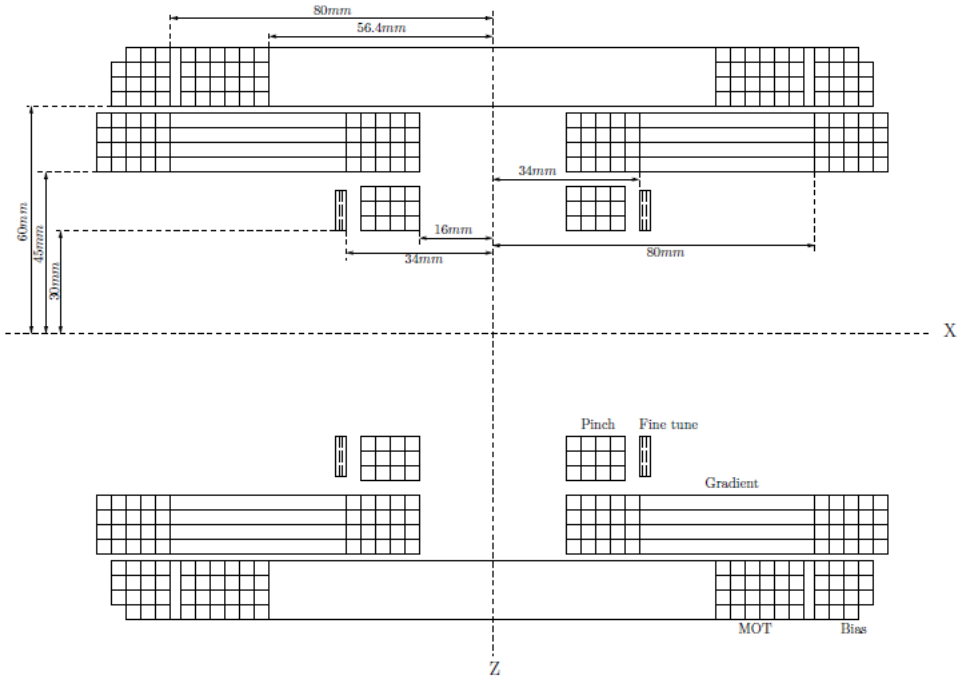

Figure 4.4: A sketch of the various components of the magnetic trap in the $x, z-$plane. Each little square stands for one wire. [11]

The shunt

The shunt can be used to divert current from the bias. In order to do this, it is connected in parallel with the bias, and this parallel circuit is connected in series with the pinch. The curvature of the magnetic trap can in this way be changed, as is also discussed in [11]. The maximum current which can be diverted, is 125A. In Figure 4.5, the effect of the shunt on the curvature (as calculated in the simulation) is shown for various currents through the shunt. It can be seen that both the curvature becomes smaller and the magnitude of the magnetic field at the minimum shifts upwards if the current through the shunt increases.

4.4.2 The fine tuning coils

The finetuning coil consists of 6 wires (on both sides of the vacuum chamber) in a configuration of 2 windings and 3 layers. The windings are located between $R_{\min} = 35.5 \times 10^{-3}$ m and $R_{\max} = 38 \times 10^{-3}$ m and the layers are located between $z_{\min} = \pm 30 \times 10^{-3}$ m and $z_{\max} = \pm 39.5 \times 10^{-3}$ m. It is used to optimize the axial confinement (i.e. confinement in the $z-$direction). Axial confinement is in principle obtained by the combination of both pinch and bias coils. Their magnetic fields should theoretically cancel each other at the minimum of the trap, but due to the fact that each of them consists of a discrete amount of wires (in the setup, there is no such thing as a magnetic coil consisting of 'exactly' $11\frac{1}{2}$ wires), this cannot be achieved by the pinch and bias coils alone. Also, when varying the current through the pinch and bias, the absolute value of the magnetic field at the minimum of the trap, should be kept at a given value (in the experiment, this is usually 4 Gauss, where 1 G = 10^{-4} T). The fine tuning coils are used to aid for this. In the experiment, the current which flows through the fine tuning coils ranges between 1.767 and 4.75 A. In the simulation, other values for the fine tuning have to be inserted to achieve the desired result. The reason for this is not entirely clear.

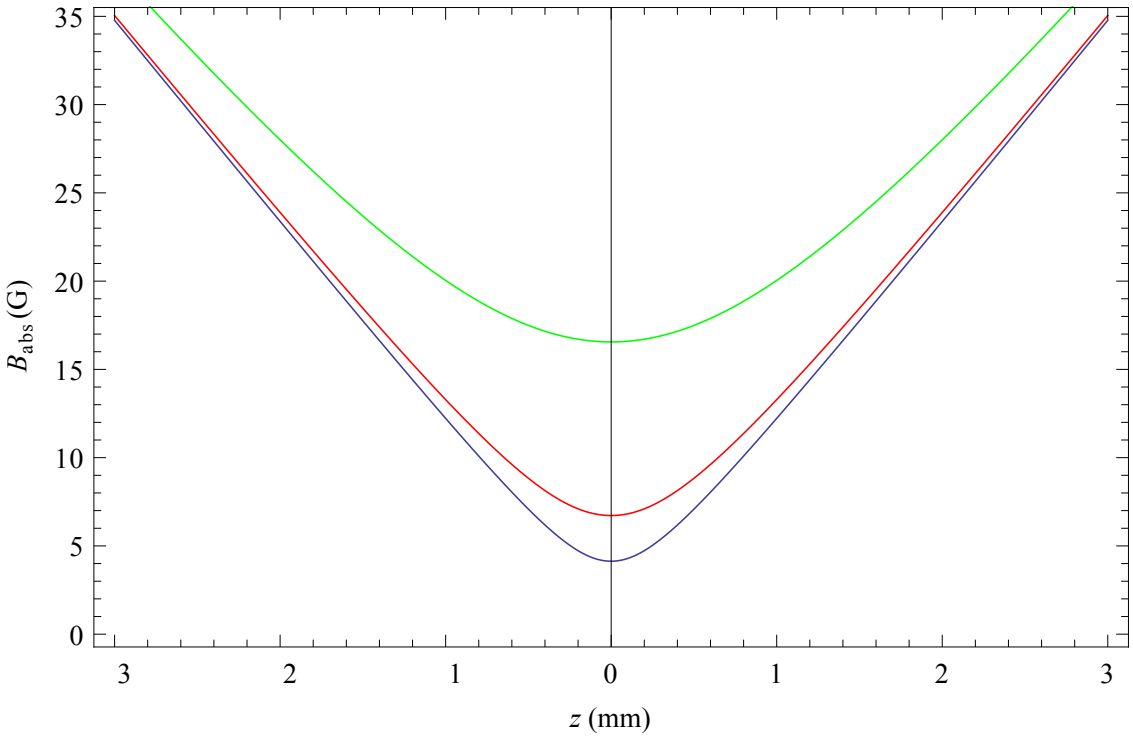

Figure 4.5: The curvature as a function of the current through the shunt. Blue is $I_s = 0$A, red is $I_s = 2.5$A and green is $I_s = 12$A. In all plots, the current through the pinch coils is 200A and the current through the cloverleaf coils is 320A.

4.4.3 The cloverleaf coils

For radial confinement (i.e. confinement in the $\rho-$direction), the cloverleaf coils are used. These coil construction consists of 8 cloverleaves, 4 at positive z and 4 at negative z. For clarity, it is convenient to describe the geometry in terms of a Cartesian coordinate system.

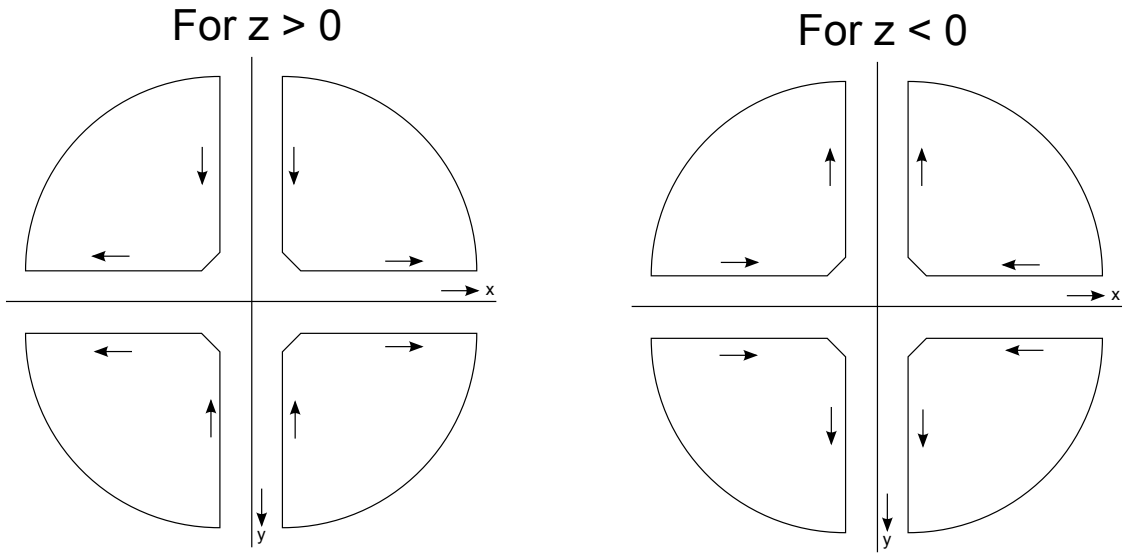

Figure 4.6: A schematic representation of the cloverleaves for both $z > 0$ (left-hand picture) and $z < 0$ (right-hand picture). The arrows indicate the direction of the current.

Each cloverleaf coil consists of one straight wire parallel to the $x-$axis, one straight wire parallel

to the $y-$axis, a circular current arc which links the two straight wires at the side far away from the $z-$axis and a piece of wire that links the two straight wires close to the $z-$axis. This 'center' piece of wire is also approximated as a straight piece of wire. The cloverleaf coils consist of 20 wires each, with a configuration of 5 windings and 4 layers. These layers are located between $z_{\min} = \pm 45 \times 10^{-3}$ m and $z_{\max} = \pm 60.5 \times 10^{-3}$ m, the windings have an inner radius of 16×10^{-3} m and an outer radius of 11.3×10^{-2} m. The direction of the current through the cloverleaf coils is different for both $z > 0$ and $z < 0$. For a schematic representation of the direction of the currents, see Figure 4.6. The current through the cloverleaf coils is normally 320 A, but lower values are also possible. Due to these high currents, 5 power supplies are necessary (1 connected in series with a parallel circuit of 4 others).

4.5 Trap frequencies

Each magnetic trap can be characterized by certain properties. One of them is the magnitude of the field at the minimum of the trap. In the experiment, the minimum is generally kept at 4 Gauss. The magnetic trap has a shape as shown in Figure 4.7.

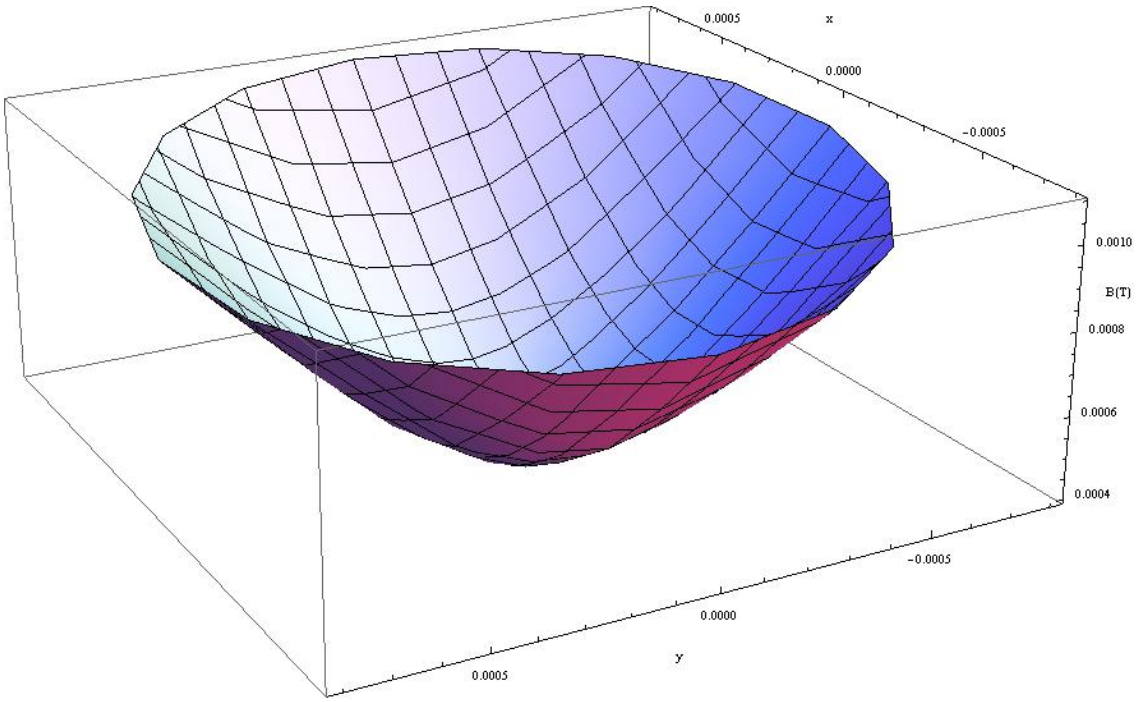

Figure 4.7: The magnetic trap created by only pinch, bias, fine tuning and cloverleaf coils.

The most important properties are the trap frequencies. There are two distinct trap frequencies: the axial and radial trap frequency. The trap frequency is a measure for the curvature of the magnetic field. The magnetic field components are:

$$B_\rho(\rho,\phi,z) = B_{\rho,\text{pinch}}(\rho,z) + B_{\rho,\text{bias}}(\rho,z) + B_{\rho,\text{fine tuning}}(\rho,z) + B_{\rho,\text{cloverleaf}}(\rho,\phi,z), \tag{4.44}$$

$$B_\phi(\rho,\phi,z) = B_{\phi,\text{cloverleaf}}(\rho,\phi,z), \tag{4.45}$$

$$B_z(\rho,\phi,z) = B_{z,\text{pinch}}(\rho,z) + B_{z,\text{bias}}(\rho,z) + B_{z,\text{fine tuning}}(\rho,z) + B_{z,\text{cloverleaf}}(\rho,\phi,z). \tag{4.46}$$

To calculate the trap frequencies, the Zeeman energy and the energy of the harmonic potential are used. For the axial trap frequency, the following relations are used:

$$\Delta E = \mu_B g_F m_F (B_{\text{abs}}(\rho,\phi,z) - B_0), \tag{4.47}$$

$$\Delta E = \frac{1}{2} m\omega^2 z^2. \tag{4.48}$$

Here, $B_{\text{abs}}(\rho,\phi,z) = \sqrt{B_\rho(\rho,\phi,z)^2 + B_\phi(\rho,\phi,z)^2 + B_z(\rho,\phi,z)^2}$ and the hyperfine Landé g-factor can be calculated from (see Ref. [3]):

$$g_F = g_J \frac{F(F+1) - I(I+1) + J(J+1)}{2F(F+1)} + g_I \frac{F(F+1) + I(I+1) - J(J+1)}{2F(F+1)} \tag{4.49}$$

where F is the magnitude of the total angular momentum of the atom, which is equal to $\vec{F} = \vec{J} + \vec{I}$, with J the (magnitude of the) total electron angular momentum and I the (magnitude of the) total nuclear angular momentum. The total electron angular momentum is equal to $\vec{J} = \vec{L} + \vec{S}$ with L the orbital angular momentum and S the spin angular momentum. In this case, $F = 1$ and $J = \frac{1}{2}$ and $I = \frac{3}{2}$ (this makes sense, because both J and I are vectors). The remaining constants are given in Appendix A. Taking the second derivative of Eqs. (4.47) and (4.48) with respect to z yields:

$$\mu_B g_F m_F \frac{\partial^2 B_{\text{abs}}(\rho,\phi,z)}{\partial z^2} = m\omega^2. \tag{4.50}$$

The axial trap frequency is then:

$$f_z = \frac{1}{2\pi}\sqrt{\frac{\mu_B g_F m_F \frac{\partial^2 B_z(\rho,\phi,z)}{\partial z^2}}{m}}. \tag{4.51}$$

The radial trap frequency can be calculated in an analogous manner. The only difference is that one does not take the second derivative of B_{abs} with respect to z, but with respect to ρ:

$$f_\rho = \frac{1}{2\pi}\sqrt{\frac{\mu_B g_F m_F \frac{\partial^2 B_{\text{abs}}(\rho,\phi,z)}{\partial \rho^2}}{m}}. \tag{4.52}$$

Both trap frequencies must be evaluated at the point where the magnetic field of the trap has its minimum value (i.e. $\rho = \rho_{\min}, \phi = \phi_{\min}, z = z_{\min}$).

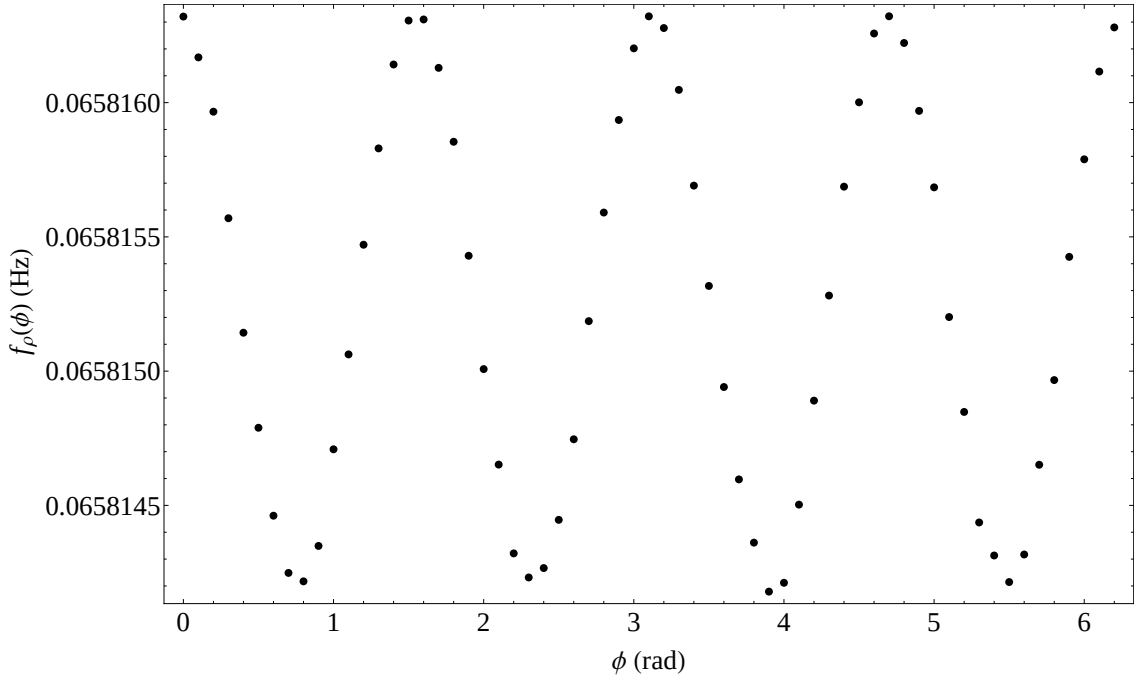

Figure 4.8: The radial trap frequency as a function of the angle ϕ. To calculate these points, the current through the cloverleaf coils is 320A, the current through pinch and bias coils is 200A and the value of the magnetic field at the minimum of the trap is at 4G. Because the variation as a function of angle is very small, a value of 100.8 Hz is subtracted from the labels on the vertical axis to make this difference visible. The radial trap frequency is thus around 100.86 Hz.

If the compensation coils (see Section 4.7) and extra gradients in the radial direction (see Section 4.8) are turned off, then $\rho_{\min} = 0$, $z_{\min} = 0$ and $\phi_{\min}$ is arbitrary (because in cylindrical coordinates, at $\rho = 0$ the angle has no meaning). The radial trap frequency has a small dependency on the angle (which accounts for a trap frequency in both the $x-$ and $y-$direction). In the experiment, the trap frequencies in the $x-$ and $y-$direction have a variation with respect to each other which is smaller than 10^{-3} Hz. Because this simulation uses cylindrical coordinates, the radial trap frequency at any angle can be calculated. Only the minimum and maximum values are interesting. This is also shown in Figure 4.8, where the radial trap frequency as a function of the angle ϕ is shown.

4.6 Comparison between the code and the experiment

With the bias, pinch, fine tuning and cloverleaf coils, a harmonic trap can be made. In this Section, the results obtained by the simulation are compared with measurements in the experiment. In the experiment, other coils are also incorporated (like compensation coils, see Section 4.7) but these are not included in the calculation outlined below. In the following, the effects of the currents on both trap frequencies are compared.

4.6.1 Cloverleaf current versus radial trap frequency

In order to change the radial trap frequency, it is necessary to adjust the current through the cloverleaf coils. The currents through these coils can range between (theoretically) 0A and 360A. For experimental purposes, the minimum current which is used is 80A. Changing the current through the cloverleaf coils does not change the magnitude of the magnetic field at the minimum of the trap, because this is mostly determined by the $z-$component of the field. In Table 4.1, a comparison between measured and calculated values of the radial trap frequency is shown.

Current cloverleaves (A)	Measured f_ρ (Hz)	Calculated f_ρ (Hz)	Difference (Hz)
320	96.4	100.8	4.4
280	86.2	88.05	1.85
240	76.3	75.3	-1
200	65.6	62.4	-3.2
160	53.98	49.5	-4.5
120	49.2	36.4	-12.8
80	28.5	22.84	-5.66

Table 4.1: A comparison between the radial trap frequencies measured in the experiment and calculated in the simulation, as a function of the current through the cloverleaf coils. The magnitude of the magnetic field at the minimum of the trap is 4G, the current through the pinch and bias coils is 200A.

4.6.2 Current through pinch and bias versus axial trap frequency

To change the axial trap frequency, one needs to adjust the current through the pinch and bias coils. However, by changing this current, the magnitude of the magnetic field at the minimum of the trap also shifts. Because this value is an important characteristic of the trap (a difference in minimum of the magnetic field automatically yields different trap frequencies), this must be corrected by using the fine tuning coils. By doing this, a fair relation between current and trap frequency can be made. In Table 4.2, a comparison between the values measured in the experiment and values calculated in the simulation is shown.

Current pinch and bias (A)	Measured f_z (Hz)	Calculated f_z (Hz)	Difference (Hz)
1.6	1.4*	1.96	0.56
3.2	1.96 ± 0.002	2.40	0.44
6.2	2.73 ± 0.001	3.06	0.33
24	5.28 ± 0.005	5.54	0.26
64	8.58 ± 0.008	8.87	0.29
200	15.5*	15.58	0.08

Table 4.2: A comparison between the axial trap frequencies measured in the experiment and calculated in the simulation, as a function of the current through the pinch and bias coils. The magnitude of the magnetic field at the minimum of the trap is 4G, the current through the cloverleaf coils is 320A. The 'measured' values marked with a * are given (known) values, which were not explicitly measured.

To measure the axial trap frequency as a function of the current through pinch and bias coils, a series of images was made where the cloud of atoms was displaced. By analyzing this series of images (the cloud of atoms moves from left to right and vice versa), the radial trap frequency can be calculated. An example of a fit is shown in Figure 4.9.

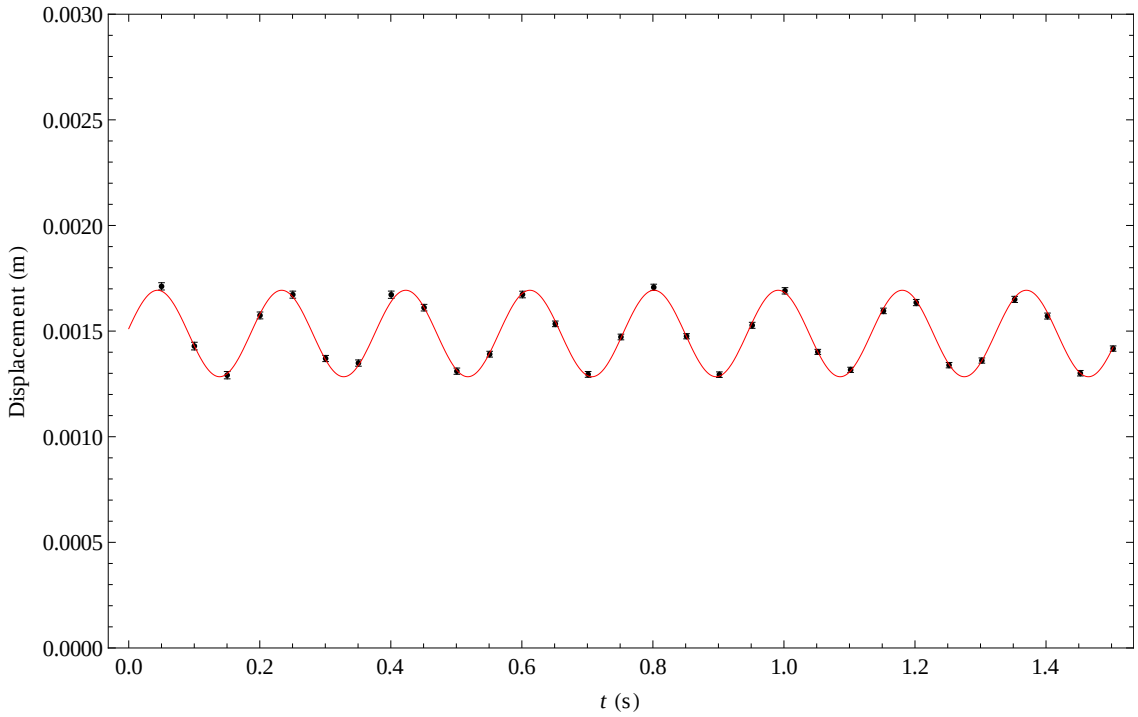

Figure 4.9: A sinusoidal fit from which the axial trap frequency can be derived. This example corresponds with a current through pinch and bias coils of 24A, which yields an axial trap frequency of 5.28 Hz. The time between each data point is in this measurement 50.08 ms.

By changing the current through pinch and bias coils, the *radial* trap frequency should not change much. This was also measured and the results are shown in Table 4.3. An example of a fit used to calculate the radial trap frequency is shown in Figure 4.10.

Current pinch and bias (A)	Measured f_ρ (Hz)
1.6	96*
3.2	95.3 ± 0.02
6.2	95.3 ± 0.05
24	96.27 ± 0.04
64	95.43 ± 0.10

Table 4.3: Measured *radial* trap frequencies as a function of the current through the pinch and bias coils. The magnitude of the magnetic field at the minimum of the trap is 4G, the current through the cloverleaf coils is 320A. The values marked with a * are given (known) values, which were not explicitly measured.

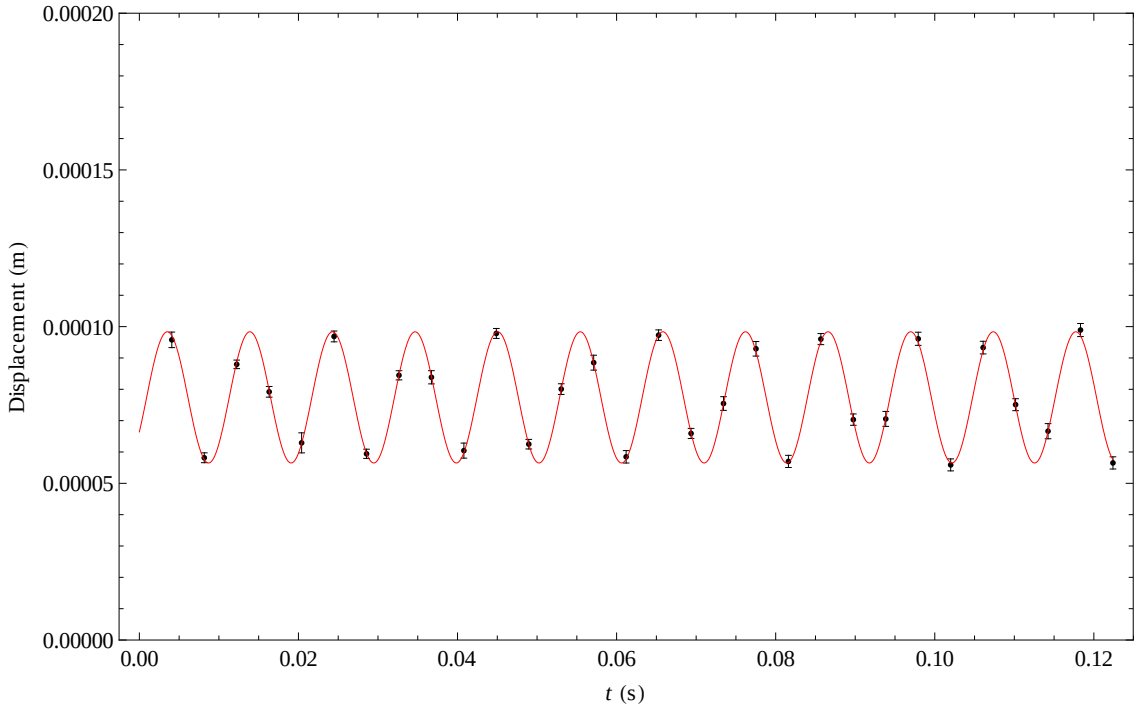

Figure 4.10: A sinusoidal fit from which the radial trap frequency can be derived. This example corresponds with a current through pinch and bias coils of 24A, which yields a radial trap frequency of 96.27 Hz. The time between each data point is in this measurement 4.08 ms.

4.7 Compensation coils

In the setup, the (small) effect of the earth magnetic field also plays a role. The magnitude of the earth magnetic field is in the order of 1 G, so this can be a significant contribution, if one keeps in mind that the magnitude of the magnetic field at the minimum of the trap is also in the order of 1 G. In order to compensate for this contribution, a set of compensation coils (cage shaped) are used. A schematic representation is shown in Figure 4.11. The compensation coils consist of 6 coils: 2 $x-$compensation coils, 2 $y-$compensation coils and 2 $z-$compensation coils. The $x-$compensation coils go around the $x-$axis (and are thus in the $y,z-$plane), there is one at $x < 0$ and one at $x > 0$. A similar reasoning holds for the $y-$ and $z-$compensation coils. The $x-$compensation coils consist of 20x4 windings, the wires have a diameter of 1.25×10^{-3} m. The $y-$compensation coils consist of 10x2 windings and the $z-$compensation coils consist of 10x4 windings. Both of these use the same type of wires with a diameter of 1.8×10^{-3} m. For the dimensions of the cage, see Figure 4.11. The currents through the compensation coils can be set separately, the usual settings are: $x-$compensation coils 0A, $y-$compensation coils 0.24A and $z-$compensation coils 0.8A.

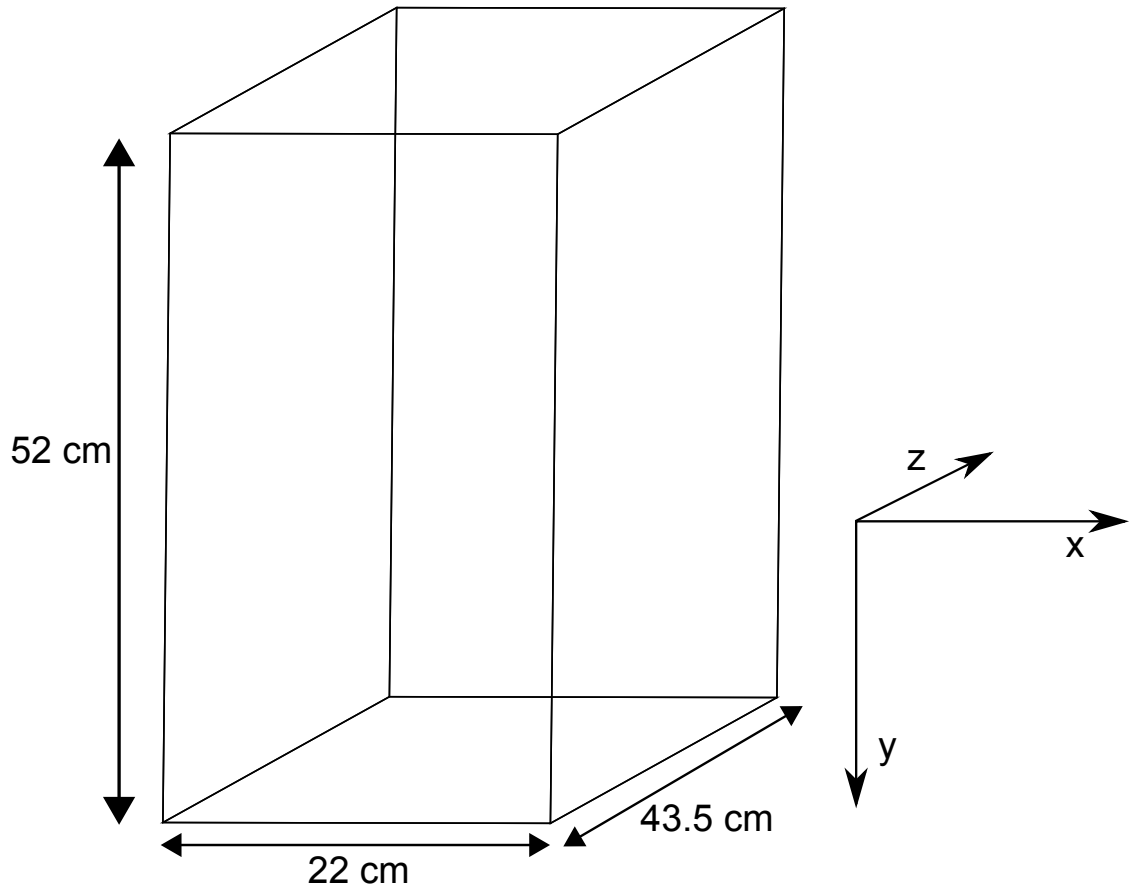

Figure 4.11: The cage shaped compensation coils. The origin is located in the middle of the cage, at the same point as the origin of the magnetic trap.

4.8 Extra added gradients

Apart from using the fine tuning coils, there are also other ways to shift the minimum of the absolute value of the magnetic field. One of them is to add gradients to the simulation. It is not (yet) clear where these gradients exactly come from in the experiment, but they are a way to adjust the magnetic trap in the situation to act the same way as in the experiment. The reason why these gradients are incorporated is that in the experiment, the magnetic trap does not behave as it should. By adding these gradient, an attempt is made to explain the anomalies in the experiment. In this Section, these gradients are discussed in more detail.

4.8.1 Gradient in the $\rho - \phi$ plane in the $\rho - \phi$ plane

The first possibility of a gradient which can be applied is a gradient in the $\rho - \phi$ plane, varying in the $\rho - \phi$ direction. In Cartesian coordinates, such a gradient is simply of the form $\vec{B}_x = (a + bx)\hat{x}$ or $\vec{B}_y = (a + by)\hat{y}$. Here, a has units T and b has units T/m. In cylindrical coordinates, the expression for $\vec{B}_x$ can be rewritten as:

$$\vec{B}_x = (a + b\rho\cos(\phi))\left(\cos(\phi)\hat{\rho} - \sin(\phi)\hat{\phi}\right). \tag{4.53}$$

So this yields the following 2 components:

$$B_\rho = a\cos(\phi) + b\rho\cos^2(\phi) \tag{4.54}$$

$$B_\phi = -a\sin(\phi) - \frac{1}{2}b\rho\sin(2\phi). \tag{4.55}$$

With the same kind of transformation, the expression for $\vec{B}_y$ can also be rewritten as:

$$\vec{B}_y = (a + b\rho\sin(\phi))\left(\sin(\phi)\hat{\rho} + \cos(\phi)\hat{\phi}\right). \tag{4.56}$$

So this yields the following 2 components:

$$B_\rho = a\sin(\phi) + b\rho\sin^2(\phi) \tag{4.57}$$

$$B_\phi = a\cos(\phi) + \frac{1}{2}b\rho\sin(2\phi). \tag{4.58}$$

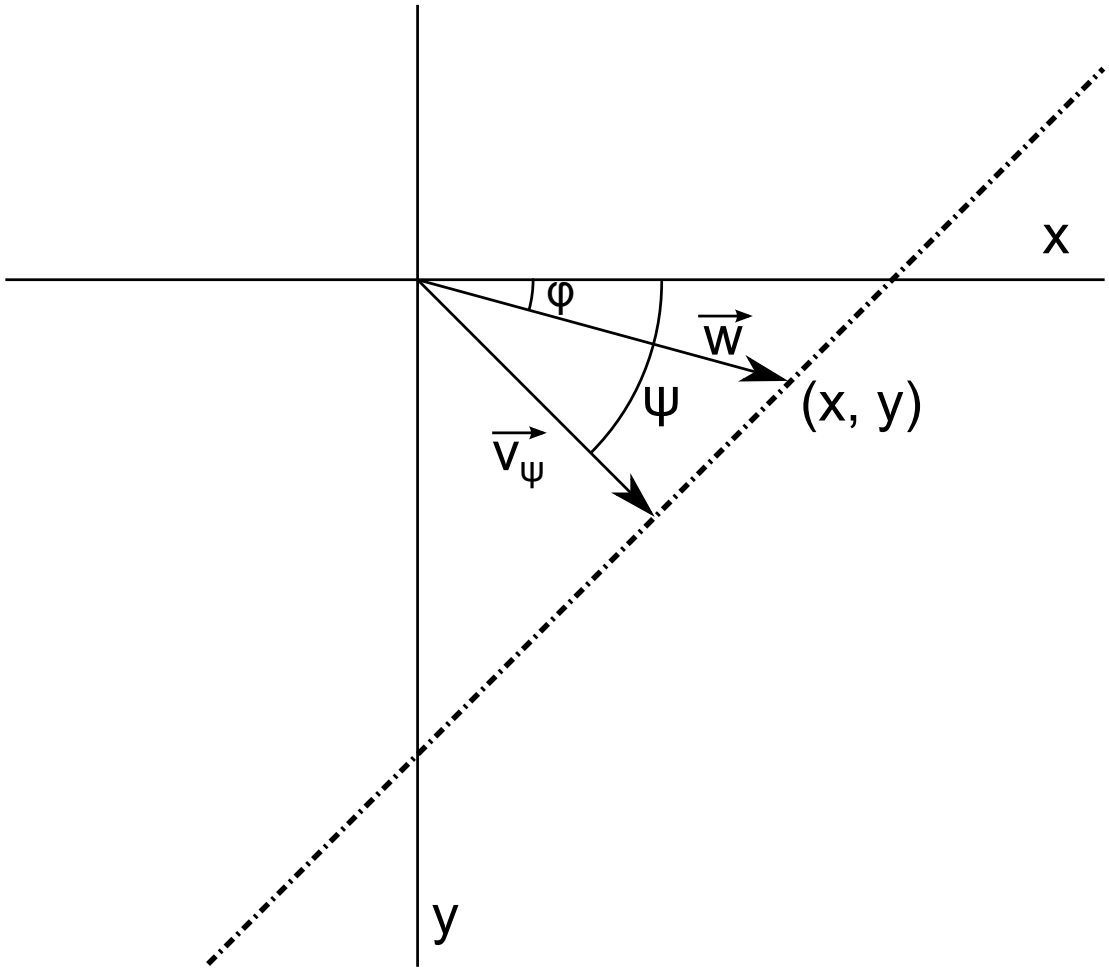

Figure 4.12: Explanation used in the derivation of the $\rho-$gradient in the $\rho - \phi$ plane (which is equivalent to the $x - y$ plane in Cartesian coordinates). The dashed line is the contour of the gradient (the angle ψ can be varied).

It is also possible to derive two general expressions (with one extra variable) which can yield both Eqs. (4.54), (4.55), (4.57) and (4.58). The variables used in this derivation are explained in Figure 4.12. The expression for a gradient of the magnetic field with an angle ψ is:

$$\vec{B}_{\mathrm{grad},\psi} = (a + bw)\hat{v}_\psi \tag{4.59}$$

where $\hat{v}_\psi = \cos(\psi)\hat{x} + \sin(\psi)\hat{y} = \cos(\psi-\phi)\hat{\rho} - \sin(\phi-\psi)\hat{\phi}$ and $w = \sqrt{x^2+y^2}\cos(\psi-\phi) = \rho\cos(\psi-\phi)$. Writing this out yields the two desired expressions:

$$B_\rho = a\cos(\psi-\phi) + b\rho\cos^2(\psi-\phi) \tag{4.60}$$

$$B_\phi = -a\sin(\phi-\psi) - \frac{1}{2}b\rho\sin(2(\phi-\psi)). \tag{4.61}$$

With these expressions, it is possible to shift the minimum of the trap to another location than $\rho = 0$. If $\psi = 0$, then Eqs. (4.54) and (4.55) are obtained again, if $\psi = \frac{\pi}{2}$ then the result yields Eqs. (4.57) and (4.58). Eqs. (4.60) and (4.61) are particularly useful if one wants to apply a magnetic field with a random angle with respect to the other components of the setup. If $a = 0$ and $b \neq 0$, then this gradient has the form of a plane with a certain slope. If this plane is (vectorially) added to the expressions for the magnetic trap (Eqs. (4.44), (4.45) and (4.46)), the magnetic trap becomes trough-shaped. If $b = 0$ but $a \neq 0$ a constant magnetic field is added to the expressions for the magnetic trap. This yields a small shift in the position of the minimum of the magnetic trap in the $\rho - \phi$ plane. This is illustrated in Figure 4.13. The minimum can be calculated using the Gradient Descent method (this only works if the minimum is at nonzero ρ).

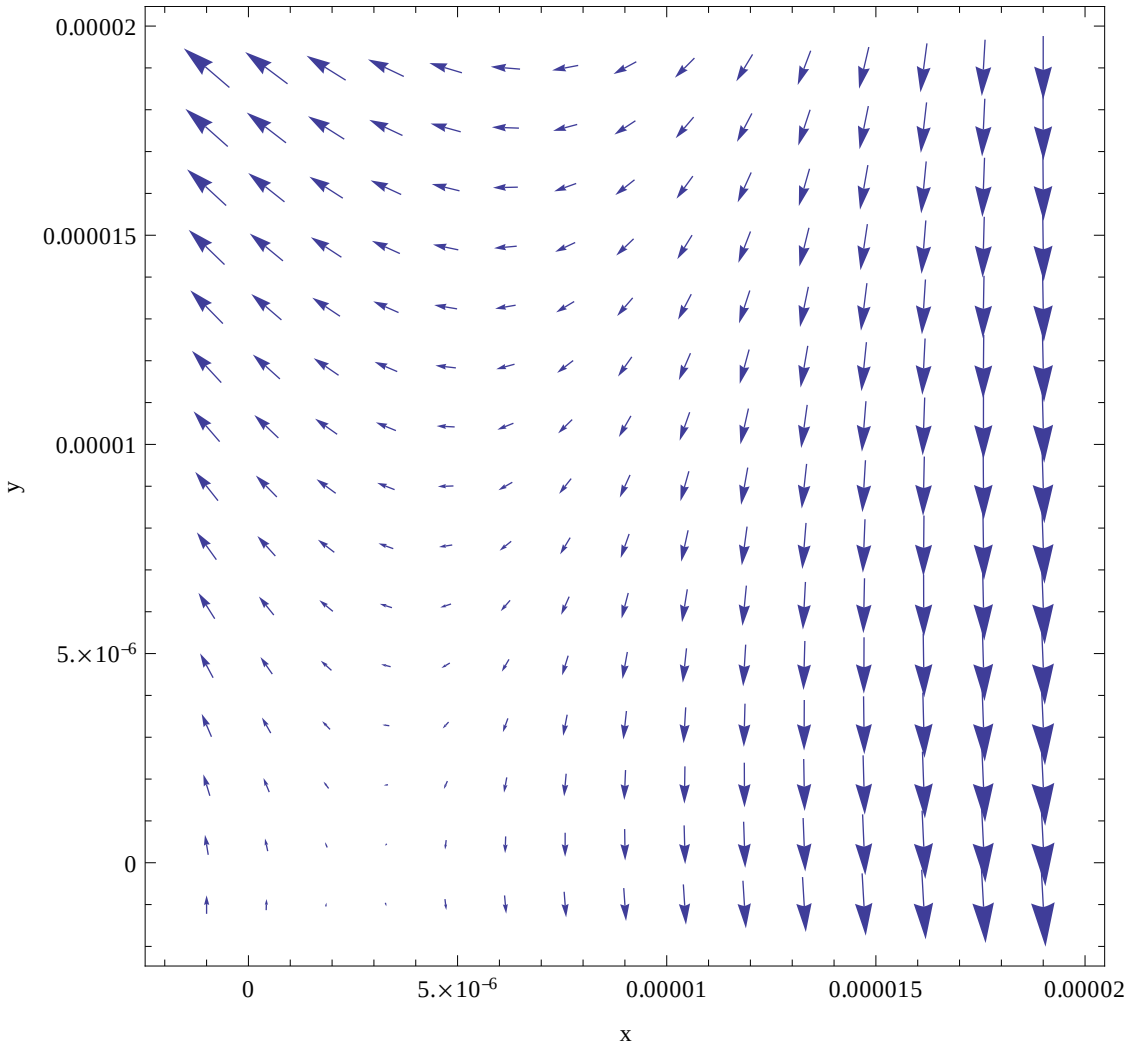

Figure 4.13: A vector graph of the magnetic trap, with the (radial) gradients turned on. The minimum is located at the spot where the arrows are smallest.

4.8.2 $z-$Gradient in the $z-$direction

A $z-$gradient in the $z-$direction can straightforwardly be applied by adding any function (dependent of z) to B_{abs}, for example:

$$B_{z,\text{grad}} = u(z - v) \tag{4.62}$$

Here, u and v are constants; u has units T/m and v has units m. This gradient can be used to shift the minimum of the trap in the $z-$direction. This does not yield a large change in trap frequencies, as shown in Figure 4.14.

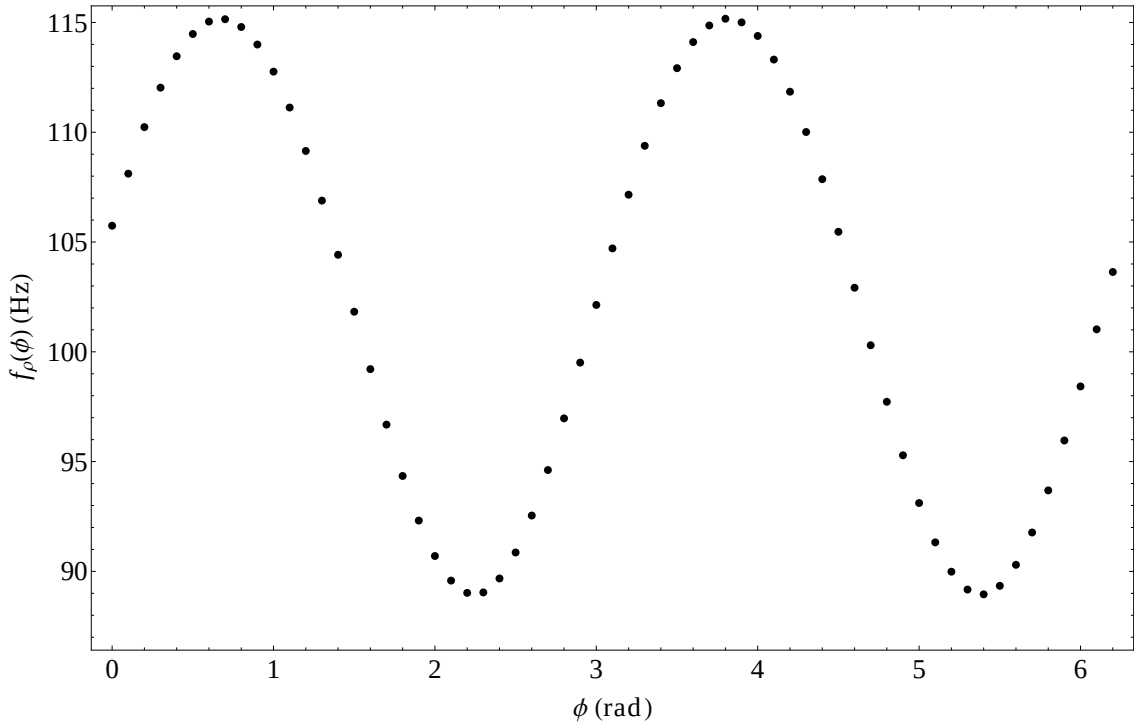

Figure 4.14: The radial trap frequency as a function of angle, after applying a gradient with $u = 0.3$ T/m and $v = 10^{-4}$ m. The current through the pinch and bias coils is set at 200A, the current through the cloverleaf coils is 320A. The result is an axial trap frequency of 15.9 Hz and a radial trap frequency of 102.49 Hz, with a large spread.

4.8.3 $z-$Gradient in the $\rho - \phi$ plane

A $z-$gradient in the $\rho-$direction can be applied by adding a function similar to Eq. (4.62), but instead of z the variables are ρ and ϕ. Also, a parameter for the angle of the gradient ψ' is added (please note that this can, but does not necessarily have to be different than the angle ψ in Section 4.8.1). It has, however, the same functionality. The gradient can be written as:

$$B_{z,\text{grad}} = u' + v'\rho\cos(\psi' - \phi) \tag{4.63}$$

Here, u' has units T and v' has units T/m. Although this gradient has only a component in the $z-$direction, its effect yields a change of the minimum of the trap in the $\rho - \phi$ plane. A result of applying this gradient is shown in Figure 4.15.

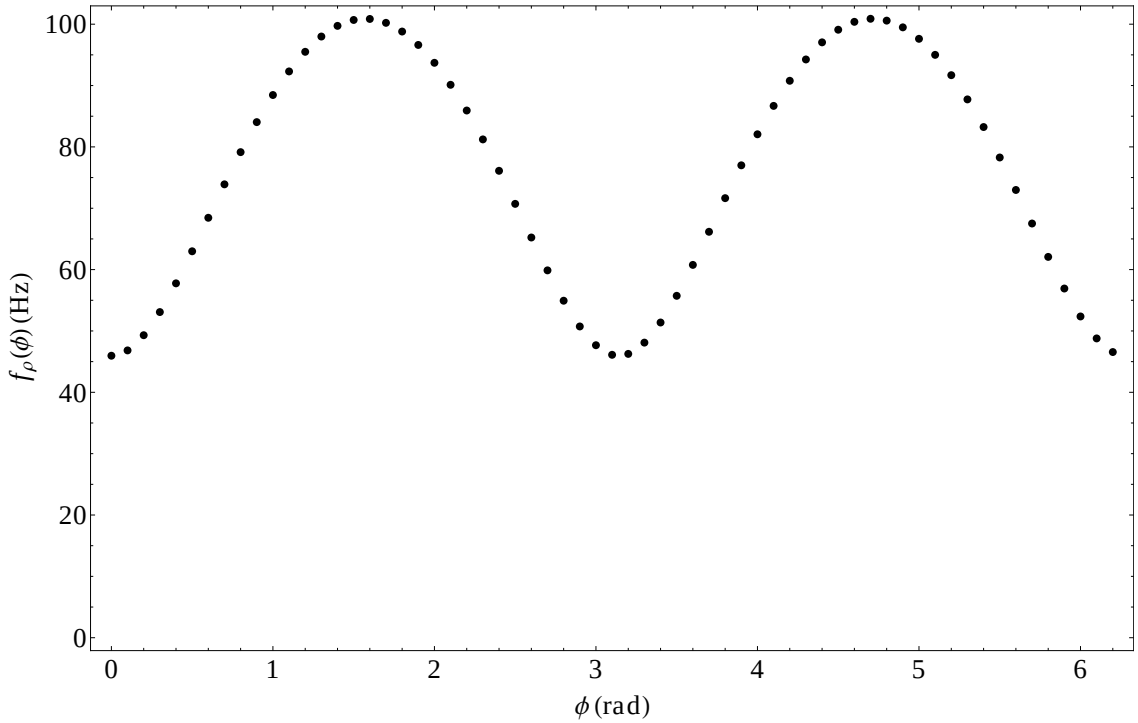

Figure 4.15: The radial trap frequency as a function of angle, after applying a gradient with $u' = 0.001$ T and $v' = 0.001$ T/m. The current through the pinch and bias coils is set at 200A, the current through the cloverleaf coils is 320A. The result is an axial trap frequency of 15.4 Hz and a radial trap frequency of 75.93 Hz, with a large spread.

4.8.4 Gradient in the $\rho - \phi$ plane in the $z-$direction

A $z-$gradient in the $\rho-$direction can be applied by adding a function similar to Eq. (4.62), but now the direction is not in the $z-$direction but in the $\vec{v_\psi}$ direction.Again, a parameter for the angle of the gradient ψ'' is added (which can, again have any value independent of ψ and ψ'). The gradient can be written as:

$$B_{\rho,\text{grad}} = (a' + b'z)\cos(\phi - \psi'') \tag{4.64}$$

$$B_{\phi,\text{grad}} = -(a' + b'z)\sin(\phi - \psi'') \tag{4.65}$$

Here, a' has units T and b' has units T/m. If this gradient is applied (with both a and $b \neq 0$), then the minimum of the trap is shifted in both the $\rho - \phi$ plane and in the $z-$direction.

4.8.5 Conclusion

In this section, the effect of adding gradients to the magnetic field of the cloverleaf trap was studied, with a focus on gradients in the $z-$direction. It can be concluded that adding gradients does change the characteristics of the magnetic trap, i.e. especially the radial trap frequency changes. Another phenomenon which occurs is that not only the average of this trap frequency changes, but also the spread as a function of angle. Without gradients, this spread is negligible, but with a $z-$gradient applied this spread becomes in the order of Hz. Together with this effect, the location of the minimum of the magnetic field changes, both in $\rho-$ and $z-$coordinates and the trap becomes asymmetric if the gradients are strong enough.
In this Section, a number of examples are illustrated with graphs. Of course, it is possible to apply more than one of the gradients described, with several possible combinations and magnitudes of the gradients. This yields different effects for different values of the parameters.

Chapter 5

Particle Flux: slow and fast

Authors: Johan van der Tol BSc and Martijn van 't Woud BSc.
Supervision: Alexander Groot MSc, Pieter C. Bons MSc and prof. dr. Peter van der Straten.

5.1 Introduction

In this chapter, some experiments involving the beam of particles that loads the Bose-Einstein condensate setup are described. First, a fast flux experiment (in which the Zeeman slower is turned off) is performed, in which the way the oven operates as a function of temperature, is investigated. The particle flux is determined by absorption measurements and these measurements are compared to calculations coming from the vapor pressure. We are able to show that scattering plays an important role in the way the oven operates. In slow flux experiments (in which the Zeeman slower is turned on), the power of the Zeeman laser is varied to find the behavior of both flux and particle speed. Also, by varying the currents through the Zeeman slower coils, the behavior of speed and flux of the sodium particles as a function of current is examined. We show that varying the current through the coils yields a more reproducible result than varying the Zeeman laser power. Also, we provide a model to calculate the speed as a function of current.

5.2 General description

If a beam of particles (for example photons) is moving through a medium, one can wonder how much of that beam is scattered. If one assumes that every particle in the medium has a certain collisional cross-section and that if one particle in the beam is scattered when it enters the area around the particle in the medium given by that cross-section, one can set up a differential equation which, when it is solved, gives the transmission of particles. This results in the so-called Beer-Lambert law for the transmission:

$$T = \exp\left(-\sigma \int \rho(x)dx\right), \tag{5.1}$$

where T is the transmission, σ is the cross-section, ρ is the density of the medium and the integral runs over the path of the beam. In the case of a homogeneous density ρ_0 this becomes:

$$T = \exp\left(-\sigma\rho_0 d\right), \tag{5.2}$$

where d is the distance traveled by the beam.

5.2.1 Resonant light

In the case of a beam of resonant light this means: $I = I_0 \exp\left(-\sigma_r \int \rho(x)dx\right)$, where σ_r is the resonant absorption cross-section. For two-level systems, this is given by $\frac{3\lambda^2}{2\pi}$ (see [15, Eq. 3.12]). However, since this is not the case, we multiply with the Glebsch-Gordan coefficient, which is

different for various polarizations and transitions and dependent on the detuning of this transition. So we obtain:

$$\sigma = c(\text{transition; polarization}; \Delta f) \cdot \frac{3\lambda^2}{2\pi}. \tag{5.3}$$

In the case of sodium for π-polarized light wavelength 589.16 nm, resonant to the $3^2S_{1/2} \rightarrow 3^2P_{3/2}$ transition, c is given by (see [15, Table 2.1 and Eq. 3.13] and [16, Appendix D]):

$$\begin{aligned} &c(F_g = 2 \rightarrow F = 1, 2, 3; \pi; \Delta f) = \\ &\frac{1}{30\left(\frac{16\pi^2\Delta f^2}{\gamma^2}+1\right)} + \frac{1}{6\left(\frac{16\pi^2(\Delta f - 3.4339\times10^7)^2}{\gamma^2}+1\right)} + \frac{7}{15\left(\frac{16\pi^2(\Delta f - 9.2649\times10^7)^2}{\gamma^2}+1\right)} \end{aligned} \tag{5.4}$$

for the transition $F_g = 2 \rightarrow F = 1, 2, 3$ used in Section 5.4 and c is given by:

$$\begin{aligned} &c(F_g = 1 \rightarrow F = 0, 1, 2; \pi; \Delta f) = \\ &\frac{5}{18\left(\frac{16\pi^2\Delta f^2}{9\gamma^2}+1\right)} + \frac{5}{18\left(\frac{16\pi^2(\Delta f + 3.4339\times10^7)^2}{9\gamma^2}+1\right)} + \frac{2}{9\left(\frac{16\pi^2(\Delta f + 5.0148\times10^7)^2}{9\gamma^2}+1\right)} \end{aligned} \tag{5.5}$$

for the $F_g = 1 \rightarrow F = 0, 1, 2$ used in Section 5.5. This means that if one measures what percentage A of light is absorbed, that one can determine the density of that medium by using:

$$1 - A = \exp(-\sigma_r \rho d) \rightarrow \rho = \frac{\ln\left(\frac{1}{1-A}\right)}{\sigma_r d}. \tag{5.6}$$

If the medium is a moving beam of sodium particles with speed v and diameter d_1 that flux will be given by:

$$F = \frac{\pi d_1 v \ln\left(\frac{1}{1-A}\right)}{4\sigma_r} \cdot \frac{\cos(\phi)}{n}, \tag{5.7}$$

where n is the number of passes, and ϕ is the incident angle. In Section 5.4 $\frac{\cos(\phi)}{n}$ is $\frac{1}{2}$ and in Section 5.5 it is $\frac{1}{2\sqrt{2}}$.

5.2.2 Beam of sodium particles

In the case of a beam of sodium particles with a flux (in particles per second) moving through a low density gas of sodium particles this means that the incoming flux F_0 is related to the outgoing flux F by:

$$F = F_0 \exp(-\sigma_s \rho_0 d), \tag{5.8}$$

where σ_s is the sodium-sodium scattering cross-section, given by $100 \cdot 10^{-18}$ m^2. [17, Table 2.1]

5.3 Experimental setup

A schematic representation of the experimental setup is shown in Figure 5.1. The setup consists of a recirculating oven, a Zeeman slower and a vacuum chamber. The sodium particle beam emerges from the vapor pressure of a heated sodium source in the first chamber of the oven (see Section 5.4.1) and then enters the second chamber through a diaphragm of 6 mm, and then the third chamber through a diaphragm of 10 mm. [15]

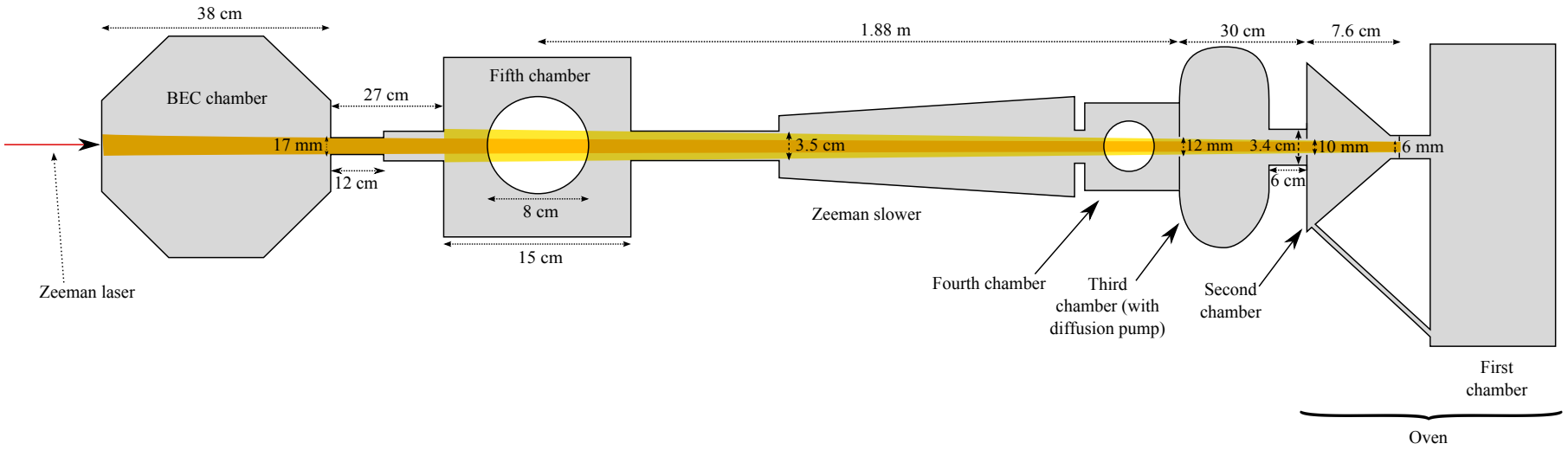

Figure 5.1: Overview of the setup used. The effective beam used for the fast flux (Section 5.4) is yellow, the effective beam used for the slow flux (Section 5.5) is brown.

The measurements of the fast flux (see Section 5.4) are performed in the vacuum chamber located between the BEC chamber and the Zeeman slower, whereas the measurements of the slow flux (see Section 5.5) are performed in the BEC chamber. Only the sodium atoms which pass through the corresponding chamber (i.e. have the correct solid angle) can be used in the measurement for the flux. This angle is (in first order, larger orders can be neglected) determined by the relation $\theta = \arctan\left(\frac{d}{2l}\right)$ where d is the width of the limiting component and l is the distance from the 6 mm diaphragm to that component. The component which yields the smallest angle determines the width of the beam. In Section 5.4, the width of the beam is determined by the width of the small pipe between the cubic chamber and the Zeeman slower (with diameter 3.5 cm). In Section 5.5, it is determined by the 17 mm thick pipe between the vacuum chamber and the cubic chamber.

For small angles, the width of the beam can be calculated by a small angle approximation, so $d_0 \approx L\theta$ where L is the distance from the 6 mm diaphragm to the point where the measurement was performed. Inserting the appropriate values yields a beam width of 1.8 cm for the slow flux and 3.6 cm for the fast flux. The value of 3.6 cm is confirmed by a photograph of the window in the vacuum chamber, of which the diameter is known.

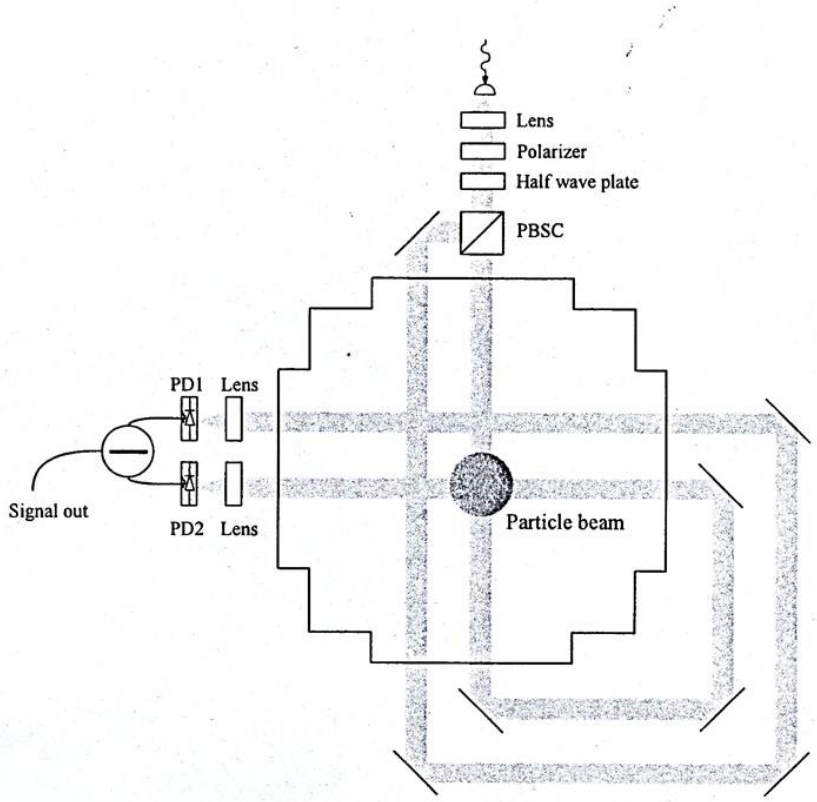

Figure 5.2: The fast flux setup. The two beam trajectories are shown, together with the sodium atom beam. [18]

5.4 Fast flux varying the oven temperature

In the experiment described in this Section, absorption measurements are performed while the temperature of the oven is varied. In that way, the operation of the oven can be understood thoroughly. Apart from the general setup described in Section 5.3, in Section 5.4.1 the setup relevant for this experiment will be described. In Section 5.4.2, the Lorentzian formula will be introduced (Section 5.4.2) and a calculation which converts absorption values into flux, including a prediction of the expected flux, will be described (see Section 5.4.2). In Section 5.4.3, the results

will be presented and in Section 5.4.4, they will be discussed and conclusions will be presented.

5.4.1 Setup

During the measurements of the fast flux, the Zeeman slower is turned off. A fraction (see Section 5.3) of the particles passes through the cubic vacuum chamber (labeled 'Fifth chamber' in Figure 5.1), where the measurements take place. This is done using a probe laser beam (using the transition $F_g = 2 \rightarrow F_e = 1, 2, 3$), which is split into two separate light beams using a polarizing beam splitter cube (PBSC). The polarization of the light beams can be tuned using a waveplate. One of these light beams only passes through the chamber twice (without crossing the particle beam), before hitting a photo diode. The other light beam crosses the particle beam twice with an angle of 90 degrees before hitting another photo diode. For a schematic representation, see Figure 5.2. The two photo diodes are connected to a differential amplifier, which measures the difference between the two signals. This amplifier is connected to an oscilloscope, which is used for obtaining the data for the experiment described in Section 5.4.3. For this experiment, the particle flux as a function of oven temperature is measured. The oven consists of 3 chambers. In the first chamber (where the temperature is varied between 295 and 325 °C), a block of sodium is present. Through a 6 mm diaphragm, the atoms enter the second chamber, where also a recirculation pipe is present (this is also shown in Figure 5.1). Only the atoms with the correct solid angle (see Section 5.3) will then enter the third chamber, to which a diffusion pump is connected. The other atoms remain in the second chamber, will liquefy and go back to the first chamber via the small pipe connecting these chambers.

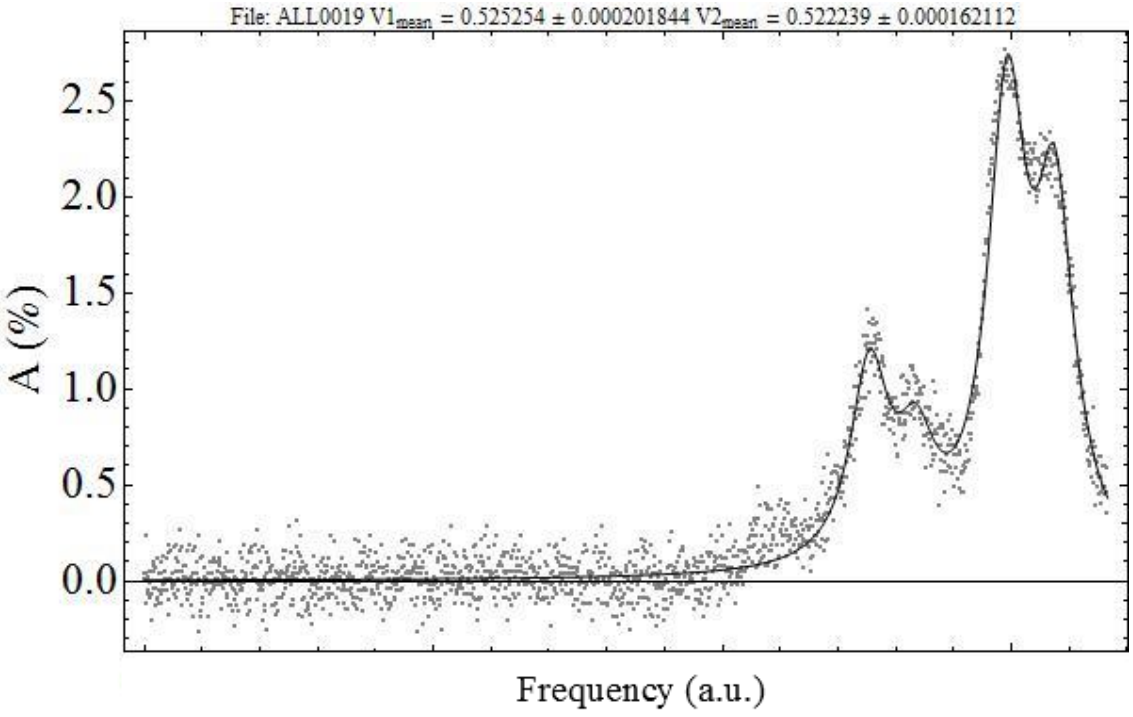

Figure 5.3: Example of a fit to the absorption data of the fast flux. Based on Eq. 5.4, one would expect 3 peaks. One of these peaks is actually really small. The reason we see four peaks (which correspond to four Lorentzians), is because a Doppler shift can occur between the two passes.

5.4.2 Theoretical description

Lorentzians

In Figure 5.3, an example of a fit to the absorption data of the fast flux is shown. In order to obtain this fit, a superposition of four Lorentzian line shapes is used, which obey the general formula:

$$L(\omega) = \frac{(\Gamma_{eff}/2)^2}{(\omega - \omega_0)^2 + (\Gamma_{eff}/2)^2} \tag{5.9}$$

where Γ_{eff} is the effective linewidth, ω_0 are the resonance frequencies of the transitions (for the fast flux $F_g = 1 \rightarrow F_e = 0, 1, 2$) and ω is the laser frequency. From this fit, the absorption can be found and compared with Eq. 5.4. In turn, from the absorption the flux (particles per second) of sodium atoms can be calculated.[1]

Flux and vapor pressure

As discussed in Sections 5.2.1 and 5.2.2, one can calculate the sodium-flux in particles per second from the absorption. In Section 5.4.3 the absorption and thus the flux is measured as a function of oven temperature. One can also make a prediction of this flux based on the vapor pressure of the oven. This vapor pressure will determine the pressure in the first chamber. The vapor pressure of sodium is given by:

$$P = P_0 \cdot 10^{A - \frac{B}{T}}, \tag{5.10}$$

with $A = 4.51961$, $B = 5202.12$K, and $P_0 = 1$ atm $= 101325$ Pa. Assuming the ideal gas law this gives the density as $\rho_1 = \frac{P_0}{kT} \cdot 10^{A - \frac{B}{T}}$. In Section 5.3 it is mentioned that the pipe connecting the Zeeman slower and the measurement chamber determines the angle at which particles move to reach the measurement point. This angle can be converted into a solid angle, and since this angle is very small, the fraction h of that to the total solid angle gives the amount of particles moving in the right direction. Further, we know that the particles leave the first chamber by a hole of diameter $d_0 = 6$ mm [19]. The flux at the measurement point is now given by:

$$F = \frac{\pi d_0^2}{4} v \rho_1 h. \tag{5.11}$$

The speed v is the same as the speed used in Section 5.2.1 and therefore, its value does not matter for comparison, but for the axes of the graphs we will just use the thermal velocity of $\sqrt{\frac{3kT}{m}}$. [2] The flux now becomes:

$$F = \frac{\pi d_0^2}{16} \sqrt{\frac{3kT}{m}} \rho_1 \arctan^2\left(\frac{d}{2l}\right) \tag{5.12}$$

where $d = 3.5$ cm is the diameter of the pipe and $l = 2.181$ m is the distance of the pipe to the hole in the first chamber. This flux is a function of temperature in the first chamber, which is varied in the experiment.
The problem with this formula is that there is no account for the fact that the flux passes a second and a third chamber after leaving the first. There is no reason to assume that there is absolute vacuum in these chambers and that means that a part of the flux will be lost. This loss can be calculated using the Beer-Lambert formula from Section 5.2. If F_0 is the flux we expected at first, the flux at the measurement point will be given by:

$$F = F_0 \cdot \exp\left(-\sigma_s \rho_2 l_2\right) \cdot \exp\left(-\sigma_s \rho_3 l_3\right) \cdot \exp\left(-\sigma_s \int \rho_z(x) dx\right), \tag{5.13}$$

[1] However, it must be noted that Eq. 5.4 consists of 3 terms, corresponding with 3 transitions. One of them is too small to be visible, and the 4 visible peaks can be divided into two groups corresponding to the two passes. These groups could be fitted separately, and the average could be taken in the analysis, but this is not done.

[2] Note that this velocity occurs on both equations and its value is of no importance. Further, $\sqrt{\frac{8k_BT}{m\pi}} \approx \sqrt{\frac{3k_BT}{m}}$.

where l_x is now the length of a chamber and the subscripts respectively refer to the 2nd and 3rd chamber and the Zeeman slower. The integral is still in the formula because there is a pressure difference between the right-hand and the left-hand side of the slower, but if we assume a linear gradient this will just result in the average of the two sides and then

$$F = F_0 \cdot \exp\left(-\sigma_s \rho_2 l_2\right) \cdot \ exp(-\sigma_s \rho_3 l_3) \cdot \exp\left(-\sigma_s \bar{\rho}_z l_z\right). \tag{5.14}$$

Considering Figure 5.1 of the setup, the densities here originate probably mostly from the first chamber particles that did not have the angle needed to reach the measurement chamber, and taking into account that the third chamber has a diffusion pump to keep the density low, we can assume that the $\exp\left(-\sigma_s \rho_2 l_2\right)$ term coming from the second chamber probably has the largest contribution, also because it is right next to the first chamber and the only way out for the particles is to the third chamber and through the little recirculation pipe. Unfortunately we can only measure the pressure in the third chamber and the Zeeman slower directly, and not in the second chamber. In the third chamber we measure a temperature of 301 Kelvin, and a pressure of $1.45 \cdot 10^{-7}$ mBar, corresponding with a density of $3.49 \cdot 10^{15}$ m^{-3}. Using that it has a length of 23.5 cm we see that the exponent gives 0.92 so about 8% of the particles passing through the third chamber gets lost due to scattering. In the Zeeman slower we measure a pressure of $1 \cdot 10^{-8}$ mBar on one side and $2 \cdot 10^{-9}$ mBar on the other, yielding an average density of $1.48 \cdot 10^{14}$ m^{-3}. Using the length of 1.88 m and assuming room temperature we see that about 3% of the particles going through it get scattered in the Zeeman slower. Both are not even close enough to account for the factor 20. This strongly indicates that we should find out the density in the second chamber. Since it is in equilibrium via a 10 mm hole with the third chamber, we can calculate it from the third chamber. Let's take a closer look at the third chamber. There are 3 connections with the outside world. There is the pump, which has a pump capacity of 1200 l/s, there is the hole to the second chamber and to the third chamber. It can be derived the time derivative of the density in the third chamber is given by:

$$\partial_t \rho_3 = \frac{C_{23} \cdot \Delta\rho_{23}}{V_3} - \frac{C_p \cdot \rho_3}{V_3} - \frac{C_{3z} \cdot \Delta\rho_{3z}}{V_3}, \tag{5.15}$$

where C is the pump capacity through the holes in volume per time and C_p the capacity of the diffusion pump. The subscripts indicate the second and third chamber and the Zeeman slower. We know $\Delta\rho 3z \approx \rho_3$ and assuming equilibrium, this means that $\partial_t \rho_3 = 0$ so since $\Delta\rho_{23} = \rho_2 - \rho_3$ we obtain:

$$\rho_2 = \frac{(C_p + C_{3z}) \cdot \rho_3}{C_{23}} + \rho_3. \tag{5.16}$$

Using a working formula for the C of a circular opening, that is $C = 0.113 \cdot R^2 \sqrt{\frac{T}{M}} \cdot$ l/sec and that of a short tube, $C = 0.31 \cdot \frac{R^3}{2.7R+L} \sqrt{\frac{T}{M}} \cdot$ l/sec where R is the radius, L is the length of the short tube, all in mm and M is the molar mass, and realizing C_{23} is a series resistance of a hole of 10 mm and a short tube of diameter 34 mm and length 60 mm, we can now calculate the expected density in the second chamber.[20] This turns out to be $4.6 \cdot 10^{17}$ m^{-3}. Realizing the length of the second chamber is 7.6 cm, we now see that fraction of particles that get through the second chamber $\exp\left(-\sigma_s \rho_2 l_2\right)$ is 0.35, indicating that we expect about 97% (!) of particles to get lost in the second chamber.

5.4.3 Measurements & results

In the experiment we measure the absorption of the light. As said before in Section 5.4.2 we can calculate the flux from that. By varying the oven temperature we can obtain the flux of particles as a function of oven temperature. Next we can compare this with the expected flux of particles that leave the first chamber and have the correct angle to reach the measurement point based on the vapor pressure. Measurements were done in a temperature range of 290-330 °C. When looking at our data, we get about 55 times as less particles as expected, corresponding to absorption percentages of depending on temperature 2-5% where one would expect 55-95% absorption (a percentage to our knowledge never measured before in this setup).

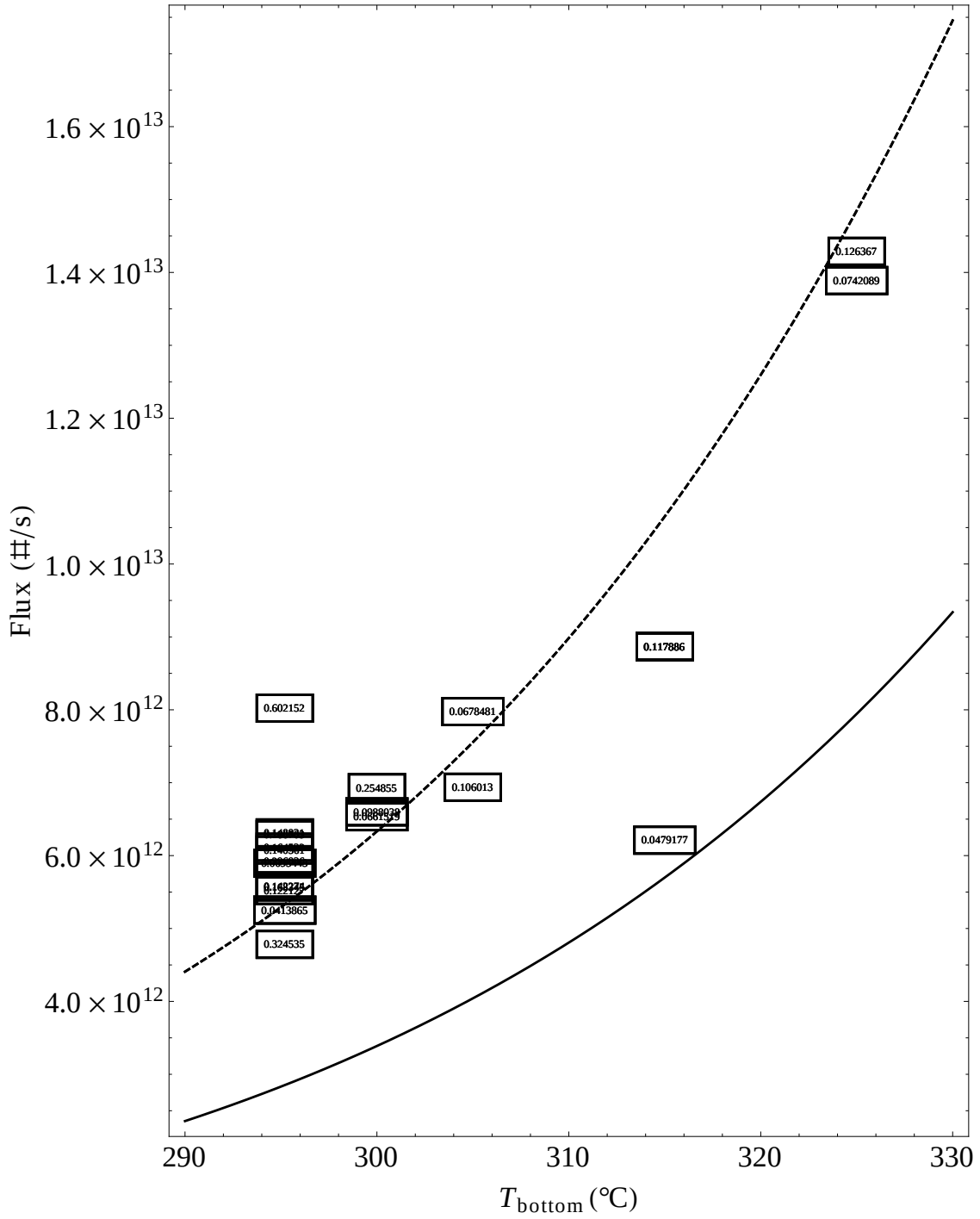

Figure 5.4: The particle flux versus the temperature of the bottom of the oven. The values in the frames indicate the fraction of saturation on which is measured. The solid line is the prediction, the dashed line is the fit. It can be seen that the values of the flux are highly sensitive to the density in the second chamber, as the difference in density is only 10%. The difference in the graph is a factor 1.4, because we are now in the highly nonlinear part of the exponent.

But this is of course without the scattering losses discussed before. Considering the numbers discussed in the previous Section the expected flux should be lowered by a factor of 38. This 'expected' [3] line is plotted as the solid line in Figure 5.4. There is a large difference between the

[3] Of course this expected flux includes measurements of the pressure and temperature at different places in the setup.

data and the expected line. But what we should take into account is that the solid line is for a huge part determined by the density in the second chamber, which was estimated in the previous Section as $4.6 \cdot 10^{17}$ m^{-3} because this is calculated from the values in the second chamber. Its temperature was measured quite roughly, and its pressure was measured against a background pressure which can be nonzero (making the density in the third chamber higher, and so the density in the second chamber), so the value of $4.6 \cdot 10^{17}$ m^{-3} has an unknown uncertainty. Taking our densities in the third chamber and the Zeeman slower as correct for their part in the scattering processes (realizing that their influences where small anyway), we can make a fit to the data with the density in the second chamber as a parameter. This results in a value of $(3.8061 \pm 0.048) \cdot 10^{17}$ m^{-3}. This fitted line is shown as a dashed line in Figure 5.4. One thing to consider is if this second chamber density does not contribute to the flux, because it gives again a pressure itself. Calculating this shows that it does not significantly contribute, not surprising realizing that the densities in the first chamber depend on temperature in the order of $10^{20} - 10^{21}$ m^{-3}.

5.4.4 Discussion

The expected value of $4.6 \cdot 10^{17}$ m^{-3} is not accurate because there are a certain number of values coming from the third chamber which are used but are not that accurately known, while we do not have a value to estimate an uncertainty in this.
The fit that was made originally had an estimated variance of 7954, way larger than the expected 1. The uncertainty in the data points for the absorption however comes itself from a fit of four Lorentzian functions (see Section 5.4.2), and we see that the uncertainties coming from that in no way correspond to the fluctuations in the measurement. For example, for the temperature of 295 degrees Celsius where a lot of measurements were done we see a spread of $1.54 \cdot 10^{12}$ around an average of $9.52 \cdot 10^{12}$ particles per second, orders of magnitude larger than the uncertainties that come from the Lorentzian fit (which are in the order of 10^{10}). To correct for these way underestimated uncertainties we multiply them with the square-root of the estimated variance, to get a corrected uncertainty for the final fit. Better would be to do more measurements at a certain temperature to get the spread in absorption from there.

5.4.5 Conclusion

We can conclude that our model seems to correspond with the data in order. The order of the density that comes out for the second chamber is calculated in two distinct ways and seems to match within 30%. We cannot tell how significant this difference is, because the uncertainty on the value of $4.6 \cdot 10^{17}$ particles per second is unknown. Due to conservation of mass, it is impossible to measure a higher particle flux than the solid line in Figure 5.4 if the data it is based on, is exact. This suggests that the uncertainty in the value $4.6 \cdot 10^{17}$ is quite large. But the most important conclusion to draw from these measurements is that we have to deal with enormous scattering losses. We lose 3% of our particles do to scattering in the Zeeman slower, 8% in the third chamber, and a much larger number of **97%** in the second chamber, proven by the densities determined in two separate ways in the second chamber.
We can conclude that if there is a way to lower the density in the second chamber, that it must be possible to increase the flux with an order of magnitude. For example if the density in the second chamber is reduced by a factor of 10, the flux increases with a factor of more than 20. Also an increase in the density in the Second Chamber corresponds to a steep decrease in the flux, increasing this density with a factor of 10 brings the flux to about 1 particle every 10 seconds, so virtually none.

5.5 Slow flux

In the slow flux experiments, Doppler shift starts to play a role (see Section 5.5.1). The setup components which are specific for these experiments are described in Section 5.5.2. In Section 5.5.3, an experiment describing the absorption as a function of Zeeman power is described. In Section 5.5.4, the speed is being tweaked by varying the values of the compensation coils of the Zeeman slower.

5.5.1 Theoretical description

Because the probe beam passes the atom beam with an angle of 45 degrees (see Section 5.5.2), this induces a Doppler shift. The first time the probe beam crosses the atoms, the component parallel to the atoms is in the same direction as the velocity of the atoms (moving away from the source) so the observed frequency is smaller than the non-Doppler shifted frequency. When the probe beam comes back, the component parallel to the atom beam is in the opposite direction of the velocity of the atoms, so the observed frequency is larger than the non-Doppler shifted frequency. Together, this leads to a double Doppler shift which can be expressed as $\Delta f = \frac{2v \sin(\theta)}{c} f_0$ with $\Delta f = f_2 - f_1$. An example of a fit (with Doppler shift) can be seen in Figure 5.5. Again, four Lorentzians were used for this fit, but two of them are just the other two Doppler shifted. So, we can only distinguish two Lorentzians in the characteristic of this transition. As discussed in Sections 5.2.1 and 5.2.2 one can calculate the sodium-flux in particles per second from the absorption. In this case the $\frac{\cos(\phi)}{n}$ is $\frac{1}{2\sqrt{2}}$. The difference with the fast flux measurements is that we now have a lower speed. This speed is now no longer taken as the thermal velocity, but instead determined from the Doppler shift as mentioned above.

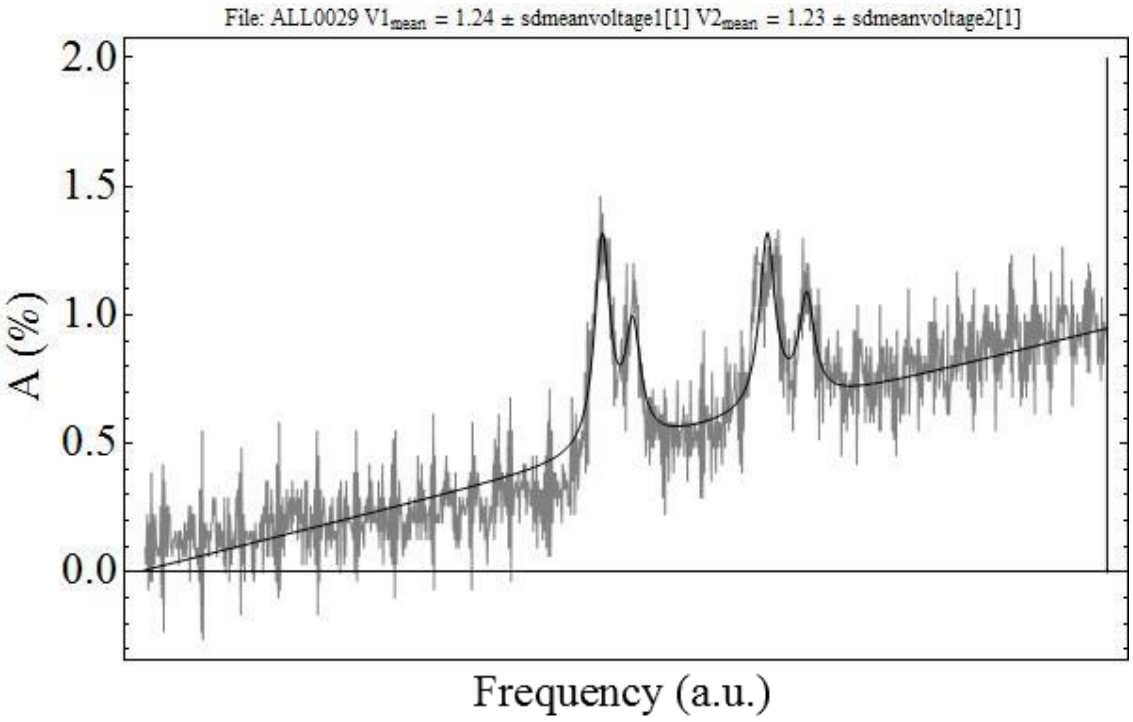

Figure 5.5: Example of a fit to slow flux data with Doppler shift and an offset function, which has to be subtracted from the curve in order to get correct absorption values.

5.5.2 Setup

During the experiments described in this section, the Zeeman slower is turned on. The Zeeman slower consists of a laser beam which slows the atoms, and of magnetic coils. Together, these give a Zeeman shift to the atoms which are on resonance, which causes them to slow. Now, the measurements are performed in the vacuum chamber (labeled 'BEC chamber' in Figure 5.1), where (as can be seen in the picture in Figure 5.6) the probe beam (now with the transition $F_g = 1 \rightarrow F_e = 0, 1, 2$) is again split into two beams using a PBSC. One beam is immediately directed into a photo diode. The other beam first passes the PBSC and then passes the atom beam with an angle of 45 degrees (two times, back and forth) before it is directed into another photo diode. These photo diodes are connected to a differential amplifier which also measures the difference between the two signals. These three signal outputs are connected to two oscilloscopes to provide data for the experiments described in Sections 5.5.3 and 5.5.4.

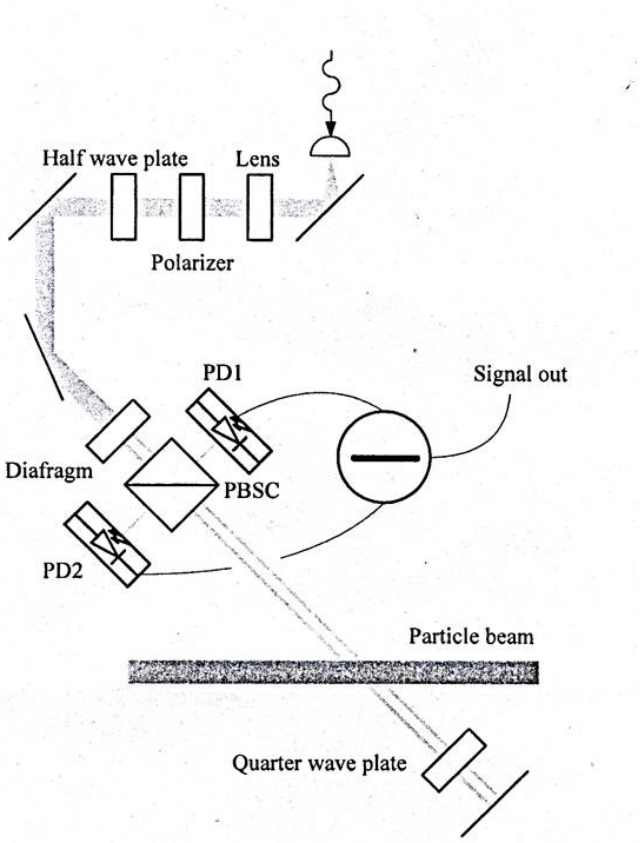

Figure 5.6: The slow flux setup. [18]

5.5.3 Experiment 1: Varying the Zeeman power

Measurements & results

In this experiment the power of the Zeeman laser is varied to measure the effects. Measurements were done in a range from about 40 to 120 mW. The effect of the laser power on the speed seemed to be marginal, though a small insignificant slope was observed, making the speed about 4% smaller at 120 mW than at 40 mW (see Figure 5.7). As will be described in Section 5.5.4 the speed can be varied by tuning the current in the coils in the second part of the Zeeman laser. Varying the Zeeman power does seem to have an effect on the absorption percentage. As said before, from these absorption percentages we can directly calculate the flux. Because of the fact that at these low absorption percentages $\ln\left(\frac{1}{1-A}\right) \approx A$ in very good approximation, and because of the fact that the speed is nearly constant, the flux versus Zeeman power will have a similar shape as the absorption percentage versus Zeeman power. That said, only the flux versus Zeeman power is shown (see Figure 5.8). A raise in flux when increasing the Zeeman power is shown. But we also see a strange variation in the flux. This variation was also observed in a different experiment (done before the absorption measurement) where the intensity of the laser was varied. There, the variation in the maximal absorption was about 0.2% around an average of 0.6%, about the same as we see here at the higher Zeeman values.

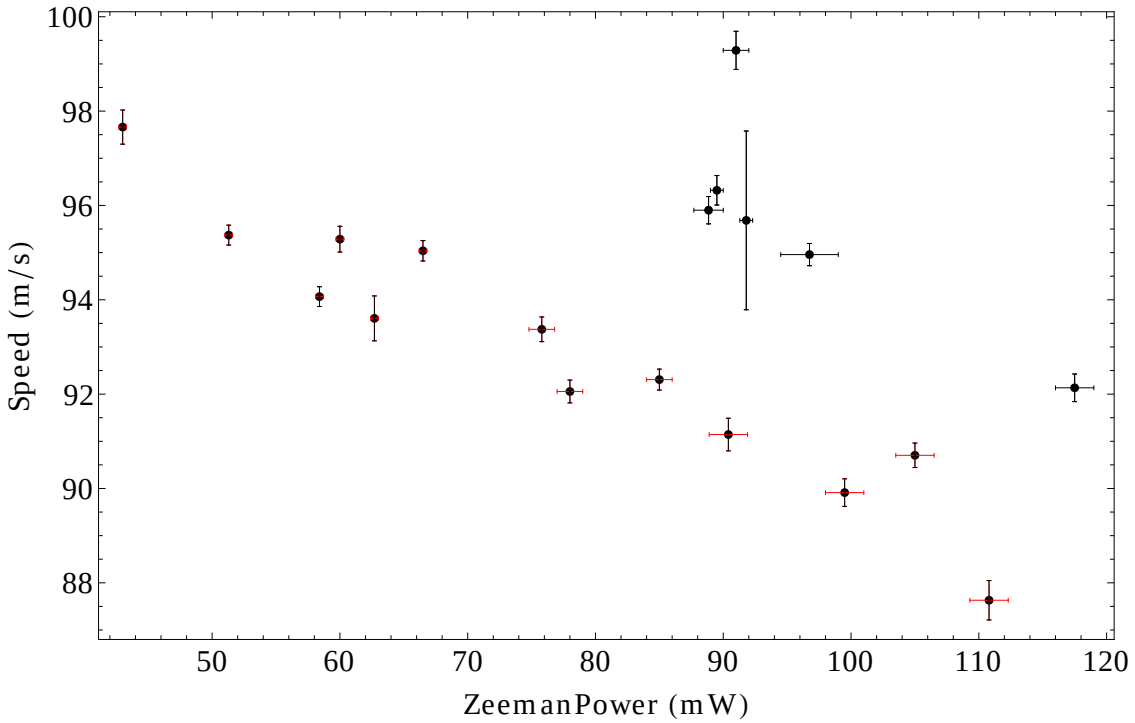

Figure 5.7: A graph of the speed versus the Zeeman power. The speed seems to be nearly constant with a slight decrease and fluctuations that are larger than expected based on the uncertainty of the data.

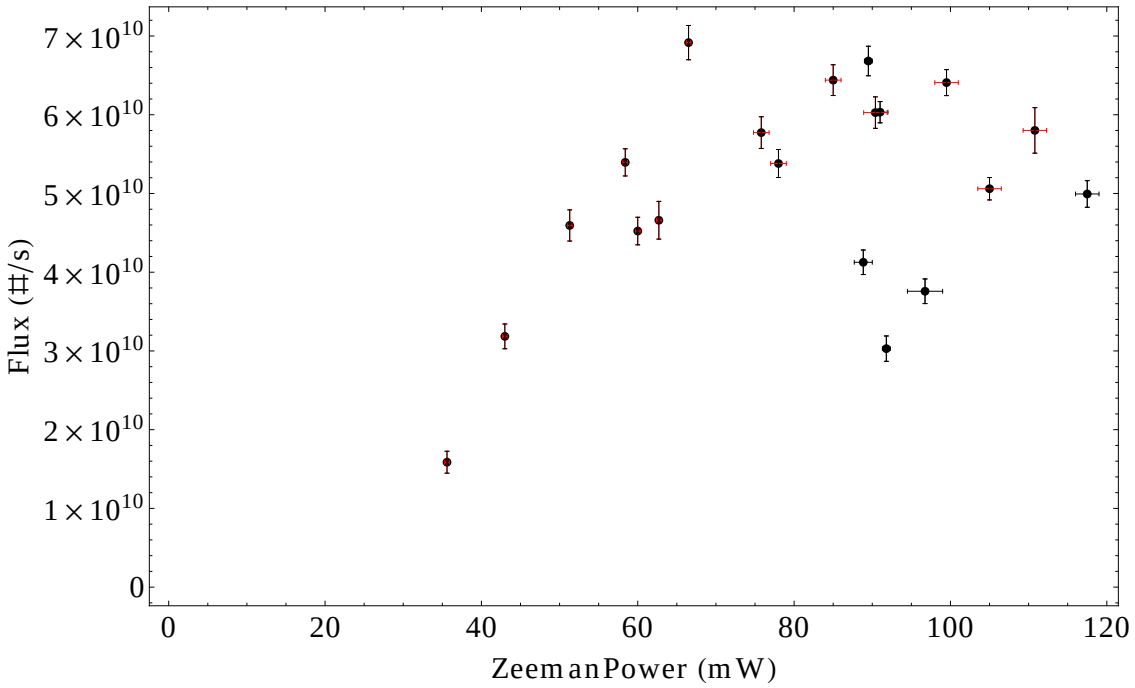

Figure 5.8: Graph showing the flux as a function of the Zeeman power. The data is noisy. We can conclude however that the Zeeman power influences the flux. The red uncertainties are estimated, the black in the Zeeman power are based on before and after measurements. The uncertainties in the fluxes are calculated from the Lorentzian fits taking into account the covariances.

Discussion

As mentioned in Section 5.4.4, the uncertainty in the data points for the absorption comes from a fit of two Lorentzian functions (or actually four, but these are Doppler shifted so two are relevant, see Section 5.5.1), and we see that the uncertainties coming from that in no way correspond to the fluctuations in the measurement. In this measurement it is even more extreme than before with fluctuations of about 0.2 percent around an average of 0.6 when varying the power of the measurement laser. The same kind of fluctuations are observed when varying the Zeeman laser power. These variations don't seem to be that extreme in the experiment in Section 5.5.3so there seems to be going something wrong when touching the lasers.

Conclusion

We can conclude that we observe an increase in flux when increasing the Zeeman power. Large fluctuations make the result not significant. A lot more measurements are needed if one would want to eliminate them.

5.5.4 Experiment 2: Speed tuning

Setup

In this experiment, the effect on the Doppler shift (and velocity of the atoms) due to the settings of 2 different coils on the Zeeman slower is investigated. These coils include the 'Master' and 'Compensation' coils. In the experiment, only the current of both coils was varied (the voltage was kept constant). Both of these coils are located at the second part of the Zeeman slower. The Master coil induces a magnetic field at the second part of the Zeeman slower (next to the MOT-chamber, which is labelled BEC-chamber in Figure 5.1), but the magnetic field lines are also present at the exact spot of the MOT (magneto optical trap), which is unfortunate because in this trap, the field should be zero. To achieve this, the compensation coil is present.

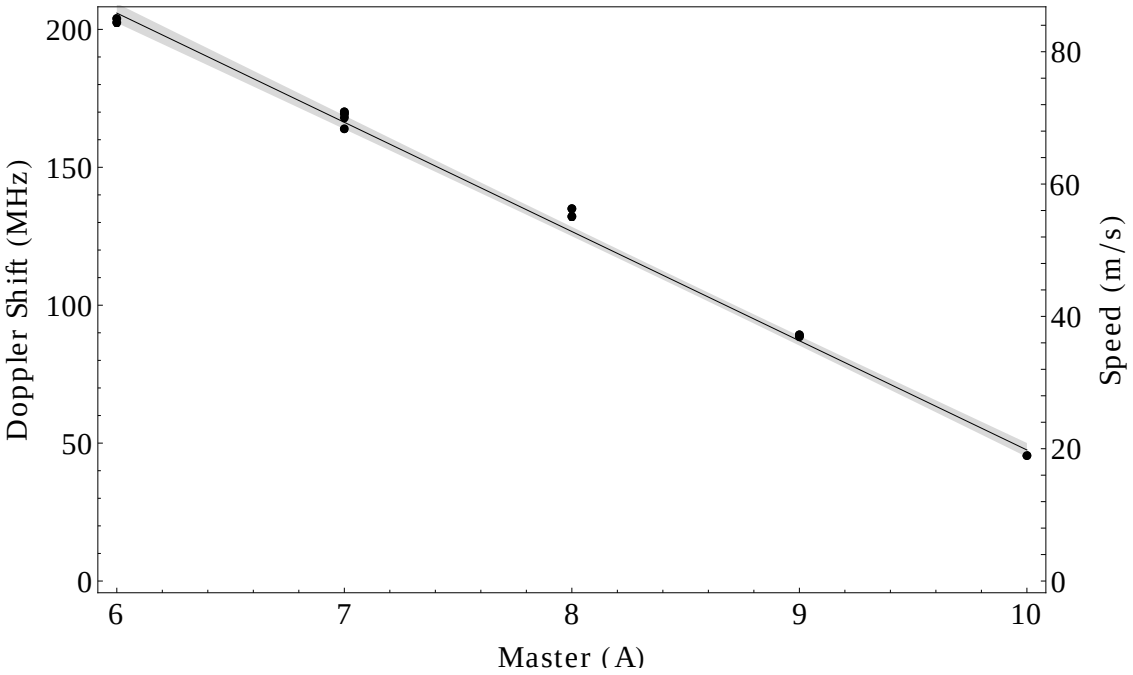

Figure 5.9: Doppler shift as a function of the master at 7.0 A of the compensation coil. On the right-hand side the speed is shown. A clear negative slope is seen with a much larger impact than obtained when varying the compensation coils. A higher master means a lower speed. The fitted line is linear and the grey area is two times the uncertainty of where the line should be.

This component consists of one coil, which produces a second magnetic field which cancels the magnetic field induced by the Master coil at the spot where the MOT is. In this way, the second part of the Zeeman slower can be used for further slowing and at the same time, there is no magnetic field in the MOT. In this Section, the focus will be on the effect of the Master coils. The effects of the compensation coils will also be described.

Measurements & results

As described in Section 5.5.4 the speed of the particles can be tuned by varying the current in the coils in the second part of the Zeeman slower. It turns out that when varying the current in the Master, a huge effect on the speed is observed. The higher the current, the lower the speed. Varying the current in the compensation coil has a smaller effect on the speed, going the opposite way, a higher current there means a higher speed.

Speed versus current In the measurements we varied two things, the current in the Master coil and the current in the compensation coil. The effect on the speed is measured. In Figure 5.9, the speed as a function of the value of the current in the master is shown (at the right-hand axis, the left-hand axis shows the Doppler shift), at a constant amperage of 7A in the compensation coil. It seems to go almost linear. In general, the compensation coil is there to compensate the Master and cannot be chosen free in value as in this experiment. For that, it is interesting to see the whole plane of varying both the Master coil and the compensation coil. In Figure 5.10, the Master is kept constant at 7A, and the compensation coil is varied. Again, the behavior seems linear. Next the Master is set constant at 10A and the compensation coil is varied. But now a problem appears. As described in Section 5.5.1 the speed is determined by looking at the shift of the transition.

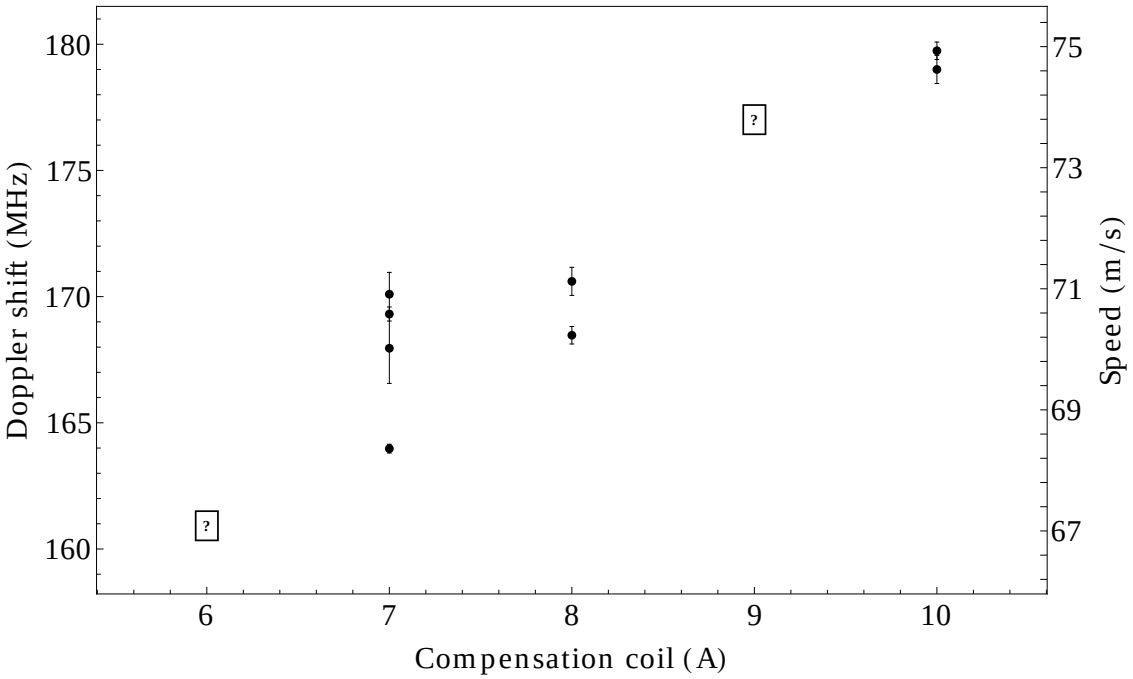

Figure 5.10: Doppler shift when varying the compensation coil, at a constant Master of 7.0 A. The question marks correspond to measurements where the values were not fitted to Lorentzians, but directly read from the oscilloscope. The line seems linear again, but small compared to Figure 5.9.

But now, this shift becomes so small that the two start to overlap. It is now no longer possible to distinguish more than two Lorentzians. The question now is if the distance between these two comes from the internal characteristics of the transition or from the Doppler shift. To

determine this we look at the other measurements where we do have four Lorentzians and realize that the distance between the two internal peaks must be constant. We now calculate from all other measurements this short peak distance. It gives a weighted average of 38.52 MHz with an Standard Deviation On Mean of 0.62 MHz and a weighted standard deviation of 2.25 MHz. The value for the internal peak distance could quite well differ two SDOM for a single measurement, but two times the Standard Deviation itself is quit improbable. That means that if a value for the distance is larger than 43 MHz we can quite surely say that it can't be an internal peak distance, so it must be a Doppler shift.

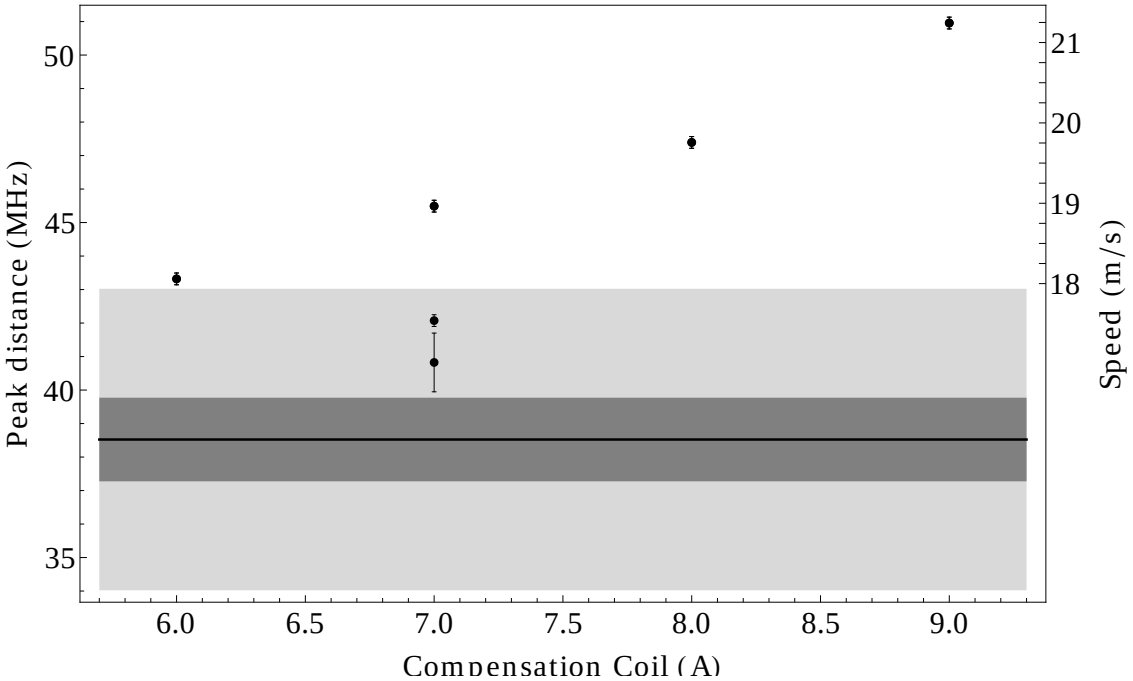

Figure 5.11: Peak distances when varying the compensation coil, at a constant Master of 10 A. If a point is outside the light-gray area, we are sure it is a Doppler shift and it corresponds to a speed. If it is in there, it can be a characteristic of the peak.

In Figure 5.11 it becomes clear that 4 of the 6 points are surely Doppler shifts. The other two can well be internal peak distances so they will not further be included. Now one observes linear lines in Figure 5.10, in Figure 5.11 and Figure 5.9. We now generalize this linear behavior to the idea that all can be approximated linear in the [6A,10A]x[6A,10A] plane. If every line in one variable must be linear while keeping the other constant it can be proven that there is only one function to fit these conditions. That function is: $v = C_1 I_M I_S + C_2 I_M + C_3 I_S + C_4$. Fitting this to our data turns out to work quit well. The resulting function is:

$$\begin{aligned} v = {} & (-0.266 I_C I_M + 3.635 I_C - 14.862 I_M + 160.99) \\ & \pm \sqrt{\begin{array}{c} 0.0170252 I_C^2 I_M^2 - 0.318035 I_C^2 I_M + 1.51059 I_C^2 - 0.258096 I_C I_M^2 \\ +4.82355 I_C I_M - 22.915 I_C + 0.998313 I_M^2 - 18.6634 I_M + 88.6668 \end{array}} \text{ m/s} \end{aligned} \tag{5.17}$$

where I must be inserted in amperes. Here, I_M is the current going through the master in ampere, and I_C the current through the compensation coil in ampere.

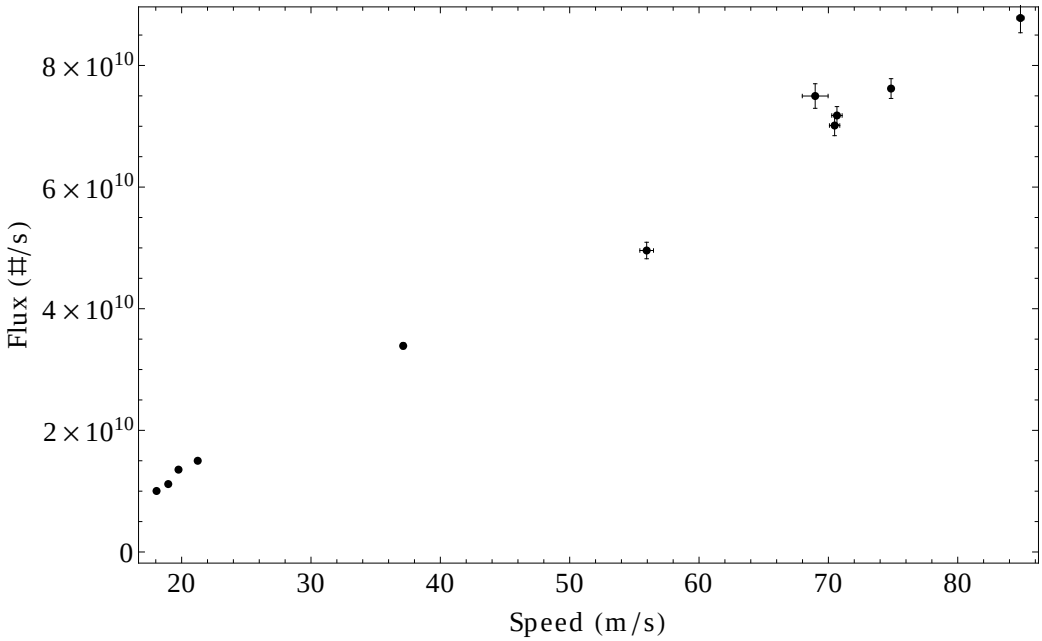

Figure 5.12: Flux versus speed. The line seems quite linear but is not when looking closer at it. The linear component comes from the fact that the flux scales with the speed. The nonlinear component is shown in Figure 5.13. The uncertainties are calculated using the Lorentzians with appropriate covariances.

Absorption versus speed Also one could be interested what the effect of this changing speed has on the flux. This is shown in Figure 5.12. It shows the flux versus the speed. It seems mostly linear, which is not that surprising since the flux scales with the speed in the original formula as explained in Section 5.4.2. But looking closer at the linear line is only visual, as it would imply that the absorption is constant, which it is certainly not, as can be seen in Figure 5.13. This figure shows the maximal percentage of absorption versus the speed. Since $\ln\left(\frac{1}{1-A}\right) \approx A$ at these absorption percentages this scales almost directly with the flux divided by the speed, giving the number of particles per length unit, this is given at the right-hand axes. The behavior seems to give a lower number of particles at a lower speed, making the effect of lower flux at lower speed even more extreme. The behavior turns out to be described quite well on this range by the following working formula:

$$A_{\max} = 0.167 \ln\left(\frac{v - 17\ \text{m/s}}{0.011\ \text{m/s}}\right) \pm \frac{\sqrt{\begin{array}{c}0.0273127v^2 + 0.000441967v^2 \ln^2(92.81v - 1578.52) - 0.00689588v^2 \ln(92.81v - 1578.52) \\ -0.960201v - 0.015034v \ln^2(92.81v - 1578.52) + 0.12785 \ln^2(92.81v - 1578.52) \\ +0.238384v \ln(92.81v - 1578.52) - 2.05965 \ln(92.81v - 1578.52) + 8.44071\end{array}}}{v - 17.0081}\% \tag{5.18}$$

but there seems to be no physical reason for this.

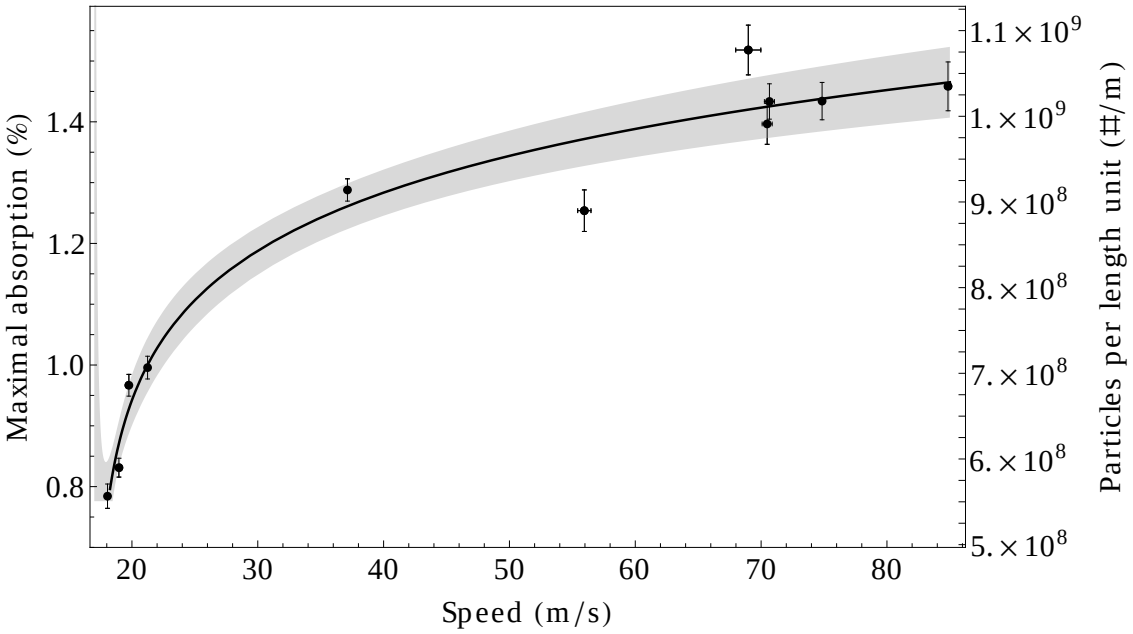

Figure 5.13: Absorption versus speed. Since at these absorption percentages $\ln\left(\frac{1}{1-A}\right) \approx A$ this scales with the flux/v = *particles per length unit* too. This is shown on the right-hand axis. Uncertainties in the data come from the Lorentzian fits. The working function is also shown, the gray area is the two times uncertainty in where the line should be.

Discussion

Although the behavior of the speed versus the current seems fairly linear, fitting a linear line in Figure 5.9 corresponds with an estimated variance of 80. This may indicated that the uncertainties in speed were underestimated, which seems reasonable, since they only come from the original fit of Lorentzians, while accounting for the correct covariances, and do not include any other variations. Still it makes the claim that it is linear only valid to a certain approximation, making that we can only trust the model in a certain range of master currents and of compensation coil currents. It does however seem valid (to a certain approximation) to use the model in the entire plane between 6 and 10 A for both the master and the compensation. The model for the absorption is a true working formula and only valid in the measured range. Further one must realize that we have to do with working formulas and not with theoretical models in this Section.

Conclusion

We can conclude that we obtained a model of getting the speed of the particles from the values of the currents. Further we see that lowering the speed costs flux, not only because the flux scales with the speed, but also because the number of particles per meter drops. The working function of this seems to suggest a negative flux for speeds lower than 17 m/s, something that is completely non-physical, so it would be interesting to see what happens at lower speeds. Unfortunately, as explained in 'Speed versus current' it is impossible to measure speeds (and distinguish them from the characteristics of the transition) below 18 m/s.

5.6 Conclusion

The most important conclusions from the measurement of the fast flux (with varying oven temperature) is that the loss in the Second Chamber of the oven is by far the most determining factor in terms of particle loss. If the density in the Second Chamber is lowered, then the particle flux from the oven can become much larger. Another way to increase the flux is to increase the Zeeman

power (this follows from the slow flux measurements). Also, as illustrated in Figure 5.12, because the flux scales with the speed, lowering the speed also lowers the flux, since it can be seen in Figure 5.13 that lowering the speed does not increase the density.

Acknowledgments

A master thesis can be written, but can certainly not be done without the help of others. Therefore, in this Chapter I would like to thank everyone who helped and supported me during the year (or better: 14 months) that I have been here. First of all, I would like to thank the head of the research group, Peter van der Straten. He has always been willing to answer all the questions I might have, including the dumb ones. From him, I have also learned that it is always good to listen to someone with much more experience in the research field than myself - when trying to find analytical expressions for the magnetic field of a curved piece of wire, he suggested that I should use the magnetic vector potential, which is a thing very briefly mentioned during the Bachelor's course on electrodynamics. I never did anything more than some odd exercise with it, and above all it did not have any advantages over just using the expressions for the magnetic field itself (because there are both vectors), or so I thought. After a long try to not use the magnetic vector potential, I decided to give it a try, and it worked. Finally. Second, I would like to thank Pieter Bons. He also was always willing to answer my questions, usually by asking me another question to (try to...) make me figure it out myself. I know I sometimes ask too much questions and in such cases, it is good to *not* straight away answer them, and Pieter is very good at that. Also, he was always very helpful during the sessions in the lab, trying to get me do things myself even when I did it the clumsy way. Third, I would like to thank Alexander Groot, the other PhD in the group. Although he was not my direct supervisor, he was always ready to answer questions if Pieter and/or Peter was not there (or not available).
Furthermore, I would like to thank my fellow students in the group, first of all Johan van der Tol, not only for the collaboration on the chapter about Particle flux, but also for always being ready to help with all sorts of things (like *Mathematica*-coding) and good discussions. Furthermore, for their useful input and interesting discussions I would like to thank Peter Elroy, Christian te Riet, Damaz de Jong, Jasper Smits and Stefan Korenberg.
Also, I would like to thank the technical staff, consisting of Paul Jurrius, Cees de Kok, Dante Killian and especially Frits Ditewig, who was always willing to answer questions and provide useful documentation which turned out to be crucial to calculate the correct magnetic fields for the MT. Last but not least, I would like to thank you, the reader, for reading my thesis.

Appendices

Appendix A

Table of constants

In Table A.1, some relevant constants, used in this thesis, are given.

Constant	Description	Value
μ_0	Vacuum permeability	$4\pi \times 10^{-7}$ N A^{-2}
a_B	Bohr radius	$5.2917720859(36) \cdot 10^{-11}$ m
k_B	Boltzmann's constant	$1.3806504(25) \cdot 10^{-23}$ J K^{-1}
$\hbar$	(Reduced) Planck's constant	$1.054571628(53) \cdot 10^{-34}$ J s
m	Mass of a sodium atom	$0.381754035(19) \times 10^{-25}$ kg
μ_B	Bohr Magneton	$9.27400915(23) \times 10^{-24}$ J T^{-1}
m_F	Hyperfine sublevel of $3^2S_{1/2}$ transition	-1
g_J	Fine structure Landé g-factor of $3^2S_{1/2}$ transition	2.00229600(70)
g_I	Nuclear g-factor	-0.00080461080(80)
I	Nuclear spin of sodium	$\frac{3}{2}$

Table A.1: An overview of relevant constants. [3]

Appendix B

Graphs of the center of mass fits

In this Appendix, the graphs of all measurements series involving the center of mass method are shown. The case $P_{\text{cool}} = 283\text{V}$, spin-dependent force $1.77 \cdot 10^{-25}$ N with a Gaussian distributed spin drag rate is already shown in Figures 3.11 and 3.12. The meaning of the several curves on the graphs is already explained in Section 3.4.2. The captions in this Appendix only contain the FORT powers and spin-dependent, and whether the spin drag rate is assumed to be constant or Gaussian.

B.1 Gaussian spin drag rate

In this Section, the spin drag rate is calculated using the Gaussian model. The points represented on the graphs are thus the centers of mass of the *condensates*.

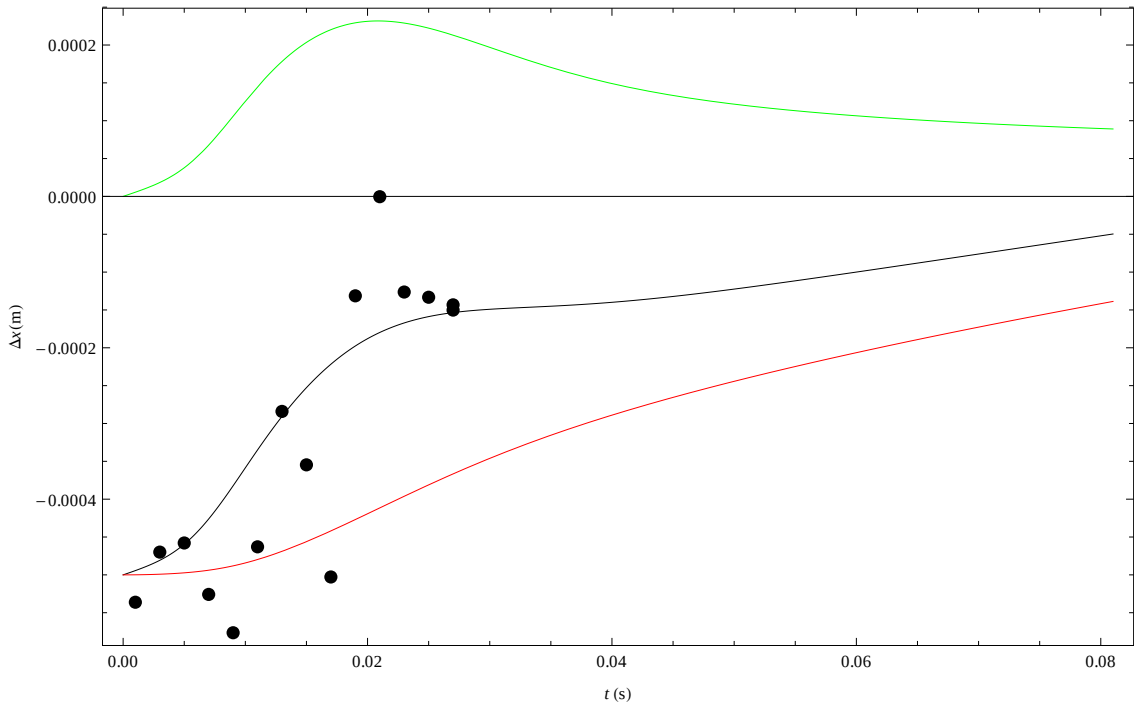

Figure B.1: FORT power: 187 mW. $F_{\text{MOT}} = 3.55 \cdot 10^{-26}$ N.

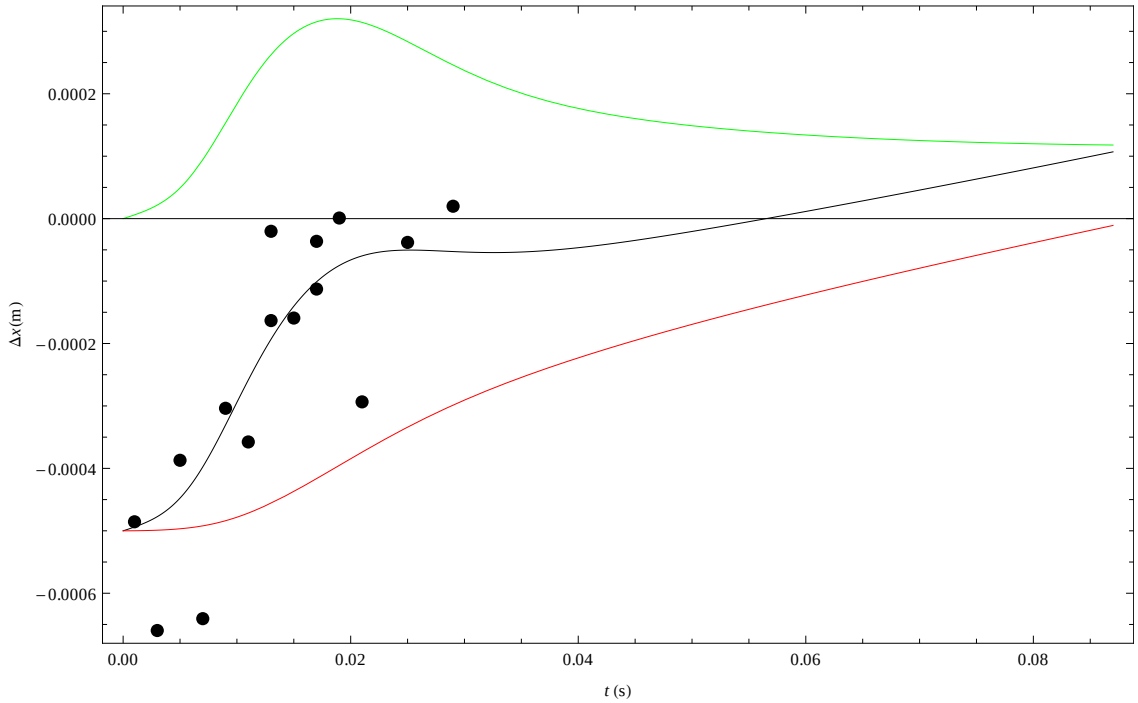

Figure B.2: FORT power: 187 mW. $F_{\mathrm{MOT}} = 5.92 \cdot 10^{-26}$ N.

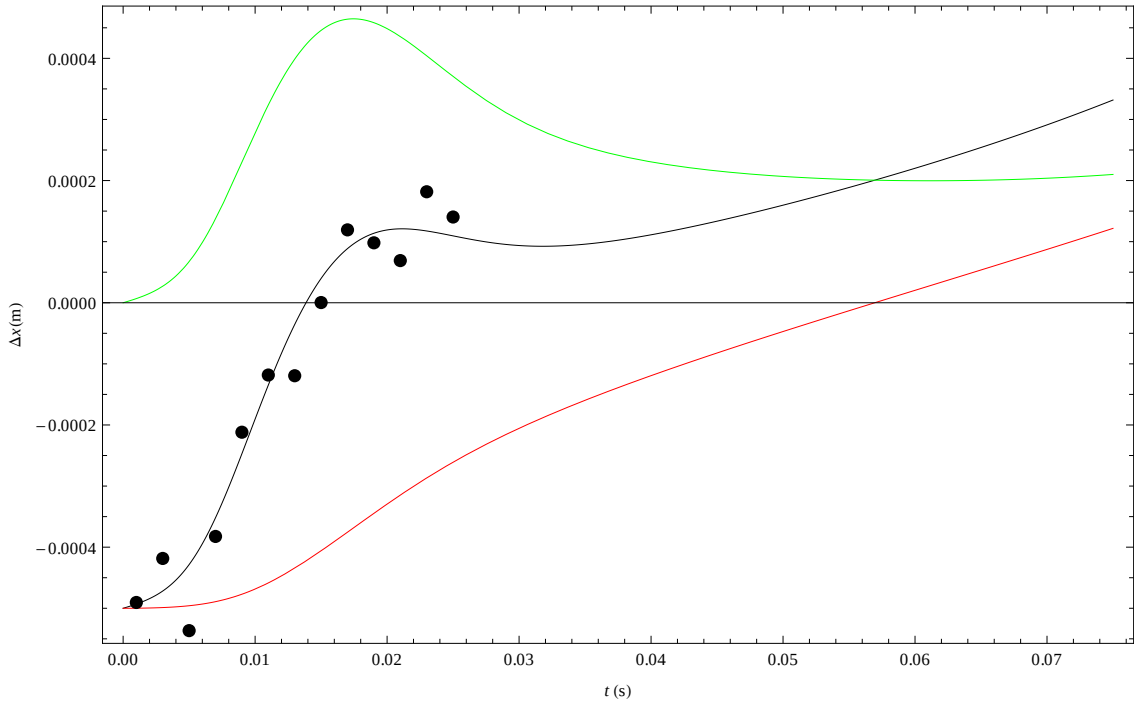

Figure B.3: FORT power: 187 mW. $F_{\mathrm{MOT}} = 9.48 \cdot 10^{-26}$ N.

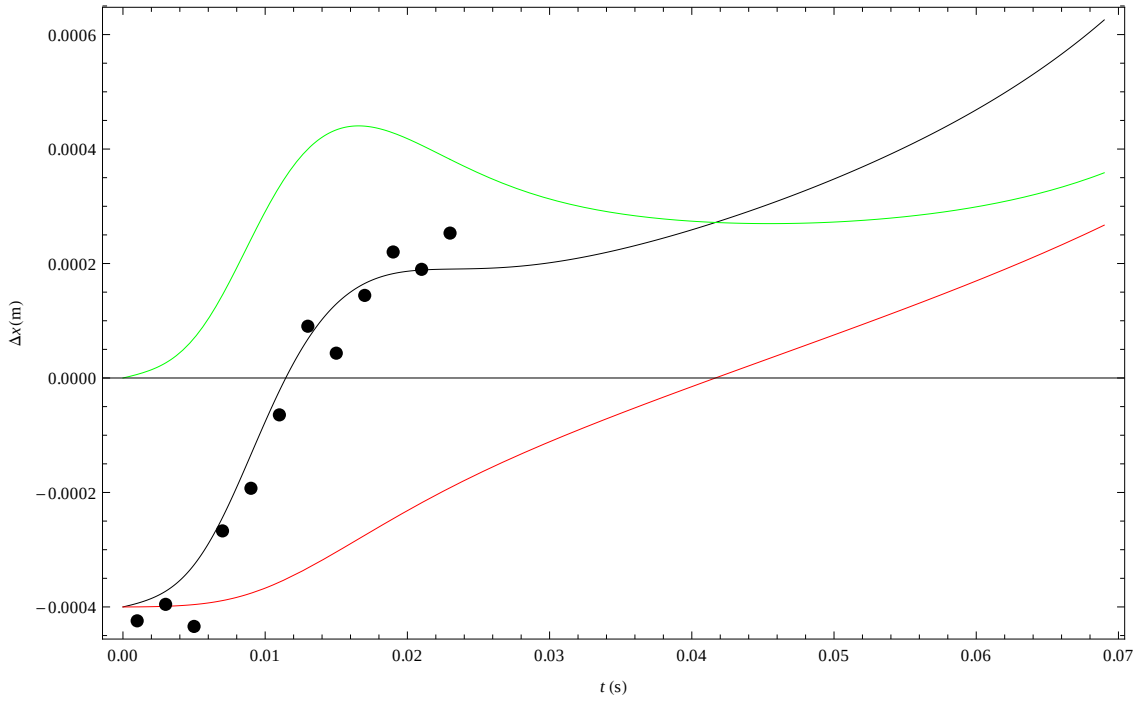

Figure B.4: FORT power: 187 mW. $F_{\mathrm{MOT}} = 1.18 \cdot 10^{-25}$ N.

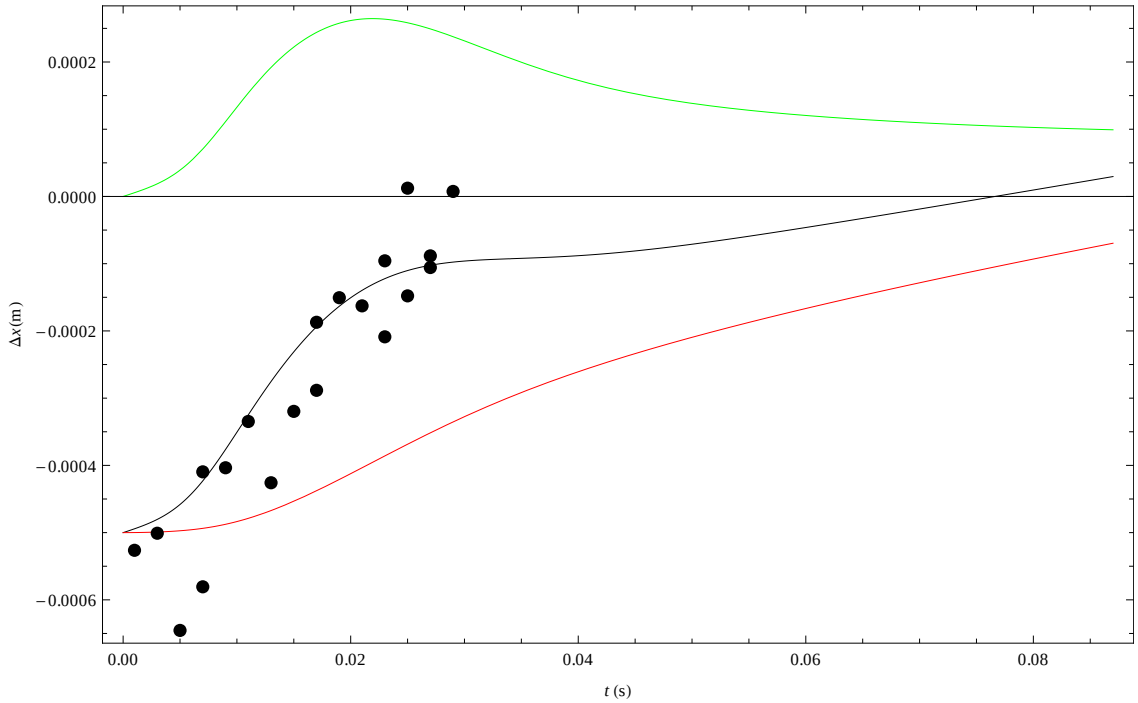

Figure B.5: FORT power: 283 mW. $F_{\mathrm{MOT}} = 3.55 \cdot 10^{-26}$ N.

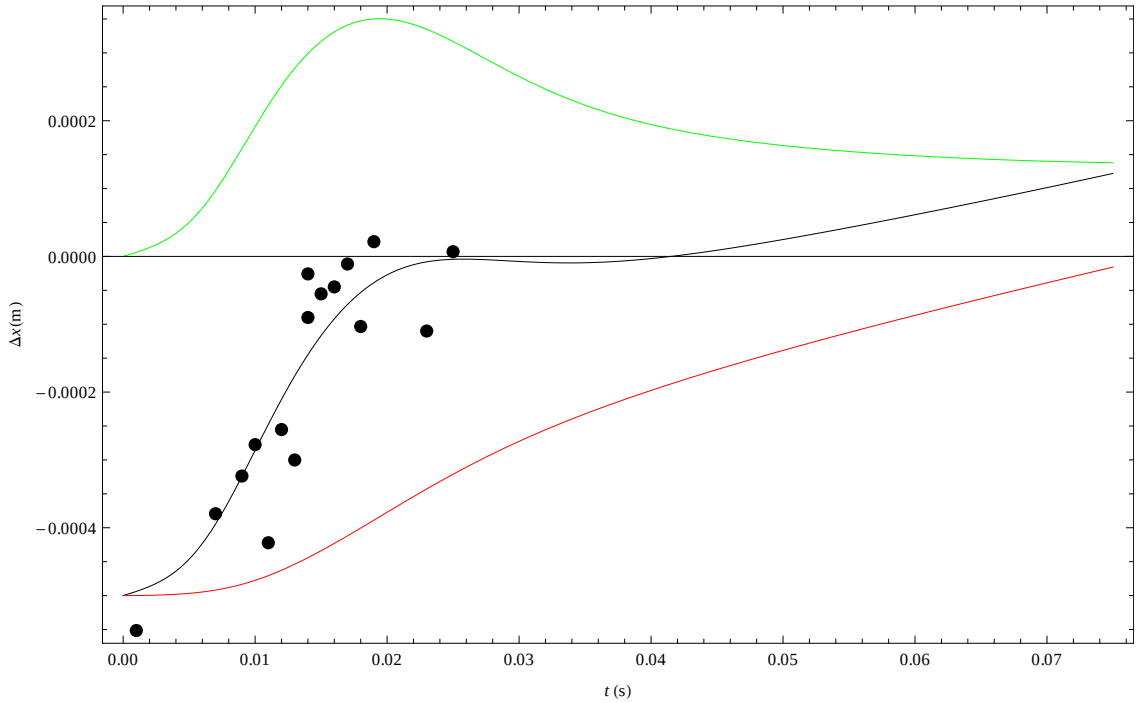

Figure B.6: FORT power: 283 mW. $F_{\mathrm{MOT}} = 5.92 \cdot 10^{-26}$ N.

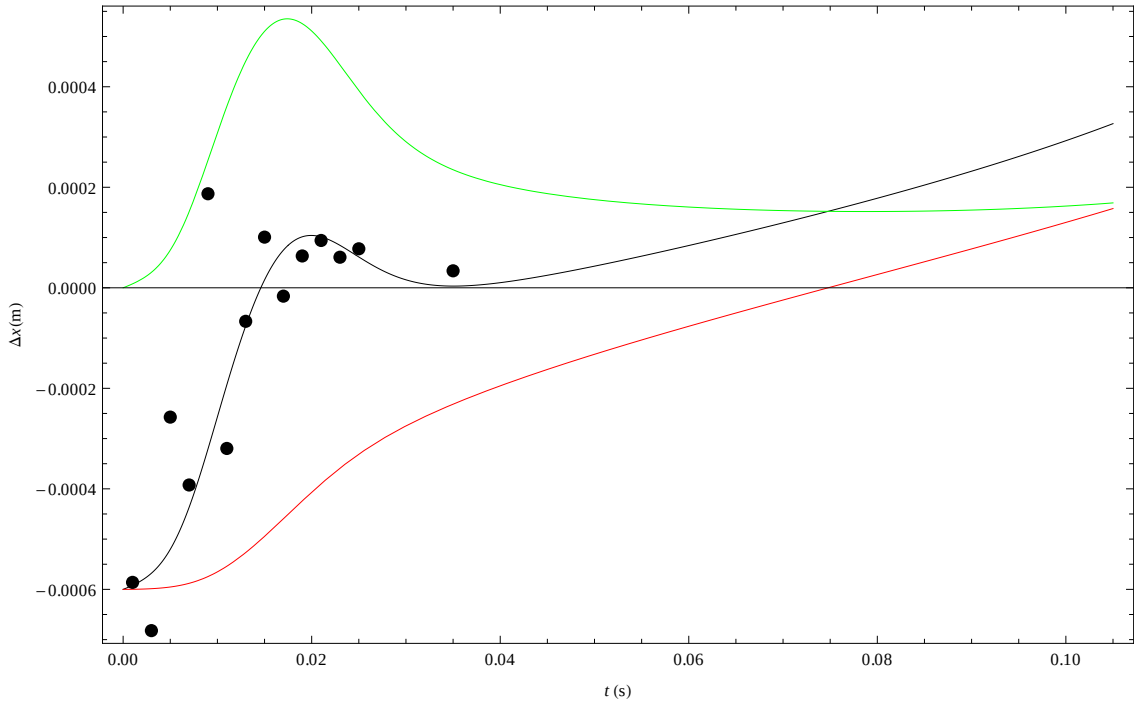

Figure B.7: FORT power: 283 mW. $F_{\mathrm{MOT}} = 9.48 \cdot 10^{-26}$ N.

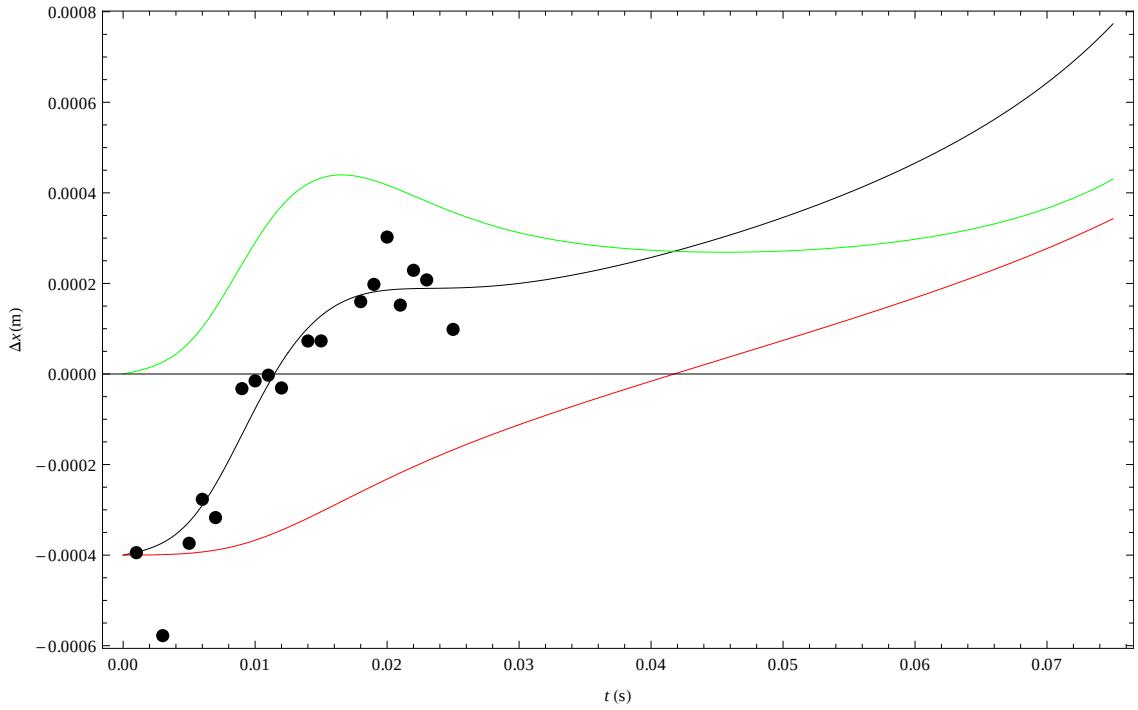

Figure B.8: FORT power: 283 mW. $F_{\mathrm{MOT}} = 1.18 \cdot 10^{-25}$ N.

B.2 Constant spin drag rate

In this Section, the spin drag rate is calculated using the assumption that it is constant. The points represented on the graphs are thus the centers of mass of the *thermal clouds*, which give different values for $\Delta x(t)$.

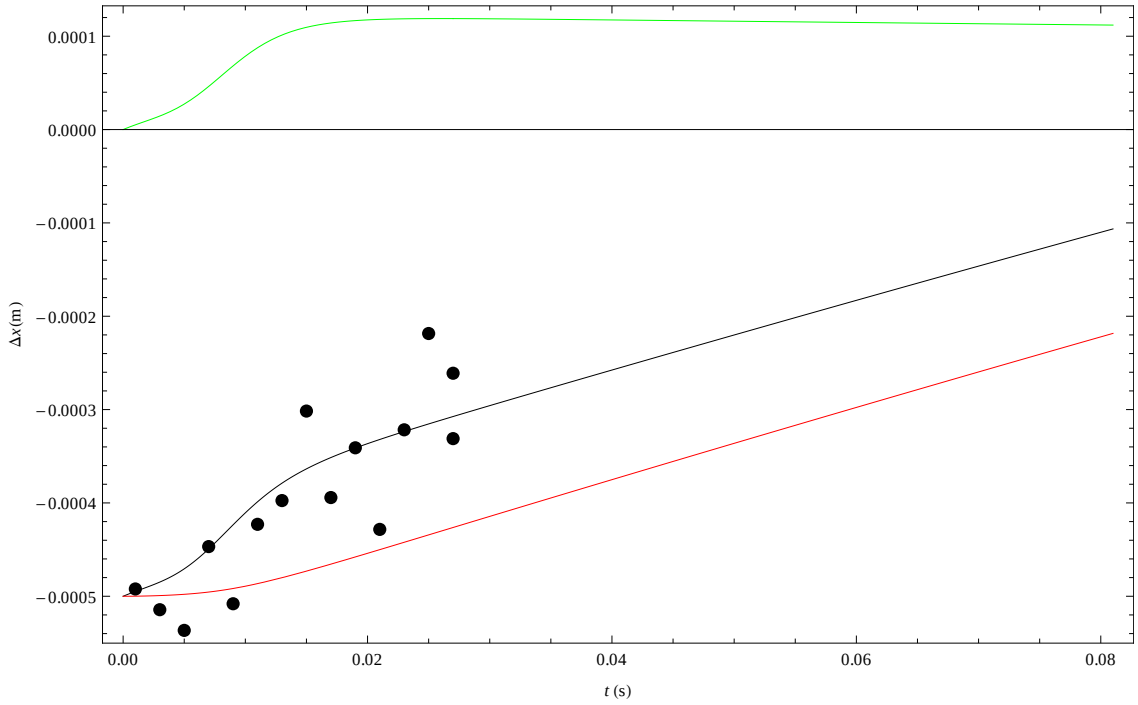

Figure B.9: FORT power: 187 mW. $F_{\mathrm{MOT}} = 3.55 \cdot 10^{-26}$ N.

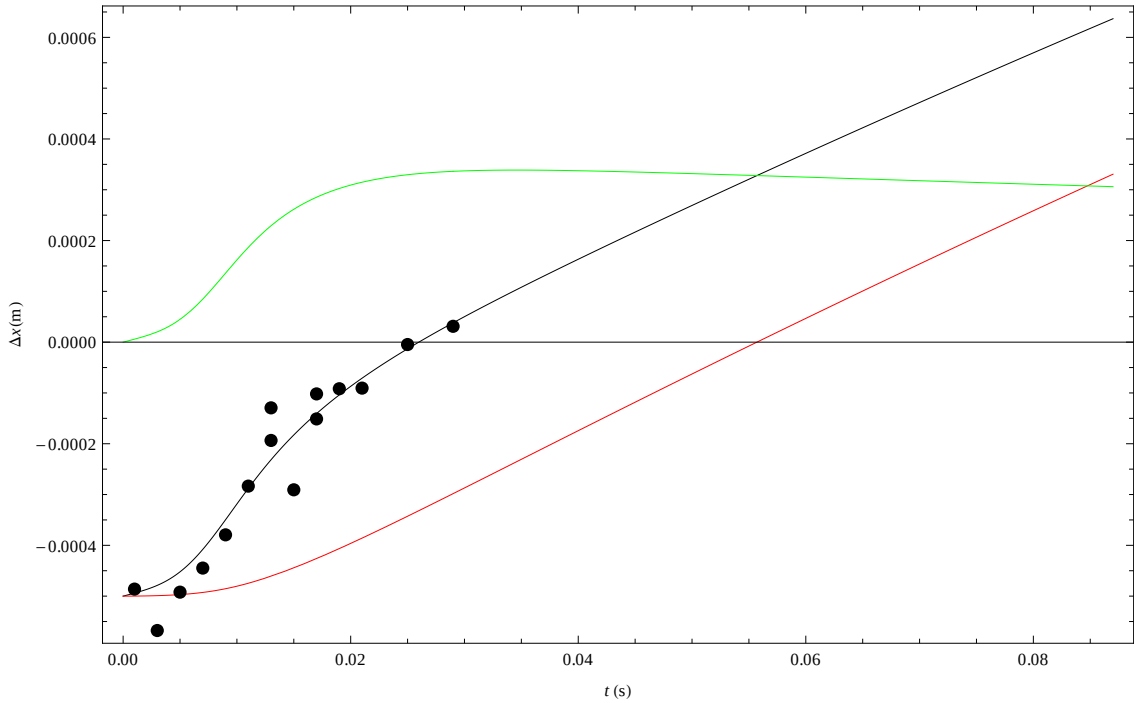

Figure B.10: FORT power: 187 mW. $F_{\mathrm{MOT}} = 5.92 \cdot 10^{-26}$ N.

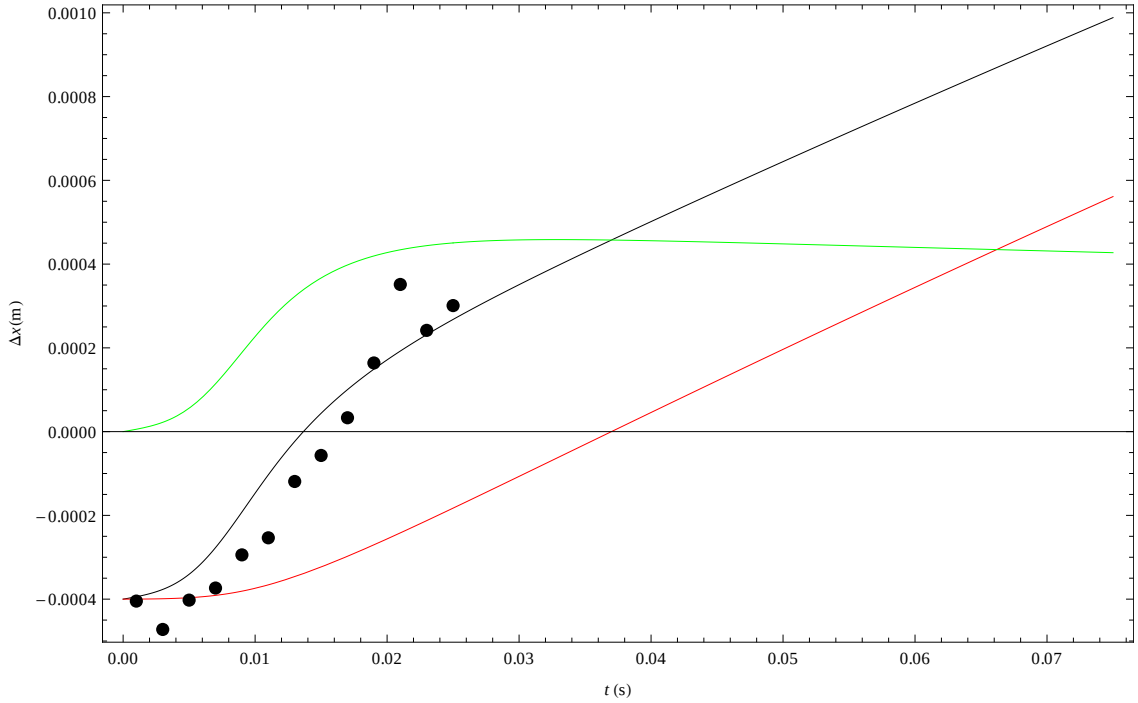

Figure B.11: FORT power: 187 mW. $F_{\mathrm{MOT}} = 9.48 \cdot 10^{-26}$ N.

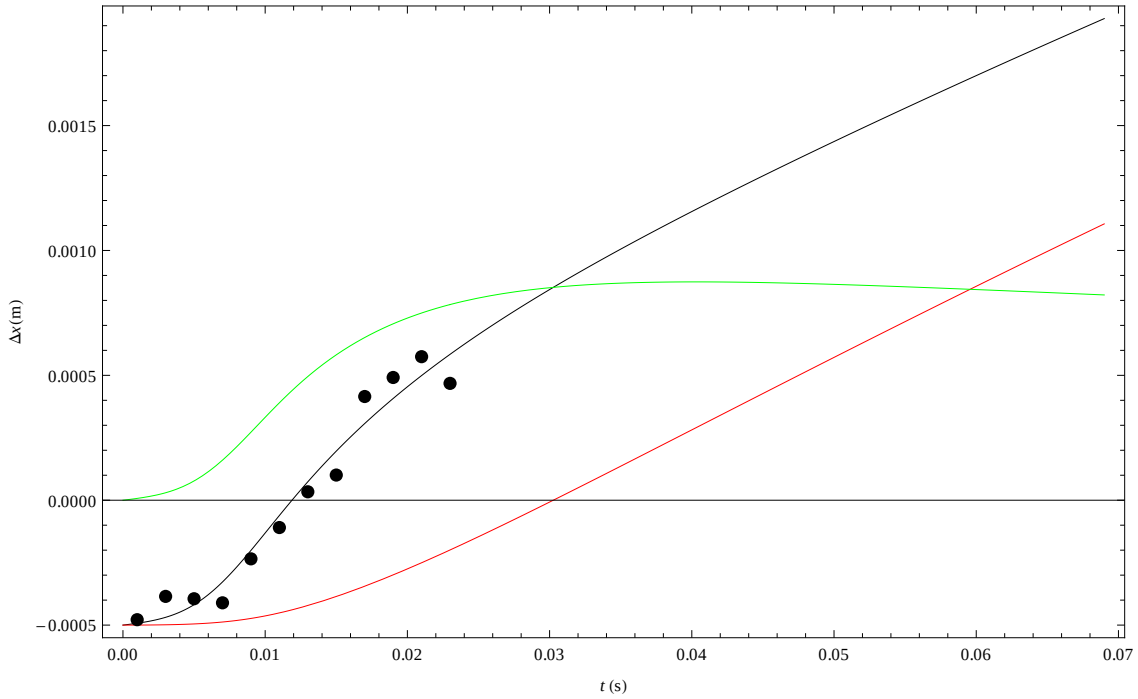

Figure B.12: FORT power: 187 mW. $F_{\mathrm{MOT}} = 1.18 \cdot 10^{-25}$ N.

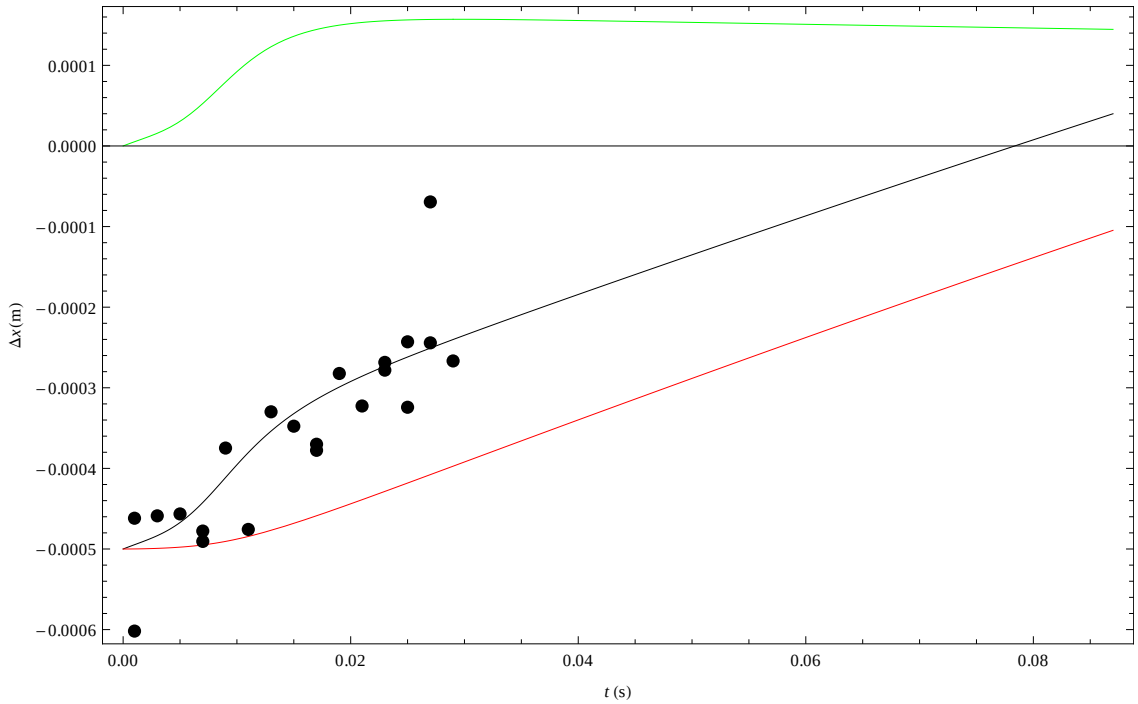

Figure B.13: FORT power: 283 mW. $F_{\mathrm{MOT}} = 3.55 \cdot 10^{-26}$ N.

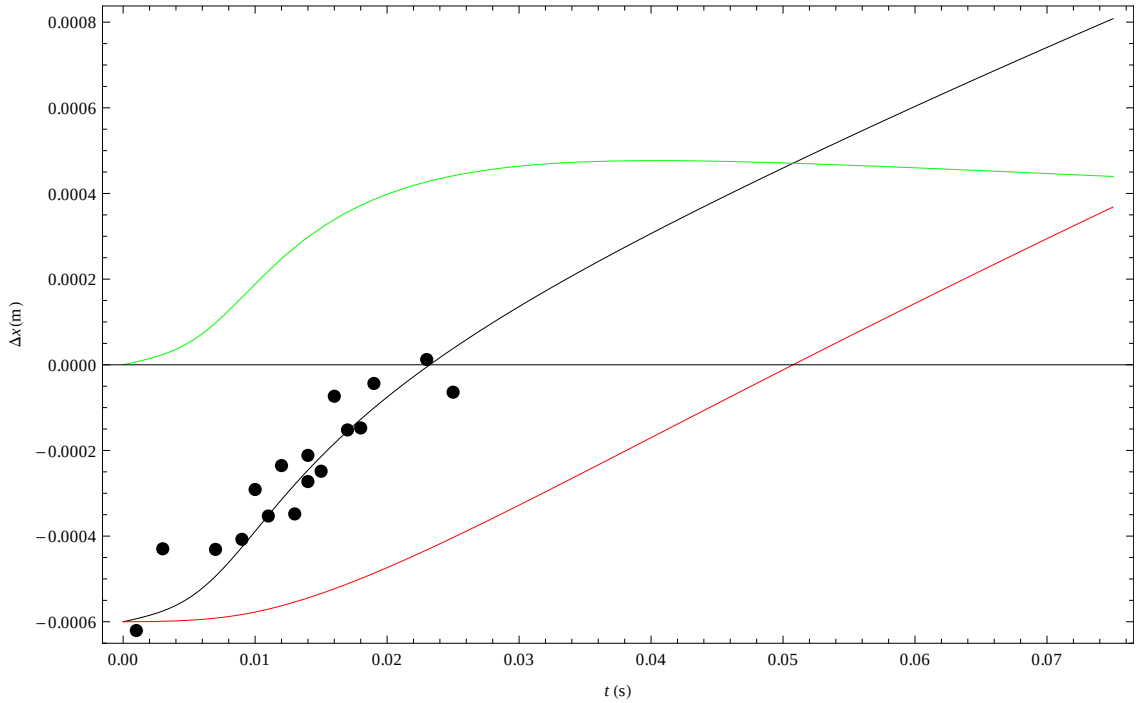

Figure B.14: FORT power: 283 mW. $F_{\mathrm{MOT}} = 5.92 \cdot 10^{-26}$ N.

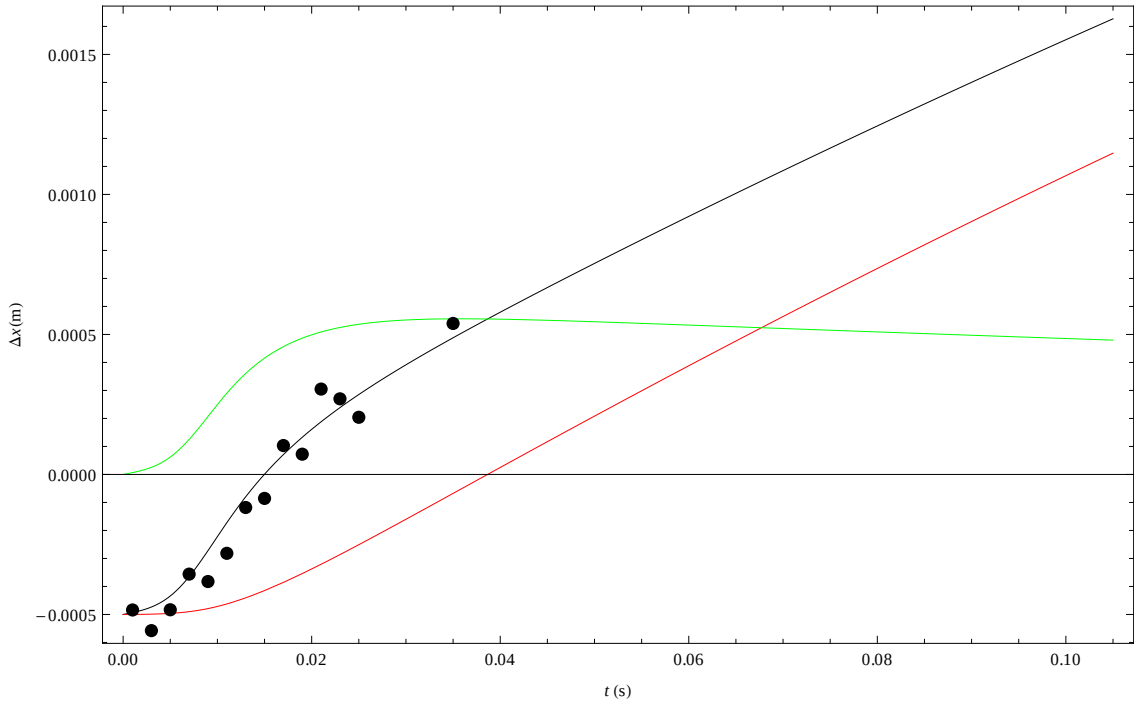

Figure B.15: FORT power: 283 mW. $F_{\mathrm{MOT}} = 9.48 \cdot 10^{-26}$ N.

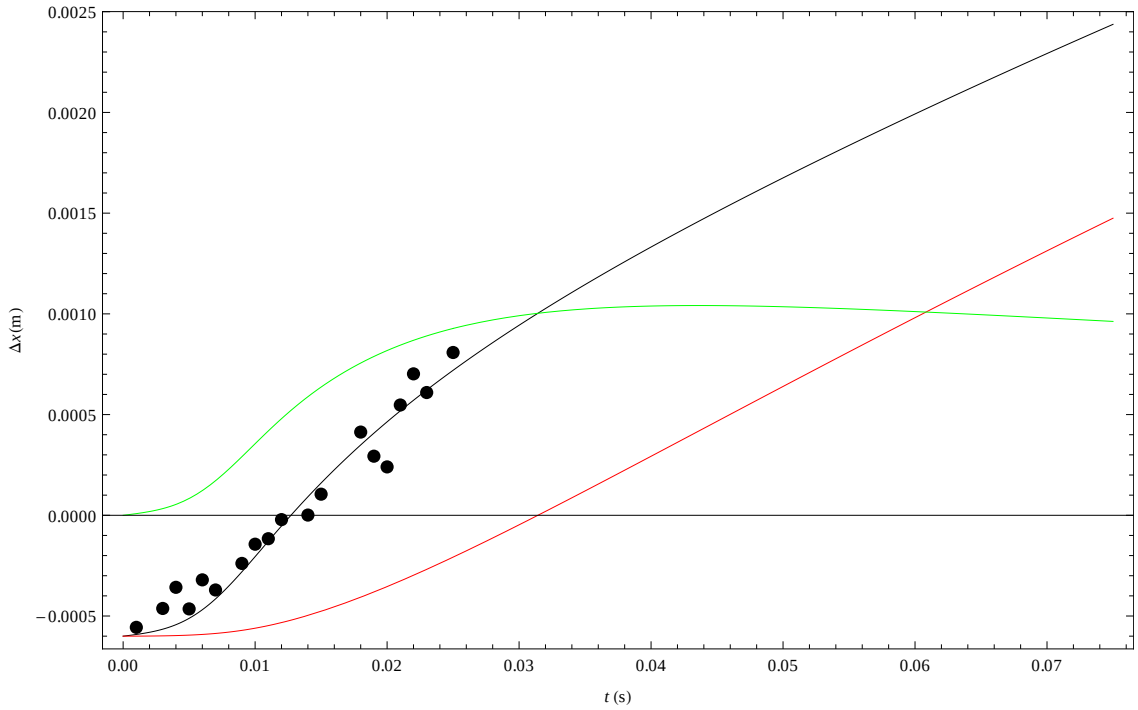

Figure B.16: FORT power: 283 mW. $F_{\mathrm{MOT}} = 1.18 \cdot 10^{-25}$ N.

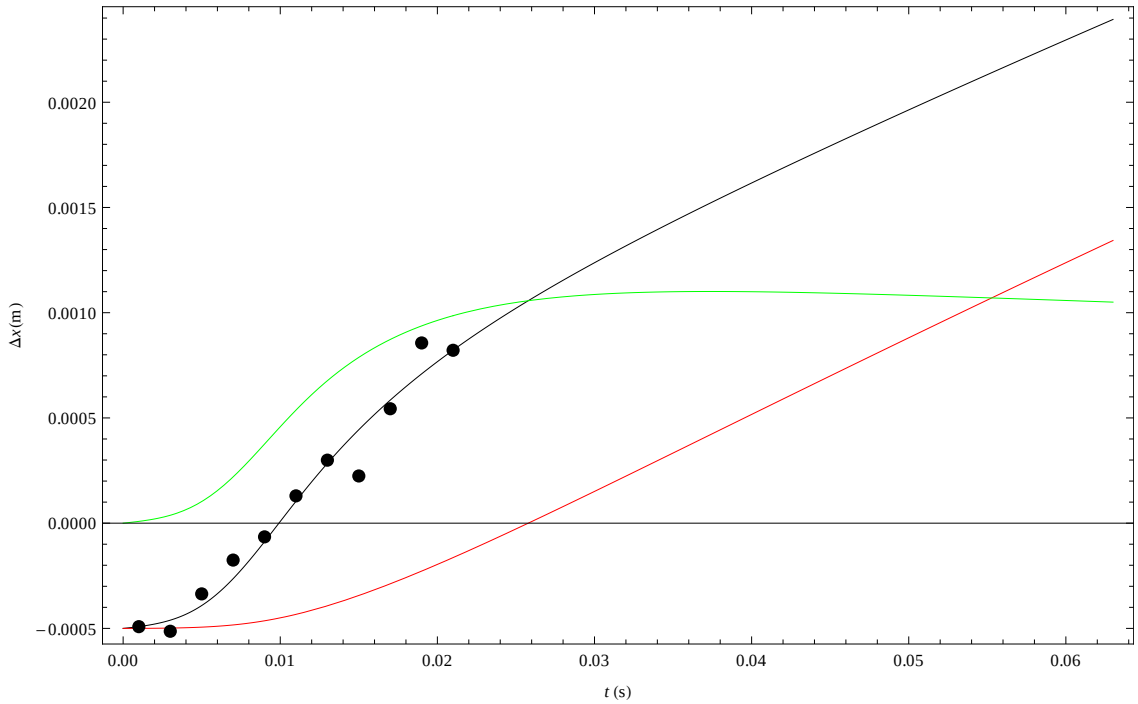

Figure B.17: FORT power: 283 mW. $F_{\mathrm{MOT}} = 1.77 \cdot 10^{-25}$ N.

Appendix C

Elliptic Integrals

There are three kinds of elliptic integrals: elliptic integrals of the first, second and third kind. Each of them has a complete and an incomplete variant. In the calculations presented in Sections (4.3.1) and (4.3.2), elliptic integrals of the first and second kind are used. In this Appendix, some more information and properties (relevant for this master thesis) about these integrals is provided.

C.1 Elliptic integral of the first kind

The **complete elliptic integral of the first kind** is given by:

$$K(m) = \int_0^{\frac{\pi}{2}} \frac{1}{1 - m\sin^2(\theta)} d\theta. \tag{C.1}$$

In this master thesis, m is always equal to k^2, which is given by Eq. (4.7). For $-\frac{\pi}{2} < \phi < \frac{\pi}{2}$, the **incomplete elliptic integral of the first kind** is given by:

$$F(\phi|m) = \int_0^{\phi} \frac{1}{1 - m\sin^2(\theta)} d\theta. \tag{C.2}$$

The relation between the complete and incomplete elliptic integral of the first kind is given by $F(\frac{\pi}{2}|m) = K(m)$. The notations used in this master thesis are from [21]. There are also other possible notations possible,see for instance [22]. In order to avoid confusion, these notations are not used. The derivative of the elliptic integral of the first kind is given by:

$$\frac{dK(m)}{dm} = \frac{E(m)}{2m(1-m)} - \frac{K(m)}{2m}. \tag{C.3}$$

C.2 Elliptic integral of the second kind

The **complete elliptic integral of the second kind** is given by:

$$E(m) = \int_0^{\frac{\pi}{2}} 1 - m\sin^2(\theta) d\theta. \tag{C.4}$$

Here, m is defined as above. For $-\frac{\pi}{2} < \phi < \frac{\pi}{2}$, the **incomplete elliptic integral of the second kind** is given by:

$$E(\phi|m) = \int_0^{\phi} 1 - m\sin^2(\theta) d\theta. \tag{C.5}$$

The relation between the complete and incomplete elliptic integral of the first kind is given by $E(\frac{\pi}{2}|m) = E(m)$. The notations used in this master thesis are from [21]. There are also other possible notations possible, see for instance [22]. In order to avoid confusion, these notations are not used. The derivative of the elliptic integral of the second kind is given by:

$$\frac{dE(m)}{dm} = \frac{E(m) - K(m)}{2m}. \tag{C.6}$$

Appendix D

Magnetic field components of the circular current arcs

In Section (4.3.2), the components of the magnetic field of a circular current arc are calculated. Because the expressions of the components of the magnetic field are quite lengthy, they are given in this Appendix. In the expressions, k^2 is given by Eq. (4.7). Furthermore, in order to make the notation as compact as possible, the following functions are defined:

$$\bar{E}(\theta_1', \theta_2'|k^2) = E(\theta_2'|k^2) - E(\theta_1'|k^2), \tag{D.1}$$

$$\bar{F}(\theta_1', \theta_2'|k^2) = F(\theta_2'|k^2) - F(\theta_1'|k^2), \tag{D.2}$$

$$f(\theta_i) = \sqrt{\frac{R^2 + \rho^2 - 2R\rho\cos(\theta_i - \phi) + (z - z_\mathrm{d})^2}{(R^2 + \rho^2) + (z - z_\mathrm{d})^2}}, \tag{D.3}$$

$$g(\theta_i) = \frac{2\sin(\theta_i - \phi)}{(k^2 - 1)\sqrt{1 - k^2\cos^2\left(\frac{-\theta_i + \phi + 2\pi}{2}\right)}}. \tag{D.4}$$

With these functions, the components of the magnetic field are:

$$\begin{aligned} B_\rho(\rho, \phi, z) = {} & \frac{\mu_0 I R(z - z_\mathrm{d})}{4\pi}\sqrt{\frac{1}{(R+\rho)^2 + (z - z_\mathrm{d})^2}}\left[\frac{2}{R\rho}\big(\bar{E}(\theta_1', \theta_2'|k^2)\right. \\ & - \bar{F}(\theta_1', \theta_2'|k^2)\big) + \frac{1}{R\rho}\left(-\bar{E}(\theta_1', \theta_2'|k^2) + \bar{F}(\theta_1', \theta_2'|k^2)\right) + \\ & \frac{2\left(\left(\frac{2}{k^2} - 1\right)\bar{F}(\theta_1', \theta_2'|k^2) - \frac{2}{k^2}\bar{E}(\theta_1', \theta_2'|k^2)\right)}{(R+\rho)^2 + (z - z_\mathrm{d})^2} - \frac{2R\rho}{\left((R+\rho)^2 + (z - z_\mathrm{d})^2\right)^2}\left(\frac{2}{k^2} - 1\right) \\ & \left.\left(\frac{4}{k^2(k^2-1)}\bar{E}(\theta_1', \theta_2'|k^2) + \frac{4}{k^2}\bar{F}(\theta_1', \theta_2'|k^2) - f(\theta_1) + f(\theta_2)\right)\right], \end{aligned} \tag{D.5}$$

$$B_\phi(\rho, \phi, z) = -\frac{\mu_0 I(z - z_\mathrm{d})}{4\pi\rho}\sqrt{\frac{1}{(R+\rho)^2 + (z - z_\mathrm{d})^2}}\left(\frac{f(\theta_1) - f(\theta_2)}{f(\theta_1)f(\theta_2)}\right), \tag{D.6}$$

$$B_z(\rho,\phi,z) = \frac{\mu_0 I R}{4\pi\rho}\sqrt{\frac{1}{(R+\rho)^2+(z-z_\mathrm{d})^2}}\Bigg[\frac{R^2+\rho^2+(z-z_\mathrm{d})^2}{R\rho}\bar{F}(\theta_1',\theta_2'|k^2) - \frac{4}{k^2}\bar{E}(\theta_1',\theta_2'|k^2)$$

$$-\frac{k^2(R+\rho)}{2R}\left[(\frac{2}{k^2}-1)\bar{F}(\theta_1',\theta_2'|k^2) - \frac{2}{k^2}\bar{E}(\theta_1',\theta_2'|k^2)\right] + \frac{\sin(\theta_1-\phi)}{f(\theta_1)} - \frac{\sin(\theta_2-\phi)}{f(\theta_2)} + \frac{\rho}{2R}\cdot$$

$$\left[\frac{2R^2(R^2-\rho^2+(z-z_\mathrm{d})^2)}{((R+\rho)^2+(z-z_\mathrm{d})^2)^2}(\frac{2}{k^2}-1)\left(g(\theta_1)-g(\theta_2) - \frac{4}{k^2(k^2-1)}\bar{E}(\theta_1',\theta_2'|k^2) - \frac{4}{k^2}\bar{F}(\theta_1',\theta_2'|k^2)\right)\right.$$

$$-\frac{4(R+\rho)}{\rho}\bar{E}(\theta_1',\theta_2'|k^2) + \frac{2((R+\rho)^2+(z-z_\mathrm{d})^2)}{\rho^2}\bar{E}(\theta_1',\theta_2'|k^2) - \frac{2(R^2-\rho^2+(z-z_\mathrm{d})^2)}{\rho^2}\bar{F}(\theta_1',\theta_2'|k^2)$$

$$\left.+\frac{(R^2-\rho^2+(z-z_\mathrm{d})^2)}{\rho^2}\left(\bar{F}(\theta_1',\theta_2'|k^2)-\bar{E}(\theta_1',\theta_2'|k^2)\right)\right]\Bigg]. \tag{D.7}$$

If $\theta_1 = 0$ and $\theta_2 = 2\pi$ are inserted in Eqs. (D.5), (D.6) and (D.7), then Eqs. (4.17), (4.18) and (4.19) are obtained again.

Bibliography

[1] C. Pethick and H. Smith. *Bose-Einstein Condensation in Dilute Gases*. Cambridge University Press, 2002.

[2] R. Grimm, M. Weidemüller, and Y. B. Ovchinnikov. Optical Dipole Traps for Neutral Atoms. *Advances in Atomic Molecular and Optical Physics*, 42:95–170, 2000.

[3] Daniel A. Steck. Sodium d line data. Online available at http://steck.us/alkalidata (revision 2.0.1, 2 May 2008).

[4] J. van der Tol. Increasing the chemical potential by using a local optical ultra-tight dipole trap. Master's thesis, Universiteit Utrecht, 2013.

[5] Silvio B. Koller. *Experiments on Hydrodynamic Transport in Ultra-Cold Bose Gasses*. PhD thesis, Universiteit Utrecht, 2012.

[6] Shu-Wei Song, Lin Wen, Chao-Fei Liu, S.-C. Gou, and Wu-Ming Liu. Ground states, solitons and spin textures in spin-1 bose-einstein condensates. *Frontiers of Physics*, 8(3):302–318, 2013.

[7] L.P. Pitaevskii and S. Stringari. *Bose-Einstein Condensation*. International Series of Monographs on Physics. Clarendon Press, 2003.

[8] H. J. van Driel, R. A. Duine, and H. T. C. Stoof. Spin-drag hall effect in a rotating bose mixture. *Physical Review Letters*, 105(15), 2010. Cited By (since 1996):6.

[9] R Kittinaradorn, R A Duine, and H T C Stoof. Critical spin transport in bose gases. *New Journal of Physics*, 14(5):055007, 2012.

[10] Roland Stas. Laser cooling and trapping of metastable neon atoms. Master's thesis, Eindhoven University of Technology, Jul 1999.

[11] E.D. van Ooijen. *Realization and Illumination of Bose-condensed Sodium Atoms*. PhD thesis, Universiteit Utrecht, May 2005.

[12] W. R. Smythe. *Static and dynamic electricity*. McGraw-Hill, New York, 1975.

[13] D.J. Griffiths. *Introduction to electrodynamics*. Prentice Hall, 1999.

[14] T. Bergeman, Gidon Erez, and Harold J. Metcalf. Magnetostatic trapping fields for neutral atoms. *Phys. Rev. A*, 35:1535–1546, Feb 1987.

[15] R. Meppelink. *Hydrodynamic Excitations in a Bose-Einstein Condensate*. PhD thesis, Universiteit Utrecht, 2009.

[16] H.J. Metcalf and P. Van Der Straten. *Laser Cooling and Trapping*. Graduate Texts in Contemporary Physics. Springer-Verlag GmbH, 1999.

[17] W.L. Kruithof. *Laser Trapping of Sodium Isotopes for a High-precision [beta]-decay Experiment*. University Library Groningen] [Host], 2012.

[18] L. Holt. Experimental setups for bose-einstein condensates. Master's thesis, Universiteit Utrecht, 2011.

[19] K.M.R. van der Stam. *Superradiant scattering of laser light from a Bose-Einstein condensate.* PhD thesis, Universiteit Utrecht, 2006.

[20] P.K. Rol. *Inleiding tot de vacuümtechniek.* Argus, 1967.

[21] Wolfram online: Elliptic Integrals and Elliptic Functions. Last visited at May 3, 2013.

[22] Wikipedia: Elliptic integral. Last visited at May 3, 2013.